Politecnico di Torino

Master's degree in Biomedical Engineering

Dose Assessment in Pediatric Cone Beam CT: an Experimental and Computational Study

Supervisors:

Prof. Gianni Coppa
Dr. Salvatore Di Maria (Istituto Superiore Tecnico Lisboa)
Dr. Ana Sá (Istituto Superiore Tecnico Lisboa)

Candidate:

Stefano Puggioni

Academic Year 2022/2023

Abstract

Cone beam computed tomography (CBCT) is widely used for pre-treatment verification and patient setting in image-guided radiation therapy (IGRT). IGRT using CBCT allows visualization of soft tissue targets and critical structures prior to treatment in order to visualize and verify the patient position. Furthermore, since CBCT imaging is used daily and multiple times per patient, and this could result in a potentially high cumulative doses to healthy tissues surrounding the exposed target organs.

Balancing the concomitant imaging dose and patient positioning accuracy is critical in IGRT especially for children, whose higher biological susceptibility and longer expected life make them more vulnerable to develop secondary cancer. Additionally, the use of adult CBCT protocols could lead to an excessive radiation dose in children, increasing the risk of malignancies.

This work is divided into 3 studies whose purpose is to assess the radiation doses in three standards pediatric CBCT protocol and suggest some other protocols that could be used for pediatric patients in order to decrease the absorbed dose.

In the first study was investigated the signal difference to noise ratio (SDNR) of scans at various kV of a Varian Clinac DHX linear accelerator, equipped with the Cone Beam for On-Board-Imager from Varian Medical Systems, in Clínica de Radiooncologia de Santarém, Portugal, in order to see where the best image quality parameter is reached while maintaining the same or lower absorbed dose with respect to a standard clinical protocol. The TOR 18 FG Phantom was used to acquire images from 40 kV to 150 kV in 10 kV steps at 25 mA and 50 ms exposure time in the clinical CBCT system. The data found was compared at different kilovolts and it has been found that the SDNR has peak at about 50-60 kV, meaning that it is possible to have an higher SDNR while maintain the same, or even lower dose with respect to clinical standard protocols.

In the second study spectra with voltages from 40 kV to 120 kV were experimentally acquired with an AMPTEK XR-100T-CdTe detector, in order to subsequently assess the radiation dose with Monte Carlo (MC) simulations and decrease the uncertainty on the radiation CBCT spectra. Acquired spectra were quite different from the ones obtained in literature. However,

since the filter materials after the anode of the X-ray system were not accurately known, standard literature spectra were used in MC simulations. In the third and last study, three CBCT protocols: Thorax, Head & Neck and Pelvic, were analysed at various energies with 10- and 15-year-old female anthropomorphic phantoms with MC simulations. Results indicate that using a voltage of 60 kV, the radiation dose could drop in Thorax protocol by an average of 28.93%, in Head & Neck protocol by an average of 39.02% and in Pelvic protocol by an average of 42.14%.

Sommario

La tomografia computerizzata a fascio conico (CBCT) è un sistema ampiamente utilizzato per la verifica pretrattamento e il posizionamento nella radioterapia guidata dalle immagini (image-guided-radiation therapy, IGRT). L'utilizzo della CBCT per questo tipo di tecnica consente di visualizzare i bersagli dei tessuti molli e le strutture critiche prima del trattamento, al fine di visualizzarne e verificarne la posizione del paziente. Inoltre, poiché l'imaging CBCT viene utilizzato quotidianamente e più volte per paziente, potrebbe comportare dosi cumulative di radiazioni potenzialmente dannose ai tessuti sani che circondano gli organi bersaglio esposti.

Bilanciare la dose di imaging e l'accuratezza del posizionamento è fondamentale nell'IGRT, soprattutto per i bambini, la cui maggiore suscettibilità biologica e un'aspettativa di vita più lunga li rendono più vulnerabili allo sviluppo di tumori secondari. Inoltre, l'uso di protocolli CBCT per adulti potrebbe portare a dosi eccessive nei bambini, aumentando il rischio di tumori maligni indotti dalle radiazioni.

Questo lavoro è suddiviso in tre studi il cui scopo è valutare le dosi di radiazioni in tre protocolli CBCT pediatrici standard e suggerire alcuni altri protocolli che potrebbero essere utilizzati per i pazienti pediatrici al fine di ridurre la dose assorbita.

Nel primo studio è stato analizzato il rapporto segnale/rumore (SDNR) di scansioni a vari kV di un acceleratore lineare Varian Clinac DHX, equipaggiato con il Cone Beam for On-Board-Imager di Varian Medical Systems, nella Clínica de Radioncologia de Santarém, in Portogallo, al fine di verificare a quale voltaggio si ottiene il miglior parametro di qualità dell'immagine mantenendo la medesima dose assorbita o una dose inferiore rispetto a un protocollo clinico standard. Il fantoccio TOR 18 FG è stato utilizzato per acquisire immagini da 40 kV a 150 kV in incrementi di 10 kV a 25 mA e 50 ms di tempo di esposizione nel sistema CBCT clinico. I dati rilevati sono stati confrontati a diversi kilovolt ed è emerso che il SDNR ha un picco a circa 50-60 kV.

Nel secondo studio sono stati acquisiti sperimentalmente spettri di raggi-X con voltaggi da 40 kV a 100 kV con un rivelatore AMPTEK XR-100T-CdTe, al fine di valutare successivamente la dose di radiazioni con simulazioni Monte Carlo (MC) e ridurre l'incertezza sugli spettri CBCT delle radiazioni. Gli spettri acquisiti erano diversi da quelli presenti in letteratura. Tuttavia, poiché i materiali dei filtri dopo l'anodo del sistema a raggi X non erano noti con

precisione, nelle simulazioni MC sono stati utilizzati gli spettri standard della letteratura. Nel terzo e ultimo studio, tre protocolli CBCT: “Torace”, “Testa&collo” e “Pelvi”, sono stati analizzati a varie energie con fantocci antropomorfi di 10 e 15 anni con simulazioni MC. I risultati indicano che utilizzando un voltaggio di 60 kV, la dose di radiazioni potrebbe diminuire nel protocollo “Torace” di una media del 28,93%, nel protocollo “Testa&collo” di una media del 39,02% e nel protocollo “Pelvi” di una media del 42,14%.

Index

Chapter 1

Introduction

Nowadays radiation therapy technique is image-based. Every stage of the radiation treatment process, from diagnosis, treatment planning, delivery, and follow-up after treatment, involves the use of imaging. Over the past forty years, breakthroughs in medical imaging have closely accompanied advancements in radiation [1].

Computed tomography (CT), which was first used in clinical settings in the 1970s, allowed medical professionals to peep inside the human body and non-invasively visualize the three-dimensional soft tissue architecture. Prior to the development of CT, soft tissue targets were difficult to see on planar radiographs, which forced treatment planning to be done in two dimensions (2D) [2].

Since Nakagawa et al. [3] first published the concept in 1998 and the technology became on sale in 2005, radiotherapy departments now have easy access to CBCT, a relatively new CT technology system incorporated into a radiotherapy treatment room. Before therapy or, more recently, during treatment, the CBCT system spins around the patient to acquire a series of 2D radiography projection images from a kV source and flat panel detector imaging system. Although not as good as a traditional fan beam CT scanner, these projection images can be used to reconstruct a 3D "volumetric" image with high resolution. The reconstructed CBCT images can be used to adjust the patient's position before treatment [4], [5]or as a foundation for tailoring the treatment plan [6], [7] to the patient's changing anatomy when radiotherapy is performed. Image guided radiation therapy (IGRT) is the term used to describe the capability to observe the target anatomy and surrounding organs at risk at the site of treatment delivery and to subsequently make changes to the patient position or the dose provided[8]. The On-Board Imager (OBI)[9] and Synergy system (XVI, X-ray volumetric imager) are the two primary commercial radiation CBCT systems from Varian and Elekta, respectively.

Every day and multiple times per patient, CBCT imaging is used, potentially exposing healthy tissues surrounding exposed organs to high cumulative imaging doses of up to 1-2 Gy [10], [11]. Because of this, CBCT has the potential to expose the patient's healthy tissues to a non-negligible radiation dose.

Instead of the treatment beams exclusively collimated to the tumour targets, CBCT scans can involve more unshielded normal tissues in repetitive scanning prior to several treatment fractions. Due to their longer projected lifespans and increased vulnerability to carcinogens, pediatric patients are more susceptible to the cumulative imaging risk [12]. Additionally, due to their smaller bodies when compared adults, infants receive a larger fractional imaging dosage from typical scanning settings [13], [14].

Manufacturer default imaging protocols are frequently made for adults and using them on children may result in a dose that is 2-3 times more than it would be for an adult [14], [15]. 'Child sizing' imaging procedures are therefore crucial. In pediatric radiation imaging, daily image guidance is common, but imaging techniques and procedures differ substantially between hospitals [16], [17].

Even though CBCT could be associated with a lower radiation dose than diagnostic CT, individual scans performed according to standard imaging guidelines may still result in up to 30 mGy of radiation over the course of several weeks of treatment [4], [10]. As an example, Ding and Coffey[18] calculated the dose to normal tissues supplied by a typical CBCT protocol, 125 kVp, 80 mA, 25 ms, and discovered that the dose was significantly influenced by the size of the patient, with larger doses delivered to normal structures in pediatrics compared to adult patients. As a result, it was discovered that the radiation dose to bone was 2 to 4 times higher than the dose to soft tissues, ranging from 4.5 to 8.4 Gy to bone over a 25 to 35 fraction period. This may be especially important for pediatric treatment, as bone growth can be impaired by bone dosage.

Numerous studies have evaluated the cancer risk that pediatric imaging involves to radiosensitive organs. For instance, Pearce et al. [19] discovered that cumulative doses of 50 and 60 mGy triple the risk of leukemia and brain cancer, respectively, with the risk for a single head CT being equal to one extra case for every 10,000 patients. This risk may be increased in cancer patients' children due to genetic predisposition, exposure to chemotherapy and radiation during treatment, among other factors. In comparison to single head CT, Zhou et al. [20] observed that the average cumulative imaging dose to the bone marrow and brain during CBCT imaging was 644 and 460 mGy, respectively, with an eight- and ten-fold higher lifetime attributable risk (LAR). Low-dose CBCT modes can significantly reduce the chance of developing cancer. Kim et al. [21] observed that with a single abdominopelvic CBCT scan at a regular and low-dose protocol, respectively, there was a reduction in lifetime attributable risk

for various organs ranging from 2.3 - 14.4 cases to 0.5 - 3.1 cases per 10 000. Although CBCT "may often be considered standard of care," the Royal College of Radiologists' Good practice guidance for pediatric radiotherapy [22] supports the use of technologies to lower imaging exposure in order to lower the overall radiation burden. Additionally, the Image Gently campaign educates the public on the importance of 'child sizing' the scanning parameters for diagnostic CT in order to best serve children [23], [24]. Many of these ideas can be used for CBCT image guidance, but as of now, there are not enough child-specific methods [16].

Concluding, CBCT images are mainly utilized for patient setup, target coverage assessment, and to find significant anatomical alterations that can affect dose distribution. Therefore, while diagnostic image quality is not required, IGRT requirements still call for appropriate quality. In a recent report, the Children's Oncology Group found that inadequate guidance was thought to be the primary reason why specific pediatric protocols are not implemented. The report concluded with recommendations to help optimize the protocol and emphasized the need for more research to establish pediatric imaging protocols [17]. Reducing exposure settings based on patient size and imaging purpose is one of the most used methods of dose reduction [13], [17], [25].

1.1 Purpose

In 2023, an estimated 9,910 children younger than 15 and about 5,280 teens ages 15 to 19 in the United States will be diagnosed with cancer [26].

In children under 15, leukemia makes up 28% of all childhood cancers diagnosed. The next most common type of childhood cancer is brain cancer (26%), followed by lymphoma (12%). In teens ages 15 to 19, brain cancer (21%), lymphoma (19%), and leukemia (13%) are the most commonly diagnosed cancers.

Rates of cancer in children and teens slowly increased since 1975, but those rates stabilized between 2010 and 2019. However, rates in teens continue to increase by around 1% each year [26].

Nowadays, the images acquired before therapy by CBCT are obtained from protocols that vary according to the body position of the tumour mass, but not according to the age, weight or anatomy of the patient. This means that the same scan is performed for a 2-meter adult

weighing 120 kg and a 1.10 meter tall 9-year-old child. In the field of radiation protection some important questions that could be raised are: “does the child need to receive the same beam at the same energy and size than the adult?”. Or “can we optimize the radiation dose by decreasing some exposure parameters such as energy and current?".

Another big problem is that if these procedures were done once, the risk would decrease a lot, but these scans have to be done before each radiotherapy treatment, which means that if a child is undergoing treatment, every week or every day he has to undergo additional radiation. The accumulation of radiation is a further important fact that is often overlooked because it is very difficult to observe its consequences [27].

The aim of the work is to study the radiation dose involved in CBCT imaging exposure for pediatric patients and try to increase the knowledge about parameters that could affect radiation dose in CBCT.

In order to reach this aim three studies were undertaken: 1) a study about the image quality at different energies levels was performed. Specifically, for each kV setting, it is studied a setting that allows for a better SDNR with the lowest absorbed dose; 2) measurements of clinical CBCT spectra through a CdTe detector that is able to acquire energy spectra in the diagnostic energy range; 3) finally, through MC simulations, a study about organs absorbed dose with 10 and 15 year old female voxel phantoms was performed taking into account several kV settings.

1.2 Cone Beam Computed Tomography

CBCT [28] is a medical imaging technology that enables high-resolution three-dimensional images of anatomical structures within the human body, using a cone-shaped X-ray beam.

CBCT is often used primarily in the dental field, as it allows dental and bone structures of the skull and jaw to be visualized with great precision. In addition, CBCT is used in several areas of medicine, such as orthopedics, interventional radiology, neurology, and cardiology, where high-resolution three-dimensional images are essential for planning surgical and diagnostic interventions. Since CBCT uses ionizing radiation, it is important to use it only when absolutely necessary and to keep radiation exposure to a minimum, especially in the most sensitive patients [29].

In CBCT, the X-ray tube emits X-rays in a cone-shaped beam in the direction of the patient sitting or lying on a supporting platform. The X-ray cone rotates around the patient's affected body part and a detector detects the attenuation of the X-rays through the biological tissue. The information gathered by the detector is then processed by a computer to create detailed three-dimensional images of the area of interest [30].
The CBCT image acquisition process can take only a few seconds, during which the patient must remain still. The process is non-invasive, and the patient does not have to undergo any special preparation.

Once acquired, the three-dimensional images can be displayed on a screen and manipulated to show different sections of the biological tissue. This allows the physician to examine the area of interest from multiple angles, providing a complete and detailed image of the anatomical structure [28].

X-ray attenuation through biological tissue is the process in which X-rays that are emitted from a radiation source interact with the biological tissue as they pass through the body. During this interaction, X-rays can be absorbed or deflected by molecules in the biological tissue, causing a decrease in X-ray intensity.

In general, biological tissues that have greater density, such as bone, attenuate X-rays more than softer tissues, such as muscles, skin, connective, epithelial, nervous tissues among others. This means that x-rays passing through bone are attenuated more, producing an image in which bone areas appear lighter than soft tissue areas [31].

The attenuation of X-rays through biological tissue also depends on the energy of the x-rays, as well as the thickness of the tissue passed through. In general, the higher the frequency and energy of the x-rays, the greater their ability to penetrate biological tissue and the more information that can be obtained from the scan [31].

The substantial advantages over other imaging techniques, Magnetic Resonance Imaging (MRI) and Positron Emission Tomography (PET) are [32]:

- Detailed anatomical visualisation: CBCT allows 3D images to be obtained, providing detailed visualisation of anatomical structures. This is particularly useful in the evaluation of tumours, as it allows the precise location and size of the tumour to be identified.
- Non-invasive and relatively fast imaging technique: which makes it possible to decrease the presence of motion artefacts.
- Cost: less expensive than other advanced imaging techniques.

Figure 1. Varian Clinac equipped with CBCT On-Board-Imager [35].

Figure 2. Modern Medical CT [36].

1.2.1 Differences between CT and CBCT

Below the main differences between a common CT and a CBCT [33], [34]:

- *Differences in components and image acquisition:* A CT scan consists mainly of four parts: the X-ray generator, a series of collimators to direct the beam towards the intended target, a ring of detectors and a computer. Then we can add a mobile table on which the patient is placed, a system for moving the ring of detectors to acquire images from different angles, and a patient monitoring system to ensure safety during the examination (*Figures 1-2.*) [35], [36]. CT and CBCT mainly differ on collimators and the detectors [34].

  The collimator of a CT has an adjustable aperture that defines the width of the x-ray beam, and this allows the spatial resolution of the image to be controlled, giving the x-ray field a "fan-like" shape (*Figure 3a*). Whereas in CBCT, the collimator is used to limit the field of view of the image, focusing specifically on the area of interest, reducing the dose to surrounding healthy organs [34].

  About the detector, CT uses a 360-degree system of detectors that acquire multiple images of the patient's body from different angles. While CBCT uses a cylindric-shaped detector system to acquire cross-sectional images of the patient's body because the beam is cone-shaped with circular sections (*Figure 3b*).

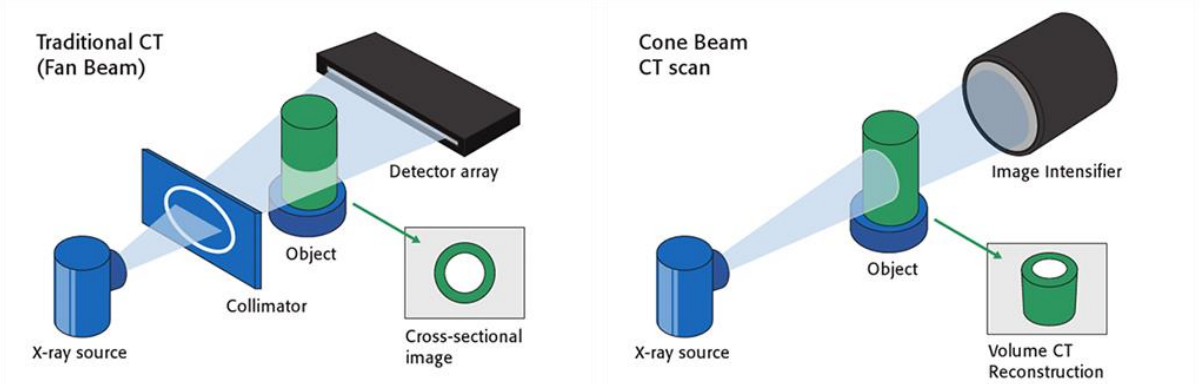

Figure 3. a) Fan Beam Computer Tomography. b) Cone Beam Computed Tomography [35].

- *Differences in use*: conventional CT is mainly used for medical diagnostics. It produces detailed images of cross-sections of the body that allow anatomical visualisation and detection of abnormalities or pathologies, including tumours. CBCT is mainly used in the field of medical imaging and provides three-dimensional images that allow radiotherapy treatment to be precisely guided.

- *Resolution differences:* CTs offer high spatial resolution and superior image quality compared to CBCTs. This makes them suitable for precise and detailed diagnosis of pathologies. While CBCTs have a slightly lower spatial resolution, they are optimised to provide sufficiently detailed images for radiotherapy treatment guidance. The image quality is balanced to provide useful information for treatment planning and guidance[37].

- *Dose differences*: The radiation dose emitted during a CT scan is generally higher than during a CBCT scan. This is due to the larger amount of data collected by CT and the need to perform more scans of the patient's body. On the other hand, CBCT should be performed before any radiation treatment to verify the correct location of the suspicious mass, potentially it can be used even multiple times per week for few months, so the radiation dose could accumulate [38].

Figure 2. Varian Clinac equipped with CBCT On-Board-Imager [35].

Figure 3. Modern Medical CT [36].

1.3 Low dose effect in pediatric patients

Radiological imaging today is still nowadays considered the secondary prevention that is able to reduce thousands of cancer deaths [39].

Health risks for humans are evident for ionising radiation above 100 mGy where the first deterministic side effects start to appear, while stochastic risks, such as cancer, cannot be predicted or even neglected at lower doses [40]. Nowadays, effective doses from pediatric CT examinations are between 1 and 30 mGy [41].

Even more importance should be given to children, since they have more sensitive cells and organs, there is a greater chance of harmful effects than in adults [40], [42]. Moreover, if protocols suitable for smaller bodies are not used, the radiation exposure could be much higher, up to 10 times increasing the risk of cancer compared to an average adult [43].

The last decade has shown a particular increase in radiological imaging in children [44] and since 2000 an increase in the incidence of cancer after childhood CT scans has been reported [44]–[47]. Despite this increase there has not yet been any scientific research that connects the risk of developing cancer due to diagnostic or therapeutic interventions. This could be partially due to the fact that studies are still very limited, and it is costly to carry them out for decades [48]–[50]. Even if there is a lot of debate in literature about this issue it is always useful to try to minimize radiation exposure to children [51].

With the discovery of CT and its increasingly intensive use, it was decided to create guidelines. Diagnostic reference levels (DRLs) are one of the main operational tools for optimising patient protection in radiological imaging [52]. While CBCT is a relatively new technology, there are no dose reference levels set yet.

Back in 1999, the International Commission published 'Radiation Protection (ICRP) 109: Guidance on diagnostic reference levels for medical exposure' [53]. This is the first document highlighting the need to establish standards for medical examinations that lead to increased radiation exposure such as CT and interventional radiology (IR) examinations, emphasizing the role of pediatric DRLs and introducing European DRLs for 5-year-olds.

Despite this, some articles were written in the American Journal of Roentgenology [29], [54], [55] in the early 2000s highlighting the problem of high radiation exposure in pediatric CT

scanning. During the same period, a survey of pediatric CT scanning methodology came out, showing that many hospitals still use adult scan settings for children.

In the same year, the European Commission conducted a study to verify the use of DRL at a European level [56]. Questionnaires were sent to 36 countries in Europe to understand the development and problems with DRLs. The results were negative, it was found that most countries either did not have up to date DRLs or were taking old standards from the European Commission or even from other countries, without reference to their own patients.

It has been found that in pediatrics, the main problem was the absence of guidelines. In fact, body size is very variable, so it is not possible to use the approaches used for adult patients, i.e., to take a standard, medium-sized phantom. For children, it is necessary to divide the measurements into multiple studies, but as there are no clear and precise regulations, for adolescents aged 5 to 18, these have never been done.

In 2013, the European Commission became aware of the need to optimise radiation protection for children and launched the PiDRL project [57], with the aim of creating European guidelines on diagnostic reference levels for pediatric imaging.

The main aims of this competition were:

- Write down a precise method to define and use DRLs for pediatric diagnosis and treatment.
- With the results of new studies, new knowledge and new technologies, update and augment old European DRLs to standardize with many procedures as possible by age/weight of patients.
- Bring the whole Europe to the knowledge and use of DRLs to optimize radiological therapies and eliminate barriers between different states.

After several years of analysis and studies, the result of this project was the publication of a set of guidelines and recommendations concerning the implementation and use of DRLs in children. The European Commission approved this document, and it was made available through the publication of issue 185 of the Radiation Protection series [52].

Within this document it is important to remark some CT and a CBCT recommendation.

Firstly, the recommended anatomical regions should be analysed.

Table 1 shows the list of CT examinations for which DRLs are recommended. As it can be seen, examinations of the extremities of the body are excluded because they absorb a relatively low dose and do not contribute much to the collective effective dose [52]. The analyses done for the "head" and "neck" protocols are done with the 16 cm phantom, while the others with the 32 cm phantom.

Table 1. CT examinations where the DRLs should be set [52]

Anatomical region	**Procedure**
Head	Routine Paranasal sinuses Inner ear/internal auditory meatus Ventricular size (shunt)
Neck	Neck
Chest	Chest
	Cardiovascular CT angiography
Abdomen	Abdomen (upper abdomen)
	Abdomen+pelvis
Trunk	Whole body CT in trauma
Spine	Cervical spine
	Thoracic spine
	Lumbar spine

Scanning protocols must be optimised not only by body section, but also for specific patient groups. Particular attention must be paid to the grouping of patients for pediatric DRLs, as the size of children, and thus the dose levels, vary significantly not only by age, but also by weight. Adult sizes usually vary by a factor of 4 (40-160 kg body weight), while pediatric patient sizes vary from premature infants (e.g., 300-400 g) to obese adolescents (> 80 kg body weight) by a factor of more than 200. The classification of DRLs should also consider a child's steep growth pattern: within the first six months of life a child's body weight doubles and during the first year its weight triples [52].

Table 2-3 show three different types of division by age and weight that have been made to divide the various children in childhood. However, the first two columns comparing weight and age are to be taken as approximate data and cannot be equated with DRLs. Usually, the most commonly used grouping is the third column in which the DRLs are calculated, showing that between the ages of 0 and 15 years there are five different categories on which the parameters can be calculated [52].

Table 2. Recommended grouping patients for pediatric DRLs [52].

Recommended weight groups (intervals) for *body* examinations	Recommended age groups (intervals) for *head* examinations
< 5 kg 5 - < 15 kg 15 - < 30 kg 30 - < 50 kg 50 - < 80 kg	0 - < 3 months 3 months - < 1 y 1- < 6 y ≥ 6 y

Table 3. Approximate equivalence of weight and age groups for the purpose of comparing weight-based DRLs with age-based DRLs [52].

Description	Weight group	Age group based on weight-for-age charts	Most common age groups used for the NDRLs (or equivalent)
Neonate	< 5 kg	< 1 m	0 y
Infant, toddler and early childhood	5 - < 15 kg	1 m - < 4 y	1 y
Middle childhood	15 - < 30 kg	4 - < 10 y	5 y
Early adolescence	30 - < 50 kg	10 – < 14 y	10 y
Late adolescence	50 - < 80 kg	14 - < 18 y	15 y

After categorizing patients by age and scanning protocols by anatomical part, it is possible to calculate the effective dose for each combination.

The standard dose values analysed in CT for defining DRLs are the volume effective dose, Computed Tomography Dose Index (CTDIvol), and the Dose Length Product (DLP), determined for a 32 cm phantom for CT examinations of the chest, abdomen, trunk, and spine and for a 16 cm phantom for CT examinations of the head.

The CTDIvol is used to calculate the dose per single slice, while the DLP for the dose of the entire CT scan. In modern CT scanners, both the CTDIvol and DLP are available from the console and can also be retrieved automatically from the structured radiation dose reports for automatic dose management [52] (see chapter 2.2.2 for reading more).

Table 4. European DRLs for CT. EDRLs for head CT refer to 16 cm phantom and EDRLs for thorax and abdomen for 32 cm phantom. DRLs refer to a complete routine CT examination (one scan series) [52].

Computed tomography			
Exam	Age or weight group	**EDRL**	
		$CTDI_{vol}$, mGy	**DLP, mGy cm**
Head	0-<3 months	24	300
	3 months-<1 y	28	385
	1-<6 y	40	505
	≥6 y	50	650
Thorax	<5 kg	1,4	35
	5-<15 kg	1,8	50
	15-<30 kg	2,7	70
	30-<50 kg	3,7	115
	50-<80 kg	5,4	200
Abdomen	<5 kg		45
	5-<15 kg	3,5	120
	15-<30 kg	5,4	150
	30-<50 kg	7,3	210
	50-<80 kg	13	480

Based on this initiative, in 2013 in the publication 185 of the Radiation Protection series [52], there is a document with guidelines to try to adhere to regarding the most commonly used ionizing source machines in the hospital.

The guidelines cover all types of pediatric radio diagnostic examinations and procedures: plain radiography, fluoroscopy, CT, and IR. They focus on CT, IR, and digital projection. However, they do not yet address pediatric imaging in nuclear medicine in order to avoid adding difficulties and potential errors to the societies and organizations that are dealing with it [52].

In this work the radiation dose of a CBCT in pre-treatment imaging, was analysed, in two female phantoms aged 10 and 15 years, in the three main body regions: chest, abdomen and head.

Since for this type of set up there are no standard procedures to analyse and optimize the radiation dose, it is vital to try to decrease the exposure to ionizing radiation trying to define new CBCT DRL guidelines.

Chapter 2

Physical Principles

2.1 Interaction of Radiation with Matter

CBCT is a medical imaging technique that uses a rotating X-ray cone beam to acquire high-resolution, three-dimensional images of a specific area of the body. During the procedure, the X-ray cone passes through the patient and is detected by a sensor, recording the photon energy through the tissue. This data is processed by a computer to create a three-dimensional representation of the area of interest [25]. X-rays are a form of electromagnetic radiation consisting of high-energy photons that are ionizing radiation.

The main characteristic of ionising radiation is its ability to ionise atoms and molecules, so to remove electrons from them. There are several types of ionizing radiation: alpha particles, beta particles (electrons and positrons), photons, protons and neutrons.

Charged particles (electrons, protons, and alpha particles) interact with the orbital electrons of atoms in the medium through collisions and ionisation, rapidly losing their kinetic energy. Therefore, charged particles have a defined range within a medium, which varies depending on the initial energy of the charged particle, whereas photons do not have a defined range within a medium, their penetration power being characterised by attenuation in the medium [58].

2.1.1 Photon interactions

Photons are electrically neutral particles that move at the speed of light, *c,* and, unlike electrons, have the ability to travel a certain distance inside a material without interacting [59].

This distance depends on the characteristics of the material and the energy of the photons:

$$E = h * \nu \; ; \qquad \textit{(Eq. 1} \text{ [60])}$$

where h is Planck's constant (6,626068 x 10^{-34} m^2 kg/s) and v is the frequency.

When photons interact with matter, there is a reduction in the number of these particles as a function of the beam direction, as absorption and scattering phenomena occur.
The interaction probability depends on the energy of the photon, and the atomic number of the attenuating material, Z.
The intensity I (x) of a photon beam passing through a medium of thickness x, can be represented by *(Eq.2)*:

$$I(x) = I(0)e^{-\mu(h\nu, Z) * x}; \qquad \textit{(Eq. 2 [61])}$$

where " μ " represents the proportionality constant called the linear attenuation coefficient that depends on the properties of the material itself and the energy of the photons, and " x " the thickness of the material passed through.

Eq. 2 characterises the passage of electromagnetic radiation through matter and is known as the Lambert-Beer law [61].

The x-ray attenuation law describes how the intensity of an x-ray beam decreases in relation to the density of the material passed through. In general, when an x-ray beam passes through a material, some of the photons may be absorbed, scattered, or deflected from their trajectory. Absorption is the main cause of attenuation of the x-ray beam.

The linear attenuation coefficient μ is inversely proportional to the energy of the photons, which means that low-energy photons are more easily absorbed than high-energy photons. This has an impact on the choice of photon energy used for computer tomography, as the choice of energy influences the amount of absorption of the material and, consequently, the quality of the image produced. For a poly-energy photon beam, which interacts with matter through different processes, the total μ will include all partial coefficients of all types of interactions.

There are four processes by which charge-free radiation interacts with matter: 1) Rayleigh scattering, 2) photoelectric effect, 3) Compton effect and 4) pair production [62].

The last three are the most important, as they result from the transfer of energy to the electron. These effects depend on the energy of the incident photons, the atomic number, and the density of the medium. *Figure 4* shows this relationship:

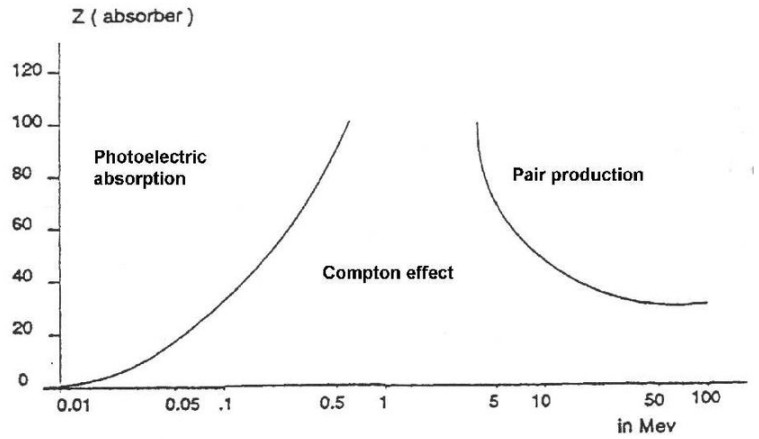

Figure 4. Regions of relative predominance of the three main forms of interaction of photons with matter.

The photoelectric effect is predominant for photons with low energy and high Z. The Compton effect is predominant for photons with intermediate energies. Pair production is more important when energy and atomic number are higher [62].

2.1.2 Photoelectric effect

It's the process in which a photon of energy $E = h * \nu$, collides with an atomic electron and an orbital electron is ejected causing a gap. In this process, all the energy of the incident photon is transferred to the ejected electron (*Figure 5*).

For this process to occur, the energy of the incident photon must be greater than the electron's binding energy to the nucleus (φ).

The kinetic energy of the emitted electron is given by the equation:

$$Ec = h\nu - \varphi\ ; \qquad (Eq.\ 3\ [63])$$

The gap in the atom can then be filled by an electron from an outermost layer with characteristic X-ray emission or by an Auger electron [64].

This effect is the dominant interaction process for energies between 0.5 keV and 0.5 MeV and in tissues with a low atomic number, such as soft tissue.

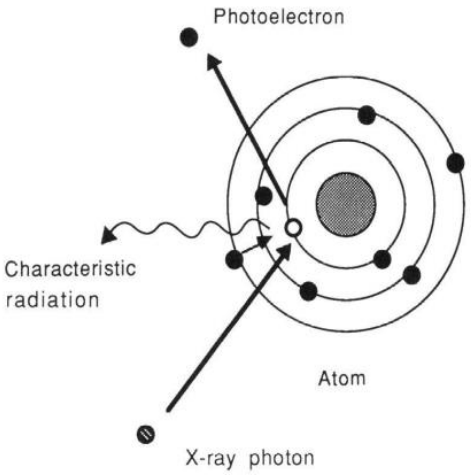

Figure 5. Photoelecric effect [63].

2.1.3 Compton effect

This process consists of the interaction between a photon and an electron in the outermost layers of the weakly bound atom of the biological tissue, whereby the incident photon gives up part of its initial energy (h * ν) and is deflected with a lower energy (h * ν') and angle (Θ), but can continue to interact with other atoms in the tissue, contributing to the decrease in the intensity of the x-ray beam passing through the tissue [65]. The electron that has interacted with the photon is scattered with an angle (ϕ) and energy that depend on the photon's initial energy (*Figure 6*). Since the Compton effect essentially involves free electrons, it is independent of the atomic number Z. As the energy increases, Compton effect interactions decrease, resulting in the production of pairs.

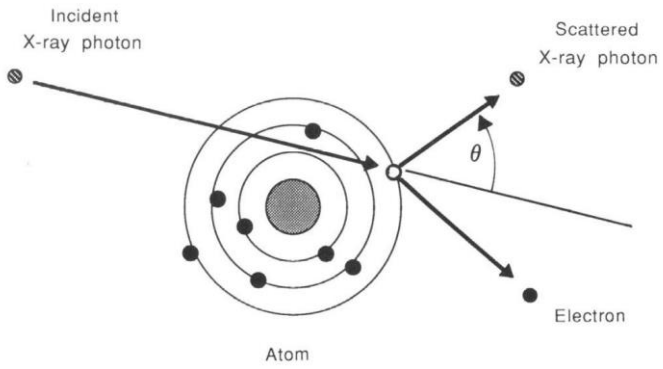

Figure 6. Compton effect [63].

In radiotherapy, the Photoelectric effect is most prelevant in CBCT because the voltage range used for imaging is 100 kV to 125 kV [66], while the Compton effect is predominant in therapy because the average energy of the treatment beam is between 1 and 15 MeV and the tissue has a $Z_{effective}$ of about 7 [65].

2.2 Dosimetry

Dosimetry is a discipline that deals with the measurement and assessment of radiation doses absorbed by a system or an individual exposed to ionising radiation sources. Interest in dosimetry has grown in parallel with the advancement of radiological and nuclear technologies. This branch of physics arose from the need to understand the effects of radiation and to develop methods to measure and quantify radiation exposure [67]. Nowadays it is fundamental in several fields, including radiotherapy, radio diagnostics, radiation protection and nuclear research. Firstly because it contributes to patient safety by assessing the amount of radiation absorbed during examinations and treatments. This allows the radiation dose to be kept within safe limits, avoiding risks to the patient's health. Secondly, radiological dosimetry optimises diagnostic and therapeutic procedures by balancing high quality images with radiation dose minimisation. Furthermore, it supports research and development in medical imaging and radiotherapy, enabling the evaluation of new techniques, equipment, and protocols to improve the efficacy and safety of radiological procedures. [68]

2.2.1 Dosimetry quantities

2.2.1.1 Energy transferred.

Considering a certain volume of matter (V) within which there is a flow of incoming photons ($\psi\gamma$,in = energy of incoming photons) and one of outgoing photons ($\psi\gamma$, out = energy of outgoing photons); remembering that photons can induce the formation of a pair, there will be a mass exchange (Δm) that will correspond to an energy that is given by the product of this mass exchange by the square of the speed of light ($\Delta m \cdot c^2$).

The energy transferred (ϵtr) will be given by the energy of the incoming photon flux (incoming energy) minus the energy of the outgoing photon flux (outgoing energy) minus the energy corresponding to the mass that is created due to the formation of a pair[67].

2.2.1.2 Kerma

Kerma stands for kinetic energy released to matter, i.e., the amount of energy that is deposited in a given volume of biological tissue and is calculated as the ratio of the energy transferred to the mass m present in the volume of matter V considered:

$$\kappa = \epsilon tr / m; \qquad \textit{(Eq. 4}[42]\textit{)}$$

It is expressed in Gray per unit mass (Gy/kg) [42].

In the study we also discuss about Air Kerma which is the amount of kinetic energy released in a defined volume containing air (ρ=1,225 kg/m³). Useful for calibrating and normalizing Dose values in volumes with other densities.

2.2.1.3 Energy imparted

Considering that we have a volume V with an incoming photon flux and an incoming charged particle flux, and also an outgoing photon flux and an outgoing charged particle flux the energy imparted ϵ by ionising radiation to matter of mass m in a volume V is defined as the sum of the total incoming energy (given by the sum of the energy of the photon flux and the incoming particle flux) minus the sum of the total outgoing energy (given by the sum of the energy of the photon flux and the outgoing particle flux) and minus the energy corresponding to the mass that is created when a pair is formed:

$$\epsilon = (\psi\gamma,in + \psi charge,\text{in}) - (\psi\gamma,out + \psi charge,out) - \Delta m \cdot c^2 ; \quad \textit{(Eq. 5}[67]\textit{)}$$

In practice, if we have several incoming radiations and several outgoing radiations from volume V, we make up the difference, and also subtract the energy due to the creation of new particles, we obtain the kinetic energy released within the volume considered [42].

2.2.1.4 Dose

The dose (D) is the energy delivered for the mass contained in the volume, it is the energy released by the radiation in volume V divided by the mass. The most commonly used unit of measurement is the Gray (1G = 1J/1kg). Compared to kerma, the dose represents exactly the energy that is released within the volume [42]:

$$D = \epsilon / m; \qquad \textit{(Eq. 6 [68])}$$

- Absorbed dose [42]: is defined as the energy absorbed per unit mass of biological tissue and is expressed in Gray (Gy). It represents the amount of energy that is absorbed by biological tissue.

- Effective dose [42]: Absorbed dose is a strictly physical concept and is limited in that it has no direct relationship to the risk of radiation-induced damage. The concept of effective dose was introduced by the ICRP to compare the delayed radiation risk from different types of human irradiation. So, it represents the sum of the equivalent doses weighted for the effect on the biological tissue, i.e. it takes into account the sensitivity of the various tissues to the radiation. It is also expressed in sieverts (Sv) and is a measure of the total radiation dose to the biological tissue *(Eq. 7)*.

The latest tissue weighting factors were published in IRCP 103 in 2007, showed in *Table 5*.

$$E = \sum_t H_t \cdot w_t \; ; \qquad \textit{(Eq. 7 [68])}$$

Table 5. Tissue weightening factor for effective dose [42].

Tissue	w_t
Red bone-marrow, Colon, Lung, Stomach, Breast	0.12 each
Gonads	0.08 each
Urinary bladder, Esophagus, Liver, Thyroid	0.04 each
Endosteum (Bone surface), Brain, Salivary glands, Skin	0.01 each
Remaining tissues: Adrenals, extrathoracic airways, gall bladder, heart, kidney, lymphatic nodes, muscle, oral mucosa, pancreas, prostate, small intestine, spleen, thymus, uterus	0.12 combined

- Equivalent dose: is defined as the product between the absorbed dose and a radiobiological weight factor (WR), which takes into account the type of radiation incident and the biological tissue irradiated. It is expressed in sieverts (Sv) and is a measure of the effective dose of radiation to biological tissue [69].

- Dose coefficent: is a parameter used in dosimetry to estimate the radiation dose absorbed by a specific organ or tissue in the human body as a result of exposure to a source of ionizing radiation. The dose coefficient represents the amount of dose absorbed per unit of activity or exposure of the source. It is specific to each type of radiation and to each organ or tissue in the human body. It is usually expressed in units of dose per unit of activity or exposure, such as sievert (Sv) per becquerel (Bq) or sievert (Sv) per coulomb per kilogram (C/kg) [69].

In summary, the main difference between these parameters lies in the way they consider the biological effects of radiation on tissue. Kerma and absorbed dose measure the amount of energy deposited and the amount of energy absorbed by biological tissue, respectively. The equivalent dose takes into account the type of radiation and the biological tissue irradiated, while the effective dose also takes into account the sensitivity of the tissue to the radiation.

2.2.1 Dosimetry quantities in CT

For the assessment of the effective dose in CT, one of the main parameters is the Computed Tomography Dose Index (CTDI) [70], which represents the integral of the absorbed dose profile for a single scan.

It is calculated it as:

$$CTDI = \frac{1}{nT}\int_{z1}^{z2} \mathrm{D(z)\ dz;} \qquad \textit{(Eq. 6 [70])}$$

Where:

- z1, z2 = integration limits along the z-axis, i.e., scan length;
- D (z) = dose quantity along a single axial scan;
- n = the number of layers acquired simultaneously (n=1 for a single-layer tomograph, n=4 for a 4-layer tomograph, etc.);
- T = the nominal layer thickness or the detector group width in the case of multislice CT.

The CTDI can be measured using a 10 cm long stylus ionisation chamber aligned with the z-axis of the CT and irradiated with an axial scan. In this case the formula has precise integration limits as z1 and z2 are equal to ± 50 mm covering a total length of 100 mm and is usually written as CTDI100 where "100" indicates the length over which the integration was performed [71].

The CTDI represents a measure of all the absorbed dose along the length of the chamber as if this dose were all concentrated within the nominal acquired layer, while the CTDI100 represents the absorbed dose in 100 mm.

The main problem is that the dose distribution in the exposed area from the centre to the periphery of the puppet is generally not uniform.

By taking several measurements at different angles of the phantom it is possible to find the point where the dose is maximum and establish a representative average, however, they are not very accurate and depend on the parts of the body, for example, CTDI100 values measured at peripheral positions of the head puppet are often similar to the values measured at the centre of the puppet, but if I have to take a general value that applies throughout the body, for example in the chest the values at the periphery are generally about twice as high as the values measured at the centre of the phantom. The exact ratio depends on the effective energy of the X-ray beam e the shape of the beam.

For this reason, it's calculated the CTDIw *(Eq. 9)*, the weighted CTDI [72].

The values obtained at the centre of the phantom can be combined with the values at the periphery to obtain a weighted mean value expressed as:

$$CTDI_W = \frac{1}{3} * \mathrm{CTDI}_{CENTER} + \frac{2}{3} * \mathrm{CTDI}_{PERIPHERAL} \qquad \textit{(Eq. 9 [72])}$$

Where CTDI100,centre and CTDI100,peripheral are measured at the centre and periphery of the phantom respectively. The value at the periphery is an average of at least four measurements at different angles around the phantom.

The CTDIw, thus defined, does not take into account the volume of the body that is scanned in the spiral movement of the CT; the IEC edition on CT safety standards uses a new CTDIvol index, i.e., the CTDIw corrected for 'pitch', a value that is used nowadays [73].

The pitch is the ratio between the couch advance (t) for a 360° rotation and the total collimation of layer x (x = N × T, where N is the number of layers and T the nominal layer thickness), i.e., it indicates how much anatomy is covered in one rotation of the X-ray tube. A higher pitch value indicates that the table is moving faster than the imaging speed, which means that more anatomy is covered with fewer images.

To calculate the total exposure, the dose length product (DLP), measured in [Gy*cm] it must multiply by the scan length:

$$DLP = CTDIvol * length; \quad \textit{(Eq.10 [74])}$$

In this work, it is used a CBCT. This type of machine can be seen as a transition from scanning one or a few layers to volumetric acquisition (CTMS > 4 layers), thus implying a transition from a fan beam type geometry to a cone beam type geometry. It is assumed in the literature that if the angle subtended by the external detectors is less than 1°, the opposite beams for an external detector will have an offset less than the thickness of the layer, so the beam is fan beam type, and the geometry can be considered planar. On the contrary, if the angle subtended by the outer detectors is greater than 1° then the opposite beams for an outer detector will have an offset greater than the thickness of the layer, so the beam is cone shaped[75].

Chapter 3

Studies Specific Aim

3.1 SDNR Analysis in a TOR phantom's CBCT Images

In the first study, there is the will to investigate whether the kilovoltages of CBCTs used at the diagnostic level are the most effective from a signal difference-to-noise ratio point of view. The clinical protocol choices nowadays mainly range from 100 kV to 125 kV [66].

In this experimental work, the SDNR from 40 kV to 150 kV in steps of 10 by the clinical imaging system: linear accelerator Varian CLINAC DHX, equipped with the CBCT OBI Varian Medical Systems in Santarem, PT.

For this purpose, analysis were performed with a TOR 18FG, to check whether it is possible to maximize the SDNR with the lowest absorbed dose possible.

Then, the best energy that maximizes the SDNR, was used for study III, by changing the kV spectra in the MC simulations.

3.2 Experimental Acquisition of CBCT Spectra

In the second study, experimental energy spectra from 40 kV to 100 kV in steps of 20 kV were acquired. The acquired spectra were produced by linear accelerator Varian CLINAC DHX, equipped with the CBCT OBI Varian Medical Systems in Santarem, PT.

The main aim of this study was twofold: i) to analyse real CBCT spectra, since, to the best of our knowledge, there is very poor information in literature about this radiation spectrum type; ii) to compare literature spectra with the experimental ones, by using both in Study III (Monte Carlo simulations) to calculate the organ radiation doses, through the anthropomorphic voxel phantoms.

3.3 Dose assessment in pediatric CBCT

In the third study, two pediatric computational phantoms, 10- and 15-years-old from the ICRP, were considered to carry out Monte Carlo simulations, with Penelope MC code, in which digital models of the phantoms and the CBCT beam at different energies were integrated.

The aim was to calculate the relative variation of absorbed radiation dose, after a CBCT scan, for different protocols currently in use in pediatric settings (head-thorax-pelvis) in the most affected organs and to compare the results between the standard clinical protocol with the ones obtained with the voltage that maximise the SDNR found in study I.

Chapter 4

Materials and Methods

4.1 Materials and Methods – Study I: SDNR Analysis in a TOR phantom's CBCT Images

In this study the following main issues will be described:

- TOR 18FG phantom for imaging purposes;
- CBCT X-ray machine able to produce the spectra for images acquisition and geometry irradiation setup;
- SDNR analysis of the acquired images.

4.1.1 Experimental Setup

4.1.1.1 TOR 18FG Leeds Test X-ray Phantom

In this work the TOR 18FG Leeds Phantom, in *Figures 7-8*, was used [76], a phantom that is usually used for calibration or evaluation of image quality in a given medical imaging modality, such as CT. It is mainly used to check the spatial resolution, linearity, distortion, and other characteristics of images produced by an imaging system, such as visualizing different contrasts. In fact, it's built to be used routinely by radiographers to check the imaging performance of conventional image-intensifier fluoroscopy and fluorography systems.

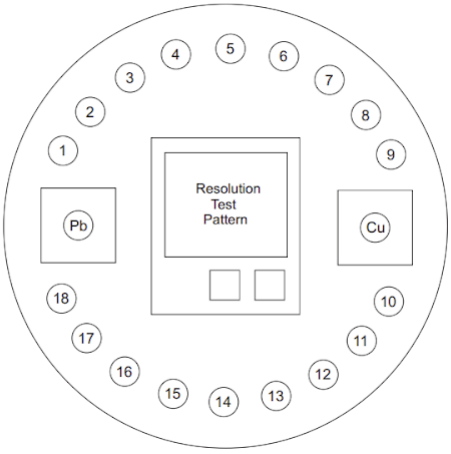

Figure 7. Layout of the TOR 18 FG details (not in scale) [78].

Figure 8. TOR 18FG Phantom with instruction manual [78].

The ability of an X-ray system to image low-contrast details depends on the levels of noise and contrast loss (due to scatter) [77]. The phantom has 18 circular discs, with the diameter 8 mm, forming a series of gradually decreasing contrasts, and the measurement consists of determining which discs at different voltages have better contrast and thus better SDNR. At each energy value the contrast of these discs changes, and the SDNR in 3 different discs, specifically at low, medium and high density, was analysed.

The following table gives the X-ray contrasts of the discs for beam conditions of 70 kVp (constant potential) with 1 mm copper filtration. These should be regarded as nominal values; actual contrasts will depend on the kV waveform, etc. They are also subject to manufacturing tolerances of ±5% [78].

For the study were used discs 1 - 5 - 9 in *Figure 7* with respectively of 0.167 - 0.088 - 0.045 levels of contrast.

Table 6. Contrast value in TOR18FG, highlighted (*) the three chosen discs [78].

Disc Number	Contrast	Disc Number	Contrast
1*	0.167*	10	0.039
2	0.148	11	0.03
3	0.128	12	0.027
4	0.109	13	0.022
5*	0.088*	14	0.017
6	0.075	15	0.015
7	0.067	16	0.013
8	0.053	17	0.011
9*	0.045*	18	0.009

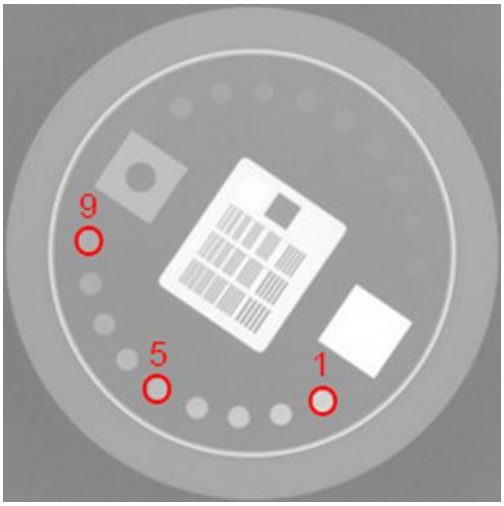

Figure 9. 40 kV scan of TOR18FG with ROI selected for the study highligthened.

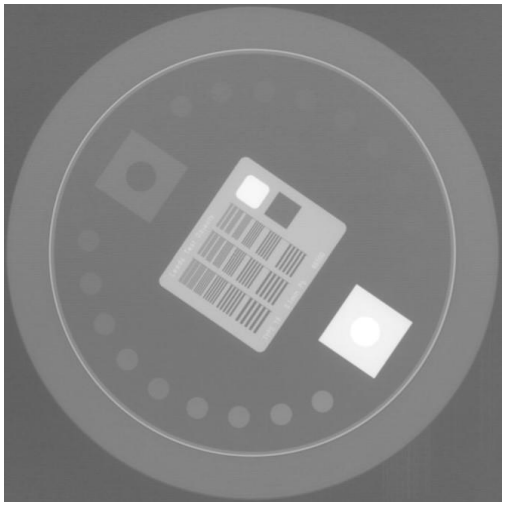

Figure 10. 70 kV scan of TOR18FG.

The *Figure 9* is acquired with a current of 25mA, at 100 cm, 0.05s of exposure time and 40 kV, while the *Figure 10* with 120 kV voltage and other same parameters. As you can see the contrast of discs in the upper right of the image is really low so, we decided to use the number 1-5-9.

The measurements should be made at a fixed distance from the monitor because viewing distance affects the perception of image noise. The recommended distance is about four times the diameter of the monitor circle, although this is not critical. In this study a common clinical CBCT distance of 100 cm was used [78].

In addition, this phantom has two copper and lead plates for evaluating differences and in the central part a Resolution Test Pattern, details which were not used in this study.

4.1.1.2 CBCT Machine

All measurements were performed on the Varian Clinac DHX linear accelerator, equipped with the Cone Beam for On-Board-Imager from Varian Medical Systems [79], in Clínica de Radioncologia de Santarém, Portugal.
The OBI (On-Board-Imager) system allows for precise treatment in radiotherapy [80]. It is mounted orthogonally to the MV beamline and consists of a kV tube and an amorphous silicon detector, which can be calibrated to variable imaging conditions.

This system has the capability to image in either radiographic 2D, fluoroscopic 2D+time, or volumetric 3D modes. For simplicity SDNR only in 2D mode were evaluated because the phantom is specifically produced for 2D imaging.

It is safe to mention that CBCT images are mainly acquired in 3D mode. However, the impact of these approximations will be better discussed in the "Limitation" section of Chapter 7.1.

With this machine has been generated conical X-ray beams at different voltages 40 kV, 50 kV, 60 kV, 70 kV, 80 kV, 90 kV, 100 kV, 110 kV, 120 kV, 130 kV, 140 kV and 150 kV, maintaining the same current, 25 mA. This current value was chosen to have a good compromise among noise and saturation of the acquired images. The distance between the X-ray tube and the test object phantom was always of 100 cm with an exposure time of 50 ms.

4.1.1.3 Setup and Procedure

For all the measurements, the phantom was aligned, *Figure 11*, with the lasers to position the isocenter at the center of the phantom.

12 images were acquired with a single 50 ms scan, at different voltages from 40 kV to 150 kV with the same current 25 mA and same distance from the tube of 100 cm, *Figure 12*.

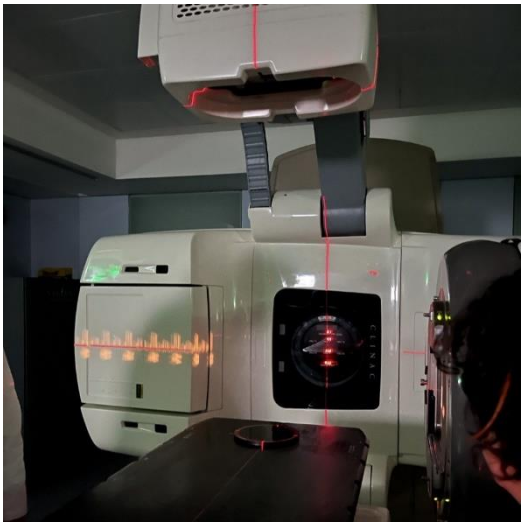

Figure 11. Aligning the CBCT with the TOR Phantom.

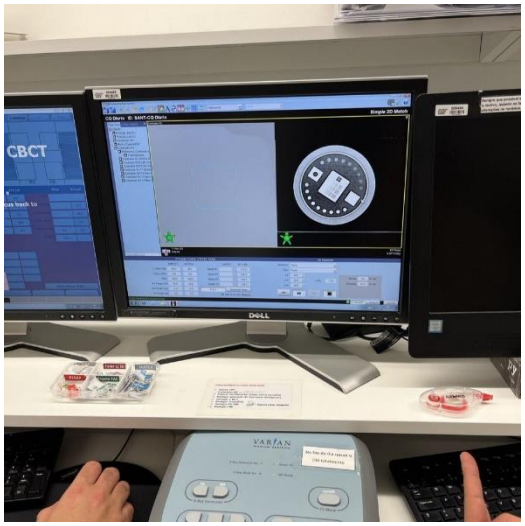

Figure 12. Early results after CBCT scans.

4.1.2 Methods of Analysis

4.1.2.1 SDNR Analysis

The Signal Difference -To-Noise Ratio (SDNR) was evaluated for each acquired image.

SDNR is defined as [81]:

$$SDNR = \frac{|MVP_{ROI} - MVP_{BKG}|}{\sigma_{BKG}}; \qquad \textit{(Eq. 11 [81])}$$

Where MPV is the average intensity of a 242 pixels ROI placed in the selected discs and MPV_{bkg}, σ_{bkg} are the mean signal and standard deviation of the ROI in background, respectively.

To calculate the SDNR, a ROI with an area of 242 pixels was selected, both in the background and in the contrast object area. Then, ImageJ software [82] was used to calculate the average intensity and standard deviation of the selected ROIs.

For the choice of the background region 4 zones were chosen, in order to have a more homogeneous area.

Next, for the calculation of the SDNR, the difference between the mean intensity of the ROI and the mean intensity of the 4 background values was divided by the mean of the standard deviation of the 4 background values.

The procedure was carried out for 3 different ROIs respectively with high - medium - low contrast according to the canons given in the TOR 18FG instruction manual [78], in fact discs 1 - 5 - 9 were examined respectively with contrast 0.167 - 0.088 - 0.045 (see 4.1.1).

With this method, the SDNR of images from 40 kV to 150 kV was analysed to see how this parameter varies at different voltages.

Figures 13-17 show an example of the methods of analysis used on the image at 40 kV. First (*Figure 13*) a ROI inside the disc was selected, then 4 different area of background *(Figures 14-17)* were chosen in order to calculate the average intensity and standard deviation and lastly the SDNR.

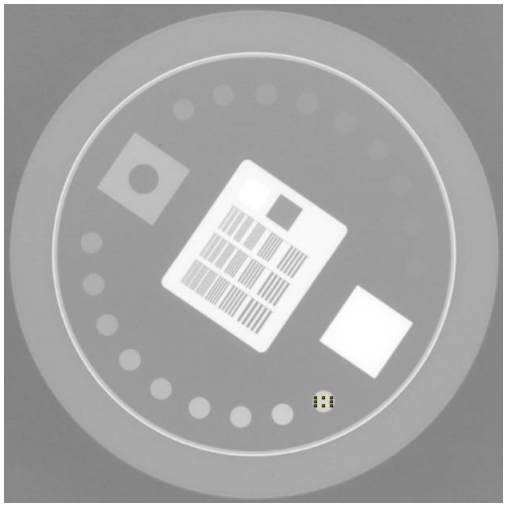

Figure 13. Selection of the ROI in disc 1.

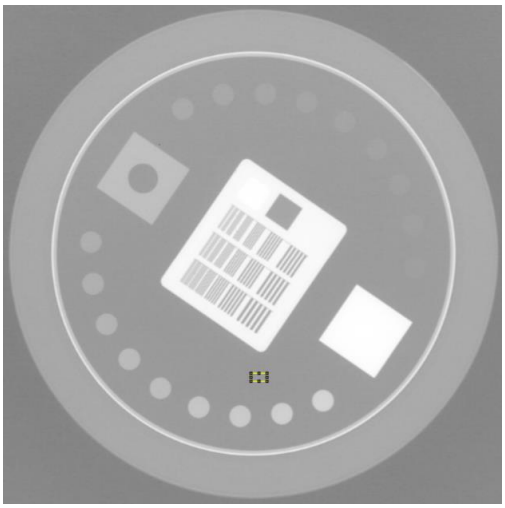

Figure 14. Selection of the ROI in the left Background.

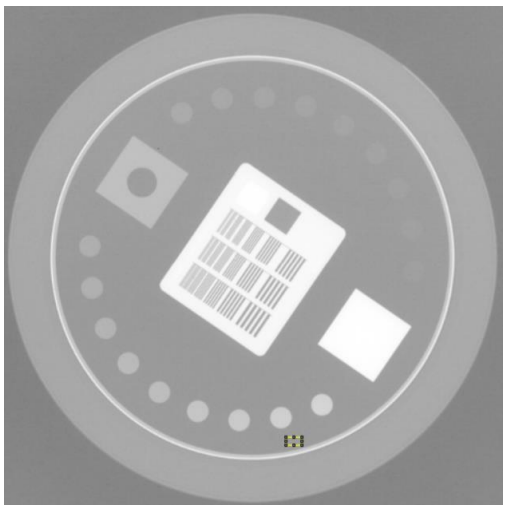

Figure 15. Selection of the ROI in the down Background.

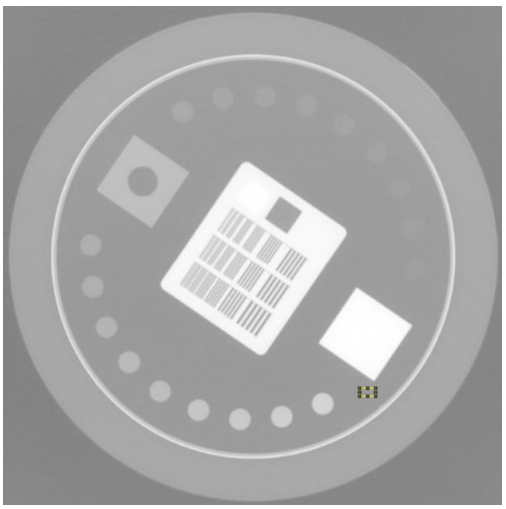

Figure 16. Selection of the ROI in the right Background.

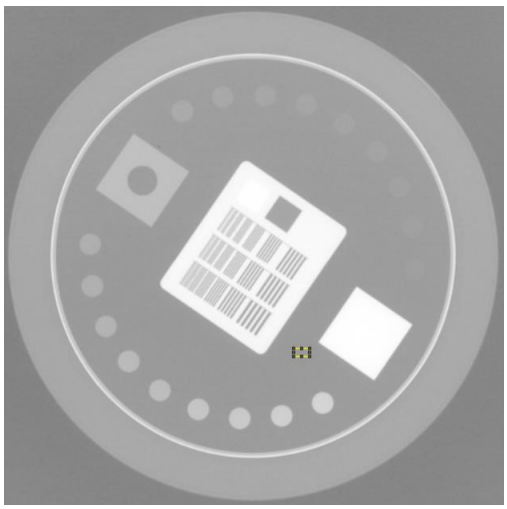

Figure 17. Selection of the ROI in the upper Background.

4.2 Materials and Methods – Study II: Experimental Acquisition of CBCT Spectra

In this second study the following main topics will be described:

- CdTe Detector for acquiring the spectra;
- Calibration of the detector with radionuclides;
- Acquisition and methods of analysis of the spectra.

4.2.1 Experimental Setup

4.2.1.1 CdTe Detector

In this work an AMPTEK XR-100T-CdTe [83] detector was used for the spectra measurement *(Figure 18)*. When a photon or particle passes through the detector, it interacts with the CdTe material, generating electrons and electron gaps within the crystal lattice [84]. These electron charges are then collected and measured to determine the energy and amount of incident radiation.

This digital processor includes: a multichannel analyser, all required power supply, close-loop temperature regulation, and the detector bias voltage. Data collection occurred at 240 K with 801 V bias. The ADMCA.EXE program that comes with Amptek's digital processors ware used to collect the data [85]. The collimator kit EXVC.0 was included with the CdTe detector equipment.

The detector is built with a 100 mm beryllium window that is vacuum-tight and the CdTe crystal of 3x3x1 mm^3 volume [83]. A tiny Peltier (thermoelectric) device [86] is used to cool the crystal, which lowers leakage current and enhances the crystal's charge transport capabilities. With the aid of X-rays from the radioactive calibration sources, the spectrometer system's energy calibration was completed with ^{241}Am, ^{152}Eu (*Figure 19*).

During the X-ray tube spectra measurements, different geometries setups were performed: changing distance from 100 cm and 40 cm, modifying current and tube voltages and adding Tungsten collimator kit EXVC.0 with aperture of 400 and 1000 μm.

All the final measurement were performed with a low tube current of 20 mA, and spectra at 60-80-100 kV were acquired.

Figure 18. XR-100T-CdTe Gamma Ray and X-Ray Detector shown with Amptek PX5 Digital Pulse Processor.

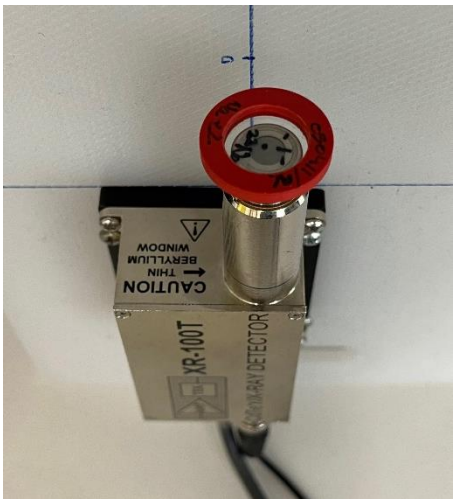

Figure 19. XR-100T-CdTe Gamma Ray and X-Ray Detector with ^{241}Am Radionuclides on top.

To acquire, visualize and process the signal, the DPPMCA (Digital Pulse Processing Multi-Channel Analyser) was used. This software for Windows was developed by Amptek for visualizing the spectra [83]. It is designed to facilitate data acquisition, visualization, and control for Amptek signal processors used in X-ray and gamma-ray spectroscopy.

This software gives you complete control of all hardware functions, such as acquisition presets, gain, peaking time, detector HV, detector temperature, number of channels, rise time discrimination parameters, and more.

The main features used in the work are spectral visualization in different scale, linear and logarithmic vertical scale, manual or automatic interval, and zoom in on the horizontal; pulse processing for filtering the signal; features of energy calibration to find peaks [85].

4.2.1.2 Radionuclides for Detector Calibration

In order to accurately identify the photon energy, the detector needs to be calibrated. Energy calibration can be performed using monochromatic radiation sources of known photon energy,

such as a synchrotron X-ray source [87], radioisotopes [88], [89] or X-ray fluorescent materials [90], [91].

For the calibration of the detector 2 radionuclides sources (*see Table 7*) were used because they present energy emission in the same range of our CBCT spectra [88].

The Centro de Ciências e Tecnologias Nucleares - IST Lisbon, PT provides various radionuclides: ^{241}Am,^{109}Cd, ^{54}Mn, ^{166m}Ho, ^{57}Co, ^{152}Eu and ^{22}Na, *Figure 20*.

Table 7. The average activity and half-life of the radioisotope sources highlighted (*) the two chosen for the study [92].

Nuclide	Activity (mCi)	Half-life (day)
^{241}Am*	9.95*	158007.2*
^{109}Cd	1.83	461.4
^{54}Mn	0.76	312.33
^{166m}Ho	1.02	$438*10^3$
^{57}Co	0.57	271.8
^{152}Eu*	0.37*	1.68×10^{21}*
^{22}Na	4.66	950.8

The energies analysed range from 40 keV to 120 keV, so radionuclides whose spectrum had more peaks in this range were chosen.
The literature recommends using ^{241}Am, which has a significant peak at 59.24 keV, and Cobalt [93], however for this study ^{241}Am and ^{152}Eu was chosen [94] because ^{57}Co was not available (*Figure 21*).

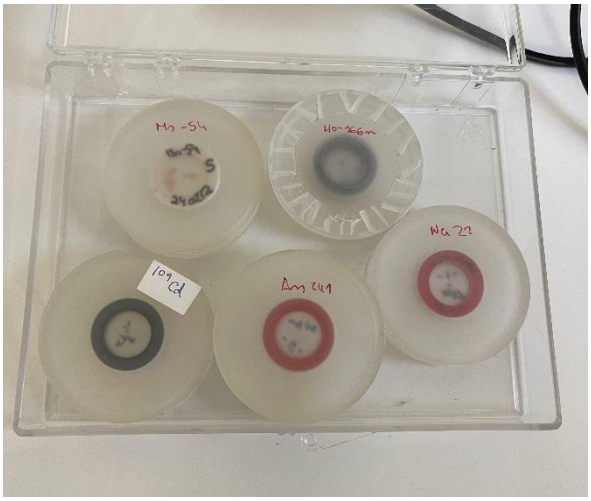

Figure 20. Radionuclides provided by the Campus Tecnologico e Nuclear in Bobadela - IST Lisbon, PT.

Figure 21. XR-100T-CdTe Gamma Ray and X-Ray Detector with ^{241}Am & ^{152}Eu Radionuclides on top.

4.2.1.3 Spectra Acquisition

All measurements were performed with the Varian Clinac DHX linear accelerator, equipped with the Cone Beam for On-Board-Imager from Varian Medical Systems [79], in Clínica de Radioncologia de Santarém, Portugal, used for radiotherapy and X-ray imaging.

The OBI (On-Board-Imager) system allows for precise imaging treatment for radiotherapy. It is mounted orthogonally to the MV beamline and consists of a kV tube and an amorphous silicon detector, which can be calibrated to variable imaging conditions [80].

Reading the OBI construction and implementation private manual [95] with the radiology technician, it turned out that there are two filters on the exit window of the X-ray tube: the first one is “0.7-0.9” mm aluminium equivalent (0.8 mm was taken as reference), the second one is 2 mm aluminium. Overall, there is a 2.8 mm aluminium equivalent filter.

Acquisitions of spectra started by placing the detector on the patient table at various distances from the X-ray source. In order to optimize spectra acquisition, the distance source-detector was changed, from 100 cm to 40 cm.

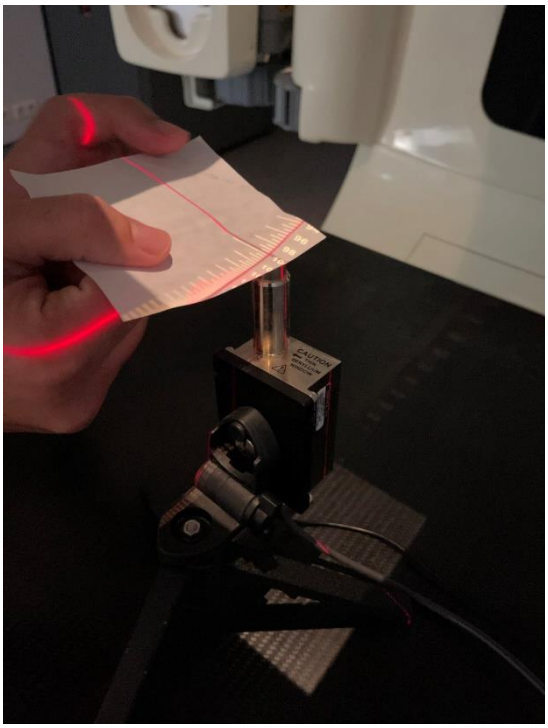

Figure 22. Alignment of the detector without collimators with the x-ray source tube.

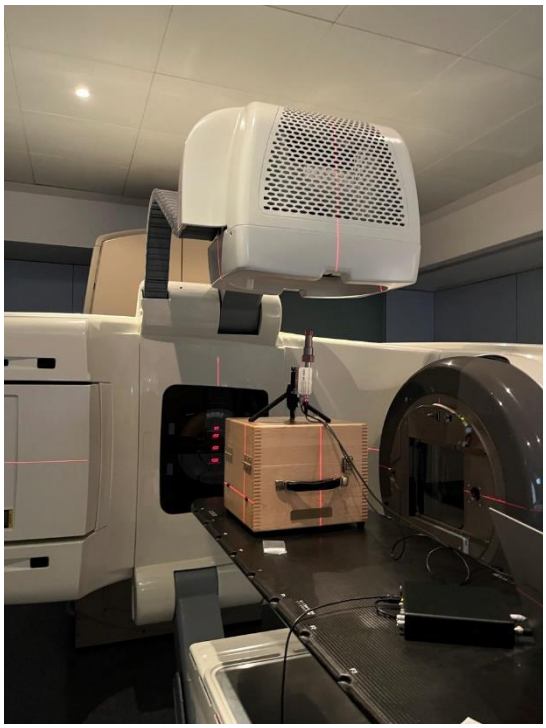

Figure 23. CBCT aligned with the detector equipped with the Tungsten collimator at 40 cm.

The system CBCT - detector - signal processor was prepared as in the Figure 23 and through the software the detector was properly connected to the DPPMCA.EXE data acquisition system.

The detector was aligned to the X-ray tube with a laser system, as reported in *Figure 22.*

Several spectra were acquired changing different parameters:

- voltage: the voltages varied from 40 kV to 120 kV in steps of 20 kV. This was to analyse the whole range of energies of interest. In fact, from the previous work were realized that below 50 kV and above 120 kV the SDNR dramatically;
- time: the X-ray beams were irradiated with different exposure times. Indicatively from 10 seconds to 2 minutes. depending on the kV setting.
- Collimators: AMPTEK XR-100T-CdTe detector include some collimator kit. The measurements of clinical spectra could present some difficulties due to the limited irradiation parameters changing and for not correct X-ray beam-detector alignment, so often spectra measurements could present some distortion. In these cases, the use of

tungsten collimators could be useful to solve these issues [96] 400 µm - 1000 µm hole and 2 mm thickness collimators were used for measurements, since an improvement in terms of pile-up decrease was registered;

- source-detector distance: Initially started from the common 100 cm, however then it was observed that the number of counts detected by the detector was low and slowly increasing so it was preferred to decrease the distance to speed up the acquisition at 40 cm;

- gain: the DPPMCA software has the feature to vary the acquisition gain, which is the amplification of the output signal relative to the input signal. It is a scaling factor that allows to increase the amplitude of the signal to make it easier to measure or to adapt it to the specifications of a system or device. In our case measurements were made with various gains, however for the final measurements a gain of 3x was chosen, and the same gain was chosen for calibration (paragraph 4.1.2);

- current: the current in the various measurements was kept constant, with a value of 20 mA. This current value seemed to have a correct balance between output amplitude and background noise. By varying these characteristics were acquired many spectra which were analysed and compared with the literature.

The literature spectra were taken from the healthcare siemens website [97], where X-ray beams can be reconstructed adding also appropriate filters.

4.2.2 Methods of Analysis

4.2.2.1 Detector Calibration

To commute the channel to the energy scale it's necessary to take some energy references and calculate the calibration curve [98]. As references ^{241}Am and ^{152}Eu radionuclides were used.

These two materials were chosen because they have peaks at energies suitable for this work in the diagnostic energy range.

The two radionuclides were placed on the top of the detector and the spectra were acquired.

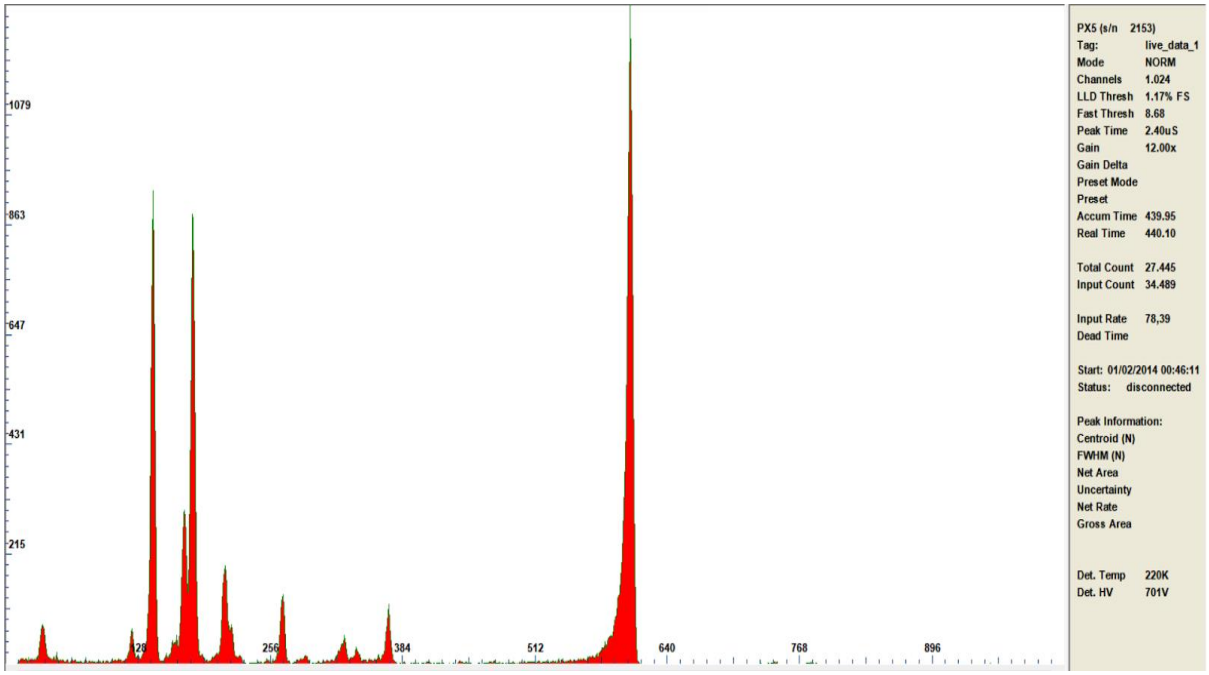

Figure 24. Spectrum of the ^{241}Am, linear scale, gain 12x.

Figure 24 shows the acquired spectrum of ^{241}Am in linear scale. A set up with 1024 channels, 12x gain was used. In the x-axis there are the number of channels while on the y-axis the number of counts. The software for 12x gain already has an initial filtering of 3% of the spectrum to avoid noise at low energies.

Through Matlab were found the peaks and compared them with the literature [93].

The same procedure was repeated with ^{152}Eu [94].

The spectra show that some peaks of two elements are very close, so rather than use them all to calculate the calibration line it's decided to look at the spectrum of the two elements at the same time, seeing which of the peaks had greater importance and "strength" and eliminate the others.

With the separated spectra, 4 peaks in ^{241}Am and 6 in ^{152}Eu were chosen.

With the combined spectra, 6 peaks for the calibration were chosen, *Figure 25*.

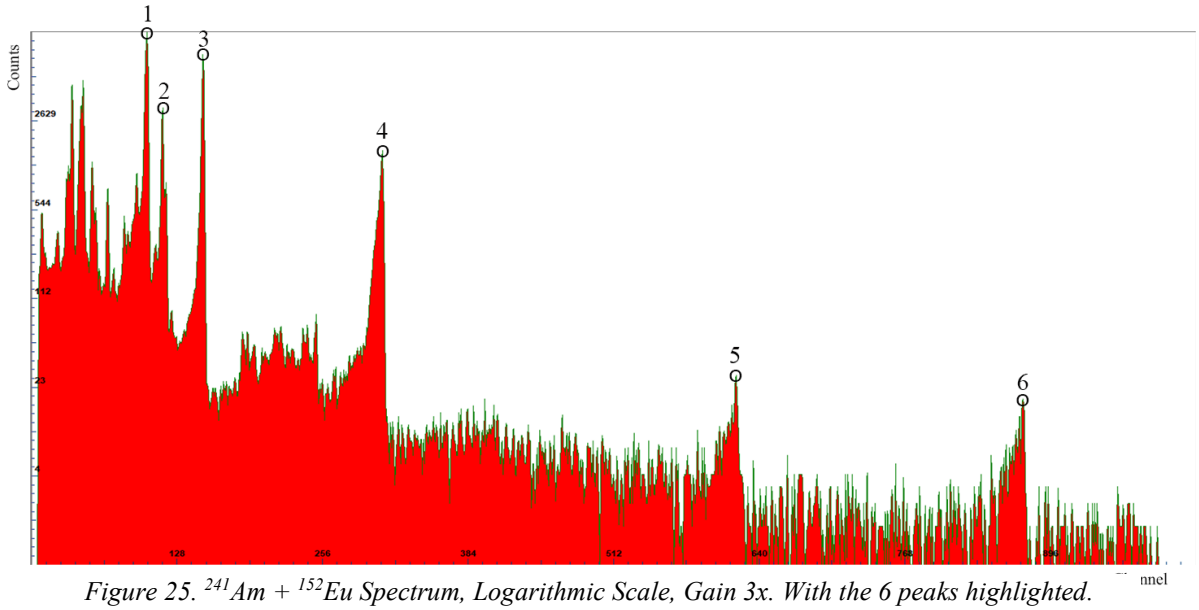

Figure 25. ^{241}Am + ^{152}Eu Spectrum, Logarithmic Scale, Gain 3x. With the 6 peaks highlighted.

The linear fitting method (performed with Origin program [99]) was used to find the calibration line, this process finds the best line that fits the available data [100].

Linear regression is a statistical method used to model the relationship between a dependent variable (Y) and one or more independent variables (X). The goal of linear regression is to find the best regression line that represents the relationship between the variables based on the available data [101].

The method used that is commonly used to estimate regression coefficients is the least squares method. This method seeks to minimize the sum of squares of the errors between the observed values of Y and the values estimated from the regression line.

Then the linear fitting, gave us in output the straight line that best approximates the relation among energy and channels. The equation of the linear fit is:

$$y = mx + q \ ; \qquad \textit{(Eq. 12 [102])}$$

Where:

- y represents the dependent variable (response variable).
- x represents the independent variable (predictor variable).
- m represents the angular coefficient, which represents the slope of the line.
- q represents the intercept, which represents the point at which the line intersects the Y axis.

4.2.2.2 Experimental Spectra Analysis

First, the calibration line was used to find the relation channel-energy.

Second, although the software was already doing filtering at low energies, the signal was filtered by cutting to the point where there is a lot of background noise at low energies.

However, in order to have a smoother curve in the low energy region to a gaussian interpolation was performed (*Figures 26-27*).

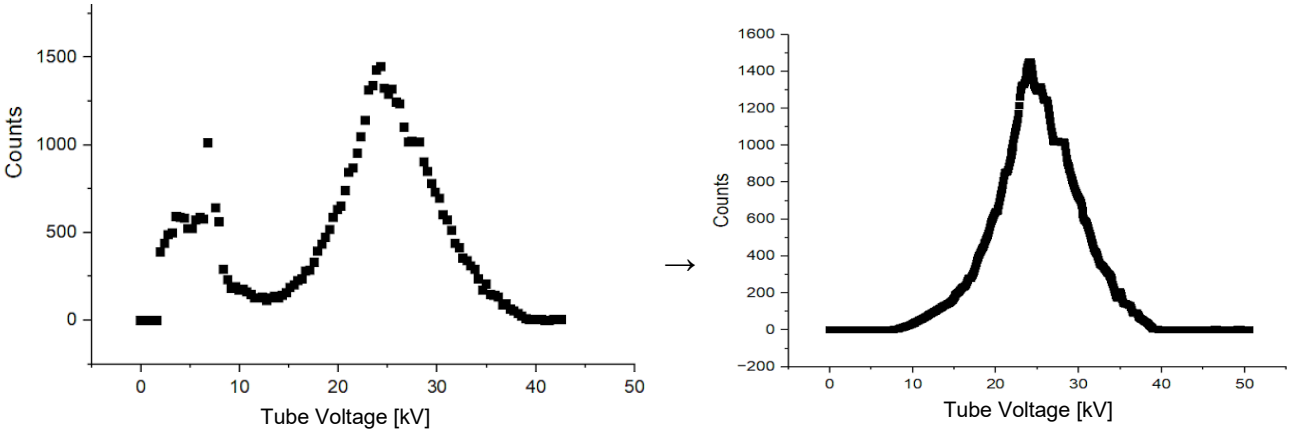

Figure 26. Raw Spectrum at 40kV.

Figure 27. Filtered and post processed Spectrum at 40 kV.

Interpolation refers to the process of estimating or approximating an intermediate value between two known points in the graph [101]. The goal is to estimate a value within the range of available data, based on the trend of the known points.

There are several interpolation methods that can be used to approximate intermediate values in the graph [100].

Since the graph in the cut-off part must follow a Gaussian curve, we cannot perform linear interpolation, but must rely on polynomial or spline interpolation.

Origin uses various interpolation methods. The two most efficient for our purposes are the B-Spline and Akima Spline. In fact, the Akima is a specific spline interpolation method that aims to provide a better approximation of curves with discontinuities or noisy data points. This type of interpolation calculates the coefficients of the interpolation polynomials so that the derivatives are estimated more accurately, especially at discontinuity points [101].

Once the graphs were reconstructed, were compared with those in the literature. As comparison metrics peaks, maxima, minima, trend and average energy were analysed.

Peaks, maxima and minima, were analysed by observing at the various energies the value of the counts. Then the graphs were superimposed to note whether the trend was the same or how it differed.

The average energy, on the other hand, is a value considered important because it is an average estimate of the penetration depth of photons. This value is useful for understanding the energy distribution of the detected particles or radiation sources. To calculate the average energy of the spectrum, it is necessary to multiply each energy bin value by its respective count bin, then sum all the values obtained. This total energy fluence is divided by the total number of counts in the spectrum. The average energy can be expressed as:

$$Mean\ Energy = \frac{\sum(En * Counts)}{\sum Counts}; \qquad \textit{(Eq.12 [103])}$$

Finally, results found were analysed and discussed.

4.3 Materials and Methods – Study III: Dose assessment in pediatric CBCT

In this last study the following main points will be illustrated:

- Monte Carlo simulations via PENELOPE software to measure the energy deposited in the organs of two pediatric phantoms;
- Dose evaluation and analysis of three CBCT protocols.

4.3.1 Monte Carlo simulations

The Monte Carlo algorithm [104] is a numerical method that is used to find solutions to mathematical problems, which may have many variables and cannot be solved analytically. Starting from a modelling of the processes under investigation and the generation of random variables, simulations consisting of multiple runs are performed to derive an approximation of the probability of certain results. The method has assumed great importance in many areas of science and engineering, especially for its ability to deal with complex problems that previously could only be solved by deterministic simplifications; it is mainly used in three distinct classes of problems [105]: optimisation, numerical integration, and the generation of probability functions. The Monte Carlo method has an extremely simple approach: it solves macroscopic systems by simulating their microscopic interactions [106].

In physics applications, the Monte Carlo method is very useful for simulating systems with several degrees of freedom, such as fluids and cell structure. This method is widely used in the field of particle physics and high-energy physics [107]; in recent years, it has also become very interesting for application in the field of medical physics, e.g., for X-ray diagnostics, radiotherapy, dosimetry, radiation protection, modelling of ionising radiation detectors, and imaging in nuclear medicine. Compared to other methods, the efficiency of Monte Carlo increases as the problem size grows.

Monte Carlo code must follow to develop the simulation, they include [105]:

- Geometry modelling: here, the geometric components, materials and cross-sections that come into play in the interaction processes are defined. It is important to observe the distances, thicknesses, shapes and composition of the materials associated with the various components, sticking as closely as possible to reality. When constructing the

geometric model, it is reasonable and necessary to make approximations, but that affect the output as standard deviation [108].

- ➢ The definition of the type and energy: associated with the particles of the beam to be simulated.

- ➢ The generation of the particles: there are algorithms that allow the particles to be simulated taking all their properties into account.

- ➢ The transport of the particles: from the point or volume of origin, they must diffuse and interact until they lose most of their available energy, there are then functions that make cuts by interrupting the simulation of events with energy below a certain threshold, whose interactions would no longer produce energy loss or events capable of interacting again, which would be useful for the result but would only lengthen the computation time.

- ➢ Scoring in volumes of specific interest: a certain result is obtained as an integration of the value recorded in each voxel in which space is sampled. There are specific functions that allow the user to decide how to sample and how to extract the results.

In the case of calculating the absorbed dose by a patient from exposure to a radiation beam, once the history of each individual particle is known, the sum of the energies deposited by all the particles making up the entire beam is taken as an estimate of the absorbed dose. The standard deviation σ, whose value typically decreases as:

$$\sigma \propto \frac{1}{\sqrt{N}}; \qquad \textit{(Eq. 11 [47])}$$

The precision of the calculation method grows as the number N of particles processed during the simulation increases; to obtain a sufficiently precise estimate of the deposited energy, it is typically necessary to follow the history of a number of photons of the order of $10^6 \div 10^8$: a large number of places serious limits on the efficiency of the Monte Carlo method [108]. In every simulation performed in this study the number of histories was between $2*10^8$-$5*10^8$.

4.3.2 Penelope & PenEasy

The mostly used MC programmes in physical fields are PENELOPE [109], Electron Gamma Shower [110], Monte Carlo N-Particle, Geant4 and FLUKA.

PENELOPE, used in this work, is a MC simulation software, freely available on Linux or Windows operating system, widely used in the field of radiation physics. It is designed to simulate the interaction of X-rays, gamma rays and electrons with matter, allowing users to study a variety of phenomena, such as photon propagation, energy deposition, secondary electron production and more [109].

PENELOPE's main features include [109]:

- ➢ Interaction with matter: PENELOPE offers a wide range of interaction models to simulate photon absorption, Compton scattering, the photoelectric effect and the production of electron-positron pairs. It can accurately calculate the energy deposition and tracking of individual electrons.

- ➢ Complex geometries: PENELOPE supports the definition of complex three-dimensional geometries, allowing users to model realistic environments and objects of interest. This is useful for simulating photon propagation and scattering effects in heterogeneous materials.

- ➢ Detector response: The software enables the simulation of the response of radiation detectors, such as scintillation detectors or semiconductor detectors, allowing users to study detection efficiency, energy resolution and other detector properties.

- ➢ Data preparation and analysis: PENELOPE offers tools for x-ray and gamma-ray generation with specific energy distributions. In addition, it allows analysis of the data produced by the simulation, including energy spectra, dose maps and electron distributions.

PenEasy [111] is the general-purpose main programme for PENELOPE used for this study's simulations. It provides users with a set of starting models, calculations and variance reduction techniques that are invoked by a structured code. Users are asked to enter, via plain text files, the information required to set up the simulation. Geometry description and associated material properties are introduced via the usual PENELOPE geometry and material data files.

PenEasy's code is mostly written in Fortran 95, although it makes use of some features of the Fortran 2003 standard. Like PENELOPE, it is a free and open-source software.

The PenEasy input file is composed by 5 important main section that recall all important PENELOPE files (see an example in *Appendix I*) [111] :

1) In the first one "SECTION CONFIG", we enter the configuration settings, such as the simulation stop conditions. For example, the simulation will be halted when any of the following conditions is fulfilled:

➢ The requested number of histories has been reached.
➢ The allotted time has been exhausted. The time is interpreted as real (i.e., clock) time if it is a positive real number and as CPU (user) time otherwise.
➢ The relative uncertainty requested of all the active tallies have been reached.

2) Then in the second section "SECTION SOURCE" devoted to the source of the beam to simulate, where the details of the CBCT beam were indicated: amplitude, distance and position from the source, and inserted the file describing the spectrum of the x-ray beam.

3) The third section "SECTION PENGEOM+PENVOX" concerns the geometry models and in fact the Pengeom.geo file is called up, as well as the file where the voxel phantom of children aged 10 and 15 are programmed.
   Three possible geometry models are possible with penEasy, namely: quadric geometries, voxelized geometries and a mixture of quadrics and voxels. In this work a voxelized geometry was used.

4) The fourth section "TRANSPORT PARAMETERS" is dedicated to the transport parameters used for each material, so a recap is made of all those we can find with the identification number of each.
   The section contains a table with one material per row. Each row begins with the material's index (MAT#), which must be a sequential integer number starting with 1. A maximum of 20 characters may be entered for the material's file name, and blank spaces or special characters are not permitted. The line then contains useful material values that we can set such as the maximum and minimum value of Absorbed Energy for charged particles and photons, EABS. The value of two constants C1 and C2,

selected by the user [111], which determine the calculation time required for the simulation of each track. Ideally, they should have no influence on the accuracy of the simulation results. This is only the case when their values are sufficiently small.

5) The last part “TALLIES” it talks about tally. Tallys are important because they refer to the quantities or quantities that are calculated and recorded during a Monte Carlo simulation. They are essential for obtaining detailed information on the results of the simulation.

   When running a simulation with Penelope, the interaction events of particles with matter are tracked and the contributions to the tally are accumulated progressively [111]. Tallys can be specified in the input file to record various quantities, such as deposited energy, absorbed dose, particle trajectory, particle angular distribution and so on. After the simulation, tally results are written to the output file, allowing the user to analyse them and use them to assess radiation effects, optimise radiation protection or make comparisons with experimental data.

In this study the Tally 'Energy Deposition', which measures the amount of energy deposited in a chosen material in the input phase, was used.

An example of an input file with a dedicated explanation can be found in *Appendix I*.

4.3.3 Pediatric Phantoms

The earliest computational phantoms were known as “stylised”, or mathematical, phantoms, in which the contours of body and organs were described by mathematical equations [112]. Those phantoms offered flexibility for modification but were not anatomically realistic.

The International Commission on Radiological Protection (ICRP) [113] is an independent, international organisation concerned with protection from ionising radiation. It was founded in 1928 and its main objective is to provide evidence-based guidelines and recommendations for radiation protection for both people and the environment.

The ICRP introduced reference adult male and female voxel phantoms in ICRP Publication 110 [114]. But the interesting publication is the 143 [115], where it publishes pediatric phantoms of 0-1-5-10-15-year-old males and females, *Figure 28*.

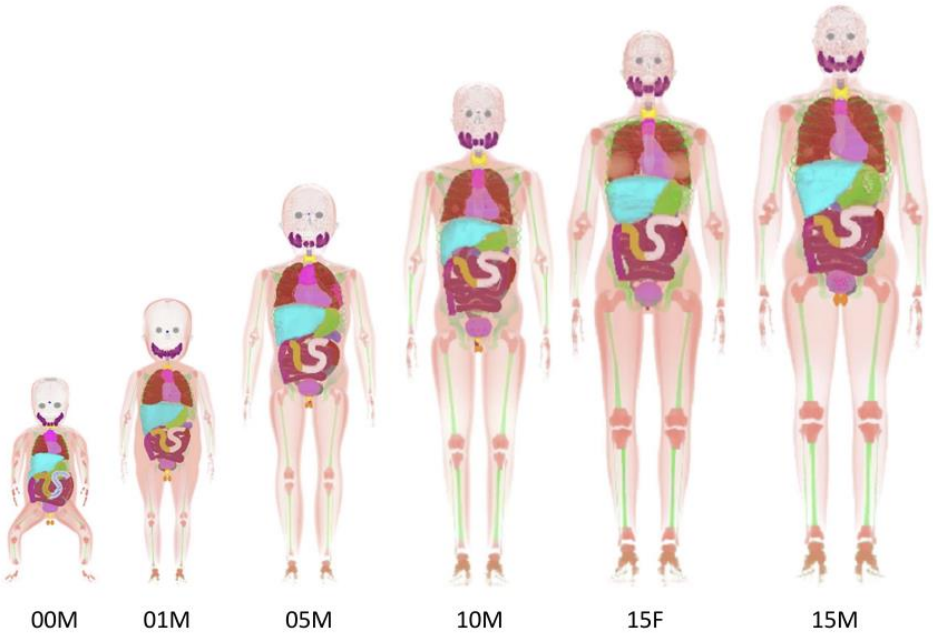

Figure 28. Frontal views of the ICRP pediatric phantom series representing newborn male (00M), 1 year old male (01M), 5-year-old male (05M), 10-year-old male (10M), and 15-year-old female (15F) and male (15M) reference individuals.

The reference pediatric phantoms, like the adult phantoms, were built using precise modifications to medical imaging data of real people. However, the digital data were used to model the organs and tissues using mesh surfaces, capturing and adding as much fine detail as possible, based on anatomical knowledge. To maintain a lot of this detail, the data were voxelised at a very high resolution while taking the age-dependent total skin thickness into account [115].

The pediatric reference computational phantoms in this publication [116] mark an important shift from purely voxel-based phantoms to a hybrid format developed using anatomical data from medical scans and knowledge of fine anatomical structures, resulting in voxel phantoms of arbitrarily high resolution.

In this study Monte Carlo Simulations were performed with computational phantoms and the energy deposited in the different organs was evaluated.

The computational phantom was built following the PENELOPE manual where it is explained how to create voxelised structured and by entering data from ICRP 143 that contains all the specifications of pediatric bodies.

The phantoms used for the simulations were the 10F and 15F, the number indicates the age and the letter 'F', the gender, Female.

In annex I are reported some of the characteristics of the two phantoms used.

4.3.4 Phantom's Methods of Analysis

The computational models made available for this study were 15F (15-year-old female and 10F (10-year-old female).

The OBI manual shows that according to the area of the body to be analysed different protocols are used, these are the ones used for all types of patients, from adults to children indifferently by gender, height or weight [9].

There are 3 protocols: Thorax, Head & Neck, Pelvic and are directly integrated into the CBCT equipment.

In imaging are used different protocols depending on the body zone because you can vary the energy and the size of the area of interest. For example, in the " Head & Neck " protocol the area of interest will be slightly smaller to avoid exposing unnecessary parts of the body to radiation, while for example in the Pelvic protocol a higher energy is used since there are many bones and thick, which have a high density and therefore a higher X-rays absorption [66].

The table below includes the various specifications for each type of protocol [9], [66].

Table 8. CBCT Modes OBI 1.4 1.5 1.6 [9].

Protocol | Feature	THORAX	HEAD & NECK	PELVIC
2D Images Blades [cm]	X1=13.7; X2=10.0 Y1=7.1; Y2=10.7	X1=13.4; X2=13.4 Y1=10.0; Y2=10.0	X1=13.4; X2=13.3 Y1=10.0; Y2=10.0
3D Images Blades [cm]	X1=13.7; X2=10.0 Y1=7.1; Y2=10.7	X1=13.4; X2=13.4 Y1=10.0; Y2=10.0	X1=13.4; X2=13.3 Y1=10.0; Y2=10.0
X-Ray Voltage [kVp]	110	100	125
X-Ray Current [mA]	20	20	80
X-Ray Milliseconds [mS]	20	20	13
Gantry Rotation [deg]	360	200	360
Number of Projections	655	360	655
Exposure Time [mAs]	262	145	680

During standard clinical image acquisition, blades with rectangular shape as collimators to focus the beam on the target, are typically used. In this work a circular blade was used.

It is important to remark that in this study there was not a complete modelling of the CBCT X-ray source, and all the blades and collimators system was not taken into account. This type of modelling is quite complex, and it was beyond the scope of this work. Here, the different protocols mean mainly the use of different voltages and the choice of different isocenter according to the clinical task (i.e., thorax, head and pelvic). Depending on the phantom and protocol, several MC setups were considered [115]:

- *Phantom 10F*

  - Thorax protocol: the center of the lungs, which is 107.19 cm in height and 20.30 cm laterally.
  - Head & Neck protocol: the center of the Cranium located at 131.31 cm in height and at 20.69 cm laterally.
  - Pelvic protocol: the center of the Pelvis located at 73.60 cm in height and at 20.89 cm laterally.

- *Phantom 15F*

  - Thorax protocol: the center of the lungs, which is 125.00 cm in height and 24.42 cm laterally.
  - Head & Neck protocol: the center of the Cranium located at 152.85 cm in height and at 23.94 cm laterally.
  - Pelvic protocol: the center of the Pelvis located at 88.09 cm in height and at 24.00 cm laterally.

These protocols were used with X-ray beams at different voltages: 40 kV, 50 kV, 60 kV, 70 kV, 80 kV, 90 kV, 100 kV, 110 kV, 120 kV. Regarding the spectra, the literature ones were used for MC simulations [97].

The organs investigated were selected based on the body part scanned. In the "Head & Neck" protocol scans, organs that were “too far" were not evaluated as they were not very evaluable and had a very high-level statistical uncertainty. However, potentially radiosensitiveorgans were kept in the analysis, for example, in the Head & Neck the spleen was not evaluated, but the uterus was.

The table below shows the organs analysed according to the type of protocol:

Table 9. Organs evaluated in this work per protocol.

	THORAX	HEAD &NECK	PELVIC
Bladder	☒	☐	☒
Brain	☒	☒	☒
Breast	☒	☒	☒
Eyes	☒	☒	☐
Heart Wall	☒	☒	☒
Kidney	☐	☒	☒
Left Colon Cont	☐	☐	☒
Liver	☒	☐	☒
Lung	☒	☒	☒
Oesophagus	☒	☒	☐
Ovaries	☒	☒	☒
Pancreas	☒	☐	☒
Right Colon Cont	☐	☐	☒
S intestine Cont	☐	☐	☒
S intestine Wall	☐	☐	☒
Spleen	☒	☐	☒
Stomach Count	☒	☐	☒
Stomach Wall	☒	☐	☒
Thyroid	☒	☒	☐
Uterus	☒	☐	☒

4.3.5 Dose Analysis

Once the X-ray beam was adjusted, the size and position confirmed and the script created,Monte Carlo simulations for each protocol were performed.

The PenEasy software output gives us the deposited energy per photon [eV/hist]. The deposited energy is a measure of the kinetic energy transferred to the particles of the material during interaction with the radiation.

Knowing the energy deposited, then to obtain the absorbed dose it is necessary to divide for the organ mass: (section 2.2.1) [42].

$$D\ [Gy]\ = \frac{E\ [eV] * \ 1{,}602 * 10^{-19}\ \left[\frac{J}{eV}\right]}{m\ [kg]}\ ; \qquad \textit{(Eq. 14 [42])}$$

This is the Absorbed Dose per number of histories (in this case photons). If a current and a time exposure is defined it's possible to assess the absolute Absorbed dose per every scan in every organ, however this work is focused on the relative Absorbed Dose variation among one protocol to another.

4.3.5.1 Data Validation.

Before running all the MC simulations for organ dose calculations, there is the need to understand if the results are acceptable or not, namely it is necessary to have a MC model that give reasonable results. For this reason, a comparison study with literature model [116] was performed.

After replicating the same setup as in the study [116], a cuboid of air was positioned in front of the 15F phantom and the air kerma (section 2.2.1) through it was calculated with MC simulations. The cuboid had a size x= 18 cm; y= 0.3 cm; and z= 18 cm.

Finally, the value of the dose coefficient for all organs was found by dividing the Absorbed Dose by the AirKerma:

$$Dose\ coefficient\ \left[\frac{Gy}{Gy}\right] = \frac{D\ [Gy]}{AirKerma\ [Gy]}; \qquad \textit{(Eq.15 [116])}$$

Because Air Kerma is a well-defined and measurable dosimetry quantity, it is used as a benchmark during calibration and normalization of measurements.

The dose coefficient values were compared with the study found where they analyse pediatric phantoms [116].

Chapter 5

Results

5.1 Results – Study I: SDNR Analysis in a TOR phantom's CBCT Images

5.1.1 Imaging

After scanning the phantom at all voltages levels, from 40 kV to 150 kV, with 10 kV steps, were obtained 12 greyscale images, saved in DICOM format with a size of 1024 x 768 pixels in 16 bits. All the scans were performed with the same current, geometry and time exposure, the only parameter that changed was the tube voltage.

The images as expected, presents a linear circumference that confirms there were no positioning errors, and it can be seen the 18 circles with different scales of intensity. The other components of the phantom were not examined because they are used for other studies such as sensitivity.

This work is focused on 3 of the 18 discs surrounding the phantom, number 1 - 5 - 9, highlighted in the *Figure 28*: High Contrast (1) - Medium Contrast (5) - Low Contrast (9).

In *Figures 29-40* results of the CBCT scans performed from 40 kV to 150 kV with the TOR 18FG are reported and to visualize them better were cropped in a square shape to remove the background.

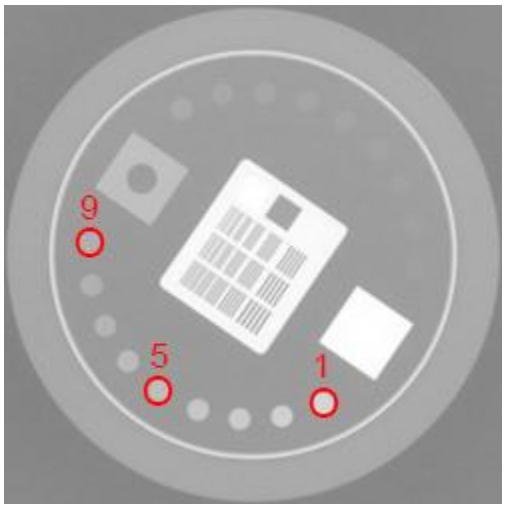

Figure 29. 2D mode CBCT scan of TOR18FG phantom at 40 kV.

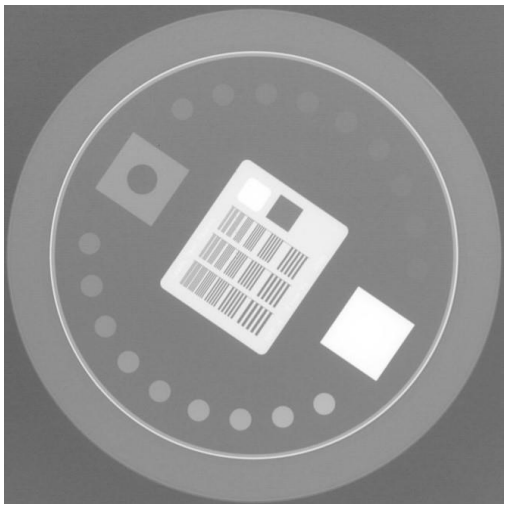

Figure 30. 2D mode CBCT scan of TOR18FG phantom at 50 kV.

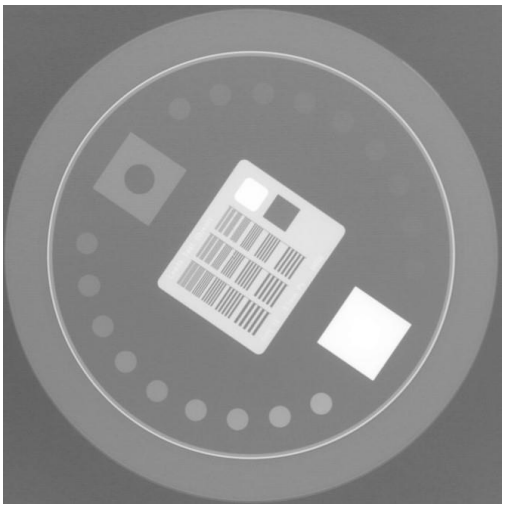

Figure 31. 2D mode CBCT scan of TOR18FG phantom at 60 kV.

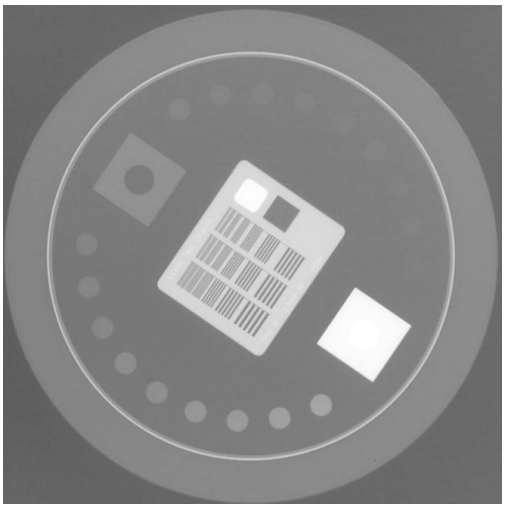

Figure 32. 2D mode CBCT scan of TOR18FG phantom at 70 kV.

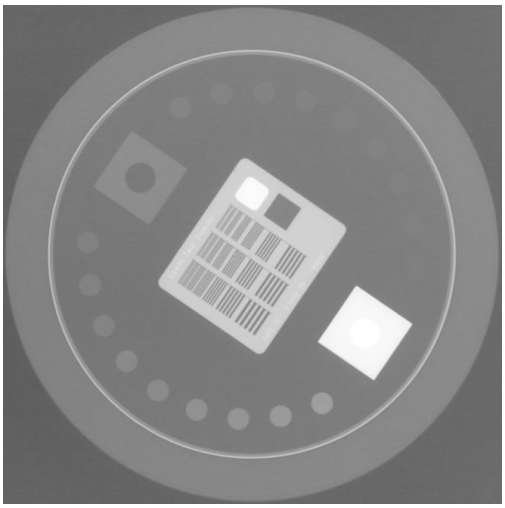

Figure 33. 2D mode CBCT scan of TOR18FG phantom at 80 kV.

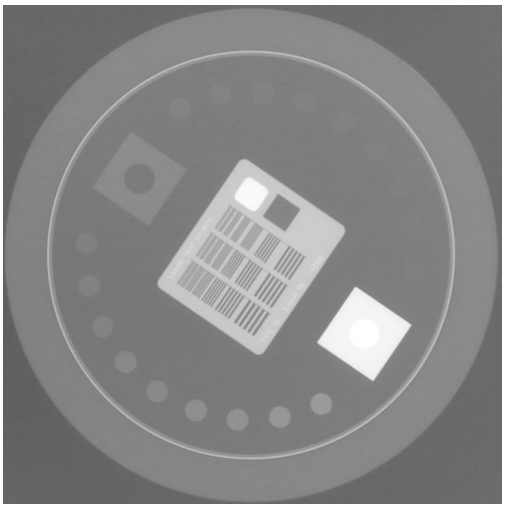

Figure 34. 2D mode CBCT scan of TOR18FG phantom at 90 kV.

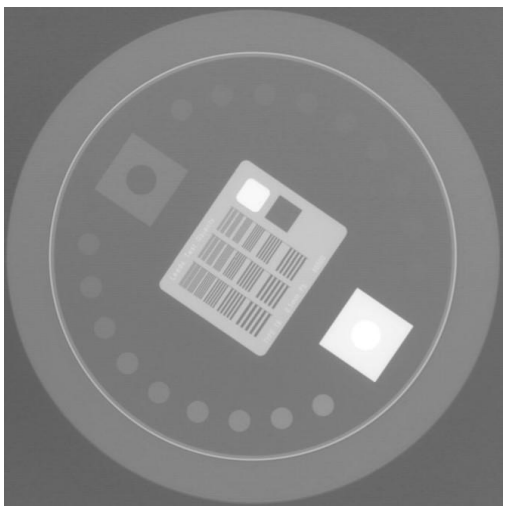

Figure 35. 2D mode CBCT scan of TOR18FG phantom at 100 kV.

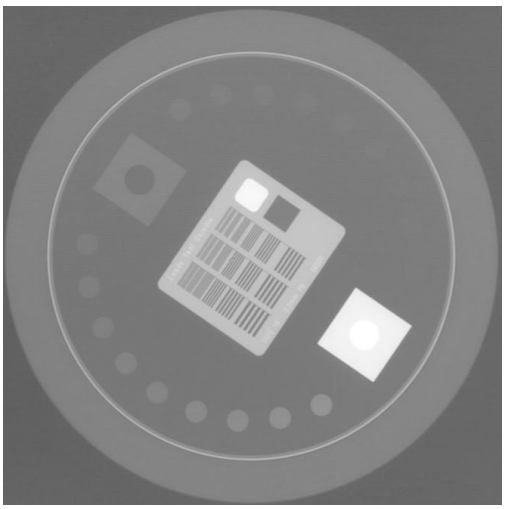

Figure 36. 2D mode CBCT scan of TOR18FG phantom at 110 kV.

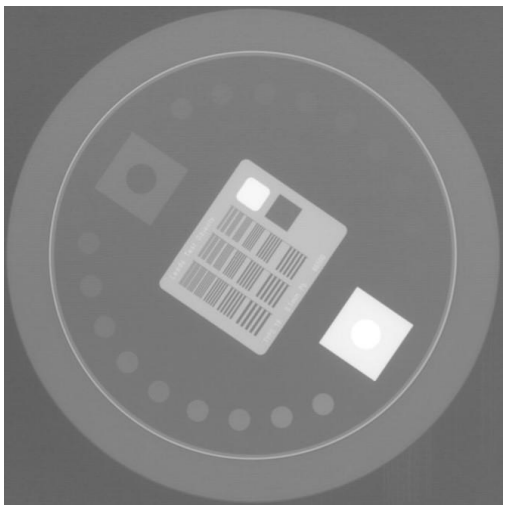

Figure 37. 2D mode CBCT scan of TOR18FG phantom at 120 kV.

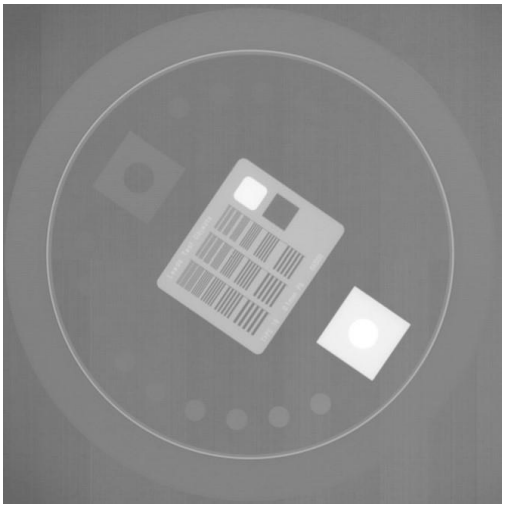

Figure 38. 2D mode CBCT scan of TOR18FG phantom at 130 kV.

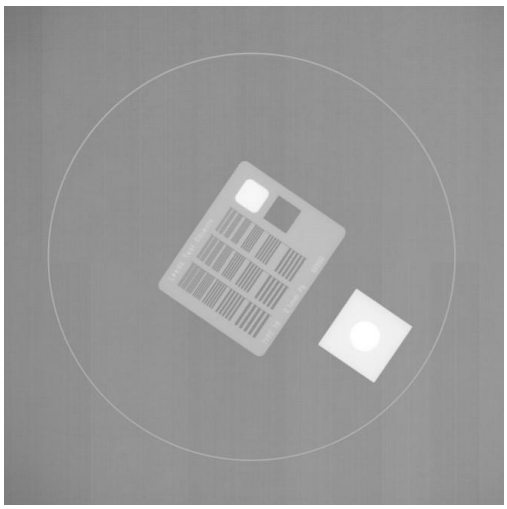

Figure 39. 2D mode CBCT scan of TOR18FG phantom at 140 kV.

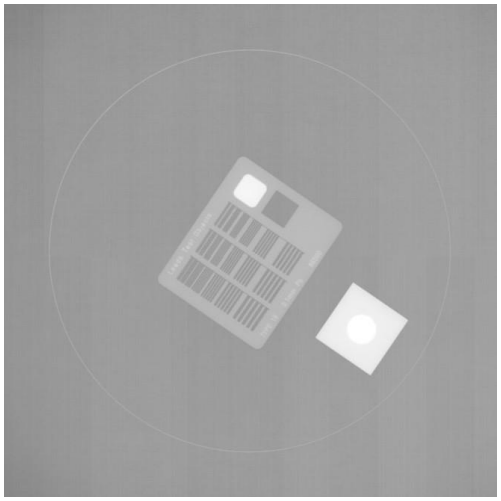

Figure 40. 2D mode CBCT scan of TOR18FG phantom at 150 kV.

5.2.2 SDNR

As explained in section 4.1.2, an area of 242 pixels was considered, both for the signal and the background regions. This process was performed for each of the 3 ROIs (discs) High-Contrast, Medium-Contrast, Low-Contrast, at various voltages from 40 kV to 150 kV in 10 kV steps.

The *Table 10* shows a summary of the SDNR at different energies for the different ROIs. Highlighted (*) the maximum SDNR values for each contrast-type are remarked.

Table 10. SDNR - ROI Comparison

Tube Voltage [kV]	High-Contrast ROI SDNR	Medium-contrast ROI SDNR	Low-contrast ROI SDNR
40	31.94	20.35	10.51
50	40.95	22.98*	11.44*
60	41.49*	22.78	10.50
70	37.82	22.23	9.72
80	36.78	21.54	8.42
90	34.75	20.39	8.16
100	34.67	19.91	7.36
110	32.47	18.83	6.99
120	31.30	18.12	6.49
130	12.38	3.61	1.49
140	1.32	1.38	0.09
150	1.32	1.38	0.09

.

Table 10 shows that the best SDNR is obtained at the voltage of 50-60 kV and slowly starts to decrease, until above 130 kV where discs in the background can no longer be distinguished. As reference for the next studies, the voltage of 60 kV is taken as the best value for the SDNR because the maximum value was obtained.

The SDNR trends for each contrast-type are shown in *Figures 41,42,43*.

- SDNR of the High-contrast ROI:

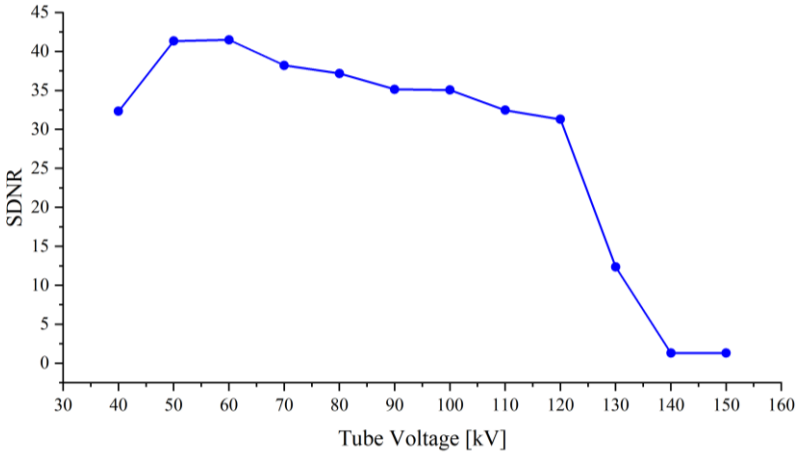

Figure 41. SDNR - High Contrast ROI.

- SDNR of the Medium-contrast ROI:

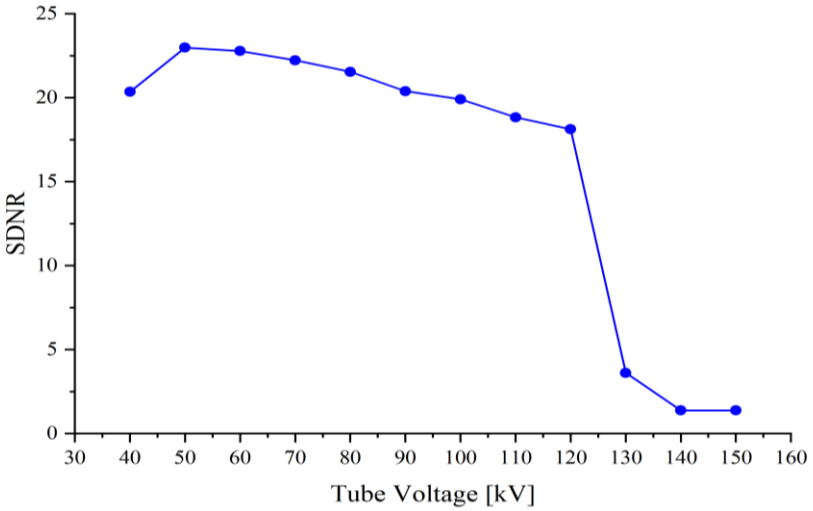

Figure 42. SDNR - Medium Contrast ROI.

- SDNR of the Low-contrast ROI

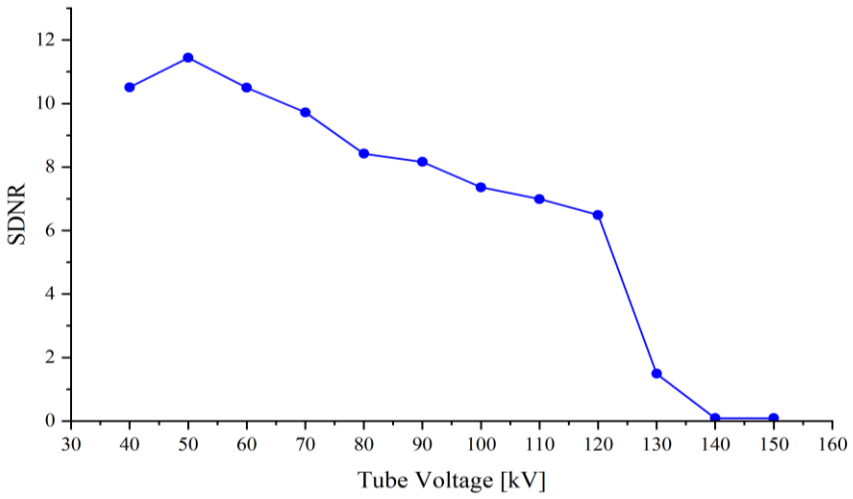

Figure 43. SDNR - Low Contrast ROI.

5.2 Results – Study II: Experimental Acquisition of CBCT Spectra

5.2.1 Calibration

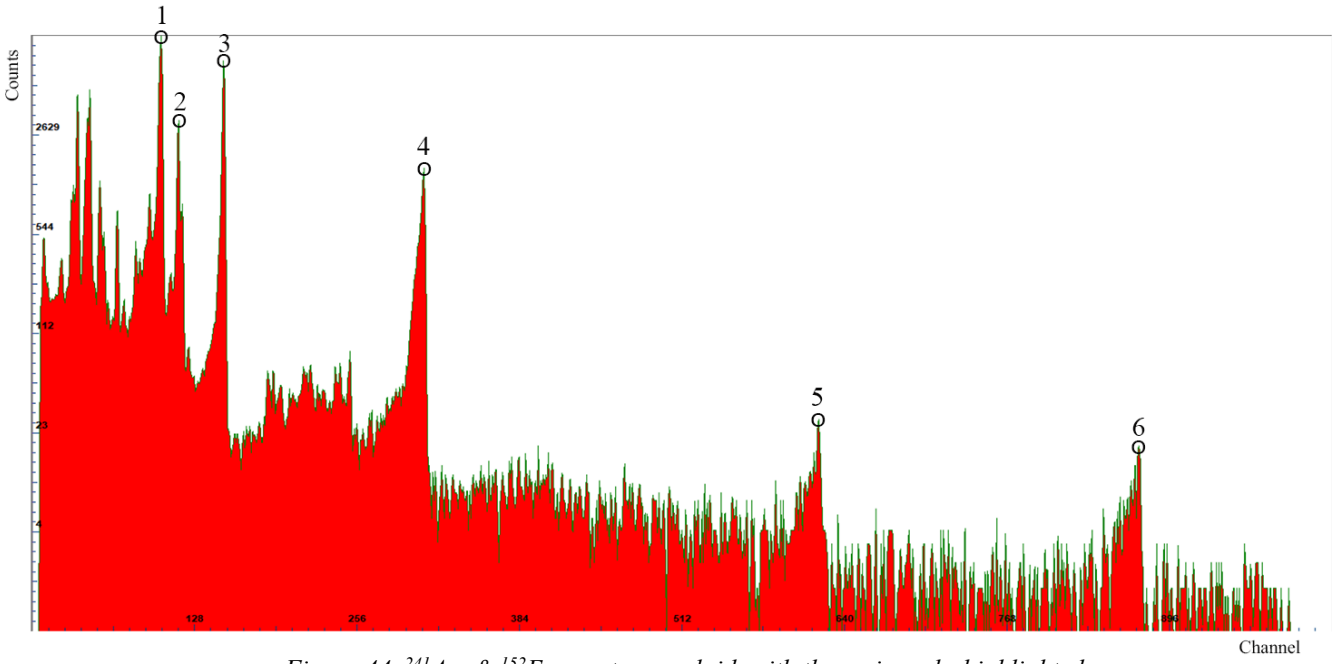

Figure 44. ^{241}Am & ^{152}Eu spectra overlaid, with the mainpeaks highlighted. For energy peak identification see Table 11.

Figure 44 shows the spectrum of ^{241}Am and ^{152}Eu overlapped in logarithmic scale. With this spectrum 6 peaks were used for calibration, namely 5 peaks from ^{152}Eu and 1 from ^{241}Am. As it can be seen there are no peaks with too low energy values because they were very close together and could also be the result of detector noise.

Table 11 presents the details of the 6 peaks chosen for the calibration of the detector, at which channel they were observed, the value of the counts and the corresponding energy value, taken from the literature.

Table 11. ^{241}Am & ^{152}Eu energy and counts peaks for calibration.

Peak number	Channel	Counts	Energy - Literature [keV]
1	101	12700	40.12
2	115	3318	45.40
3	151	8545	59.82
4	308	1572	121.78
5	619	28	244.70
6	871	18	344.28

.

To calculate the calibration curve, the data were uploaded on Origin software and a linear fitted was performed and the calibration line is reported in *Figure 45*.

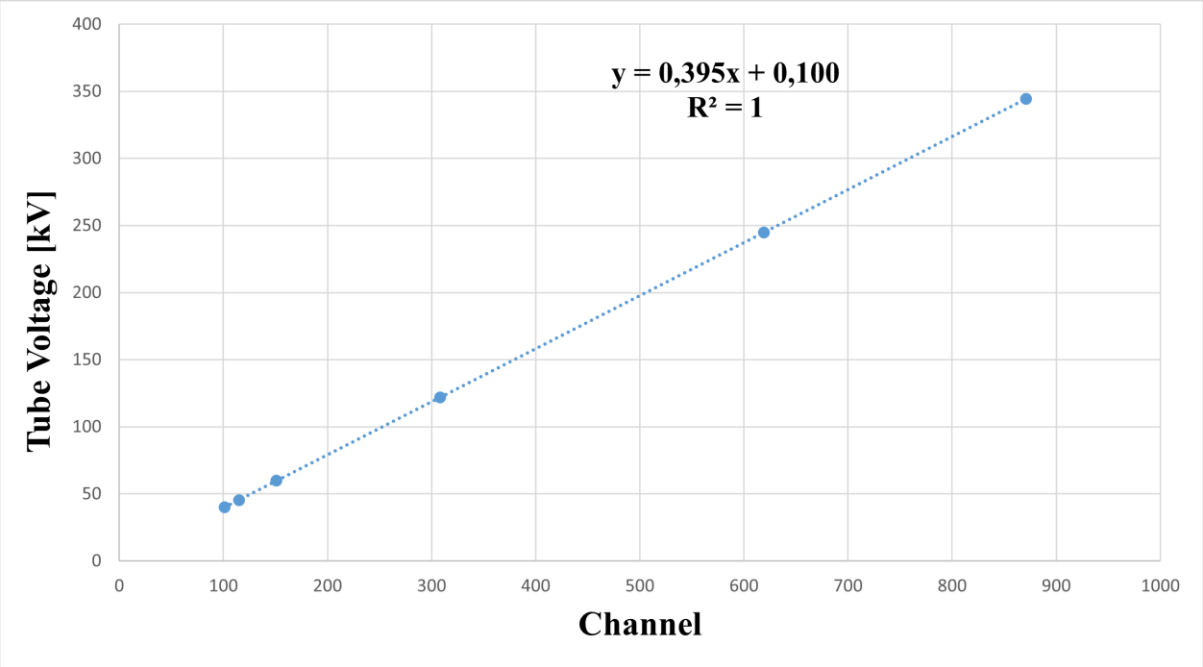

Figure 45. Calibration Line of the AMPTEK detector with 1024 channel and gain 3x, calibrated with 6 peaks of ^{241}Am & ^{152}Eu.

The calibration line found is:

$$y = 0.395 * x + 0.1 \qquad \textit{(Eq. 14)}$$

The programme evaluates the coefficient of determination R^2, namely a statistical measure that indicates how well the line fits the data. The standard error of 1,33476E-4 on the slope (0.395) and 0.06172 on the intercept (0.1), was also calculated.

At this point to definitively verify, below you can find our energy-calibrated Americium spectrum on the left, *Figure 46*, with a comparison to the literature, *Figure 47*.

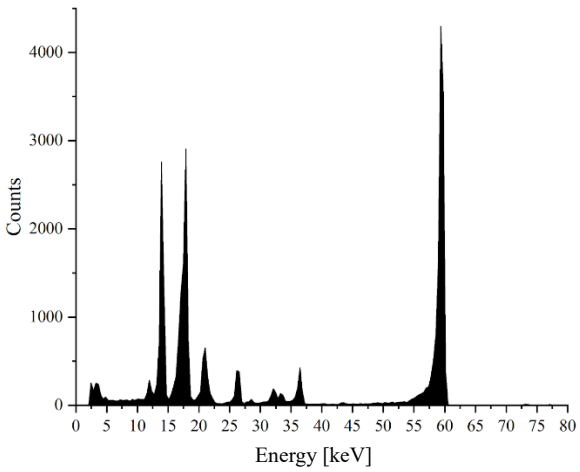

Figure 46. Am241 spectrum in linear scale acquired in this study.

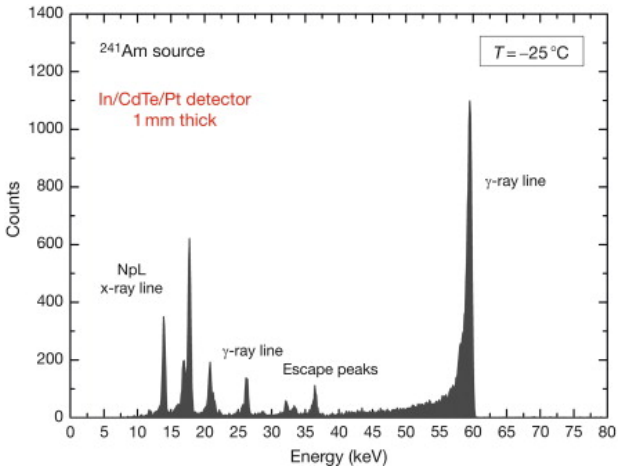

Figure 47. Am241 spectrum from literature[123].

The two spectra in *Figure 46, 47* show a good agreement, peaks are located at the same energies. Based on these results, it is possible to assumed that the calibration process is correct.

5.2.2 Experimental Spectra

The acquisitions of the CBCT spectra were made at 40 kV – 60 kV – 80 kV – 100 kV.

Also in this case, to have greater statistics, the detector was placed at 40 cm from the source and a gain of 3x was used.

Once the spectra were acquired, the initial noise was removed and were reconstructed to analyse them and compare them with those in the literature.

5.2.2.1 40 kV spectrum

Spectrum obtained at 40 kV, *Figures 48, 49*.

Exposure setup:

- Distance: 40 cm.
- Current: 20 mA;
- Gain 3x;
- Exposure: 45 seconds;
- Collimator: 400 µm.

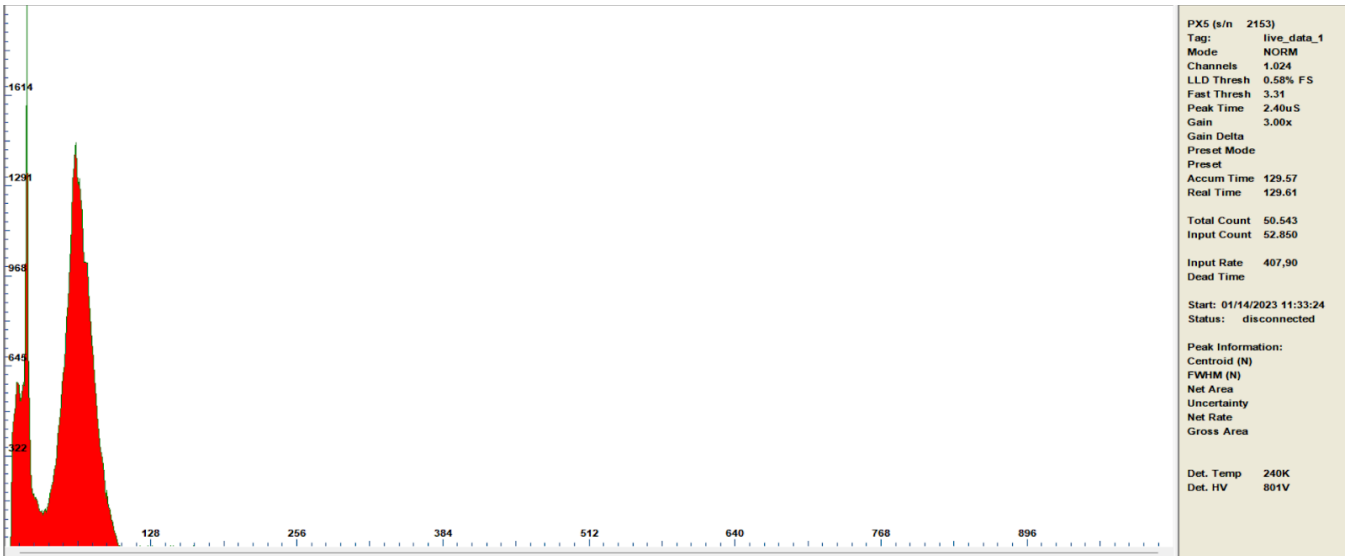

Figure 48. Raw spectrum 40 kV, linear scale, gain 3x.

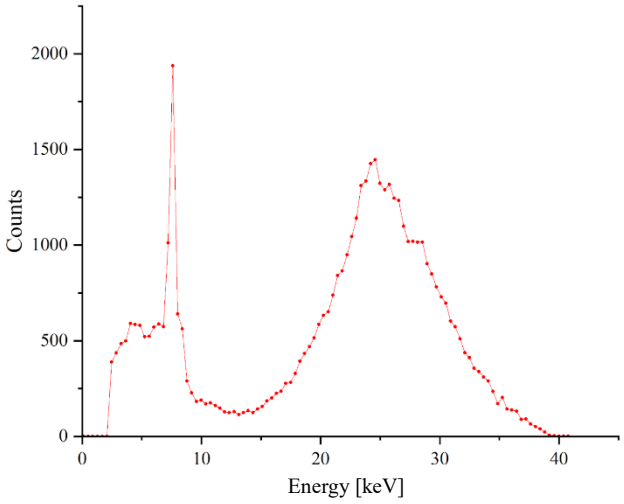

Figure 49. Calibrated raw 40 kV spectrum

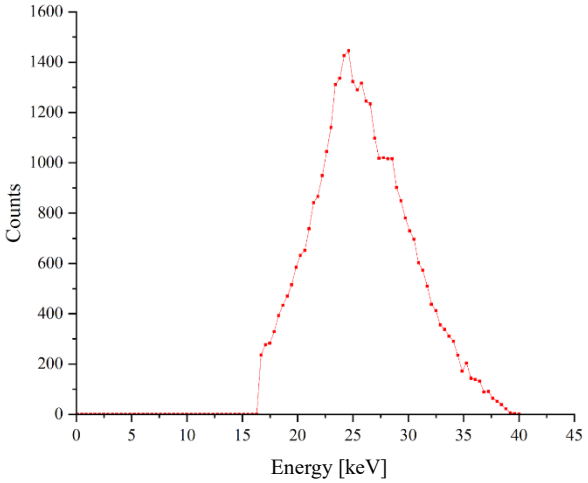

Figure 50. Porcessed and calibrated 40 kV spectrum.

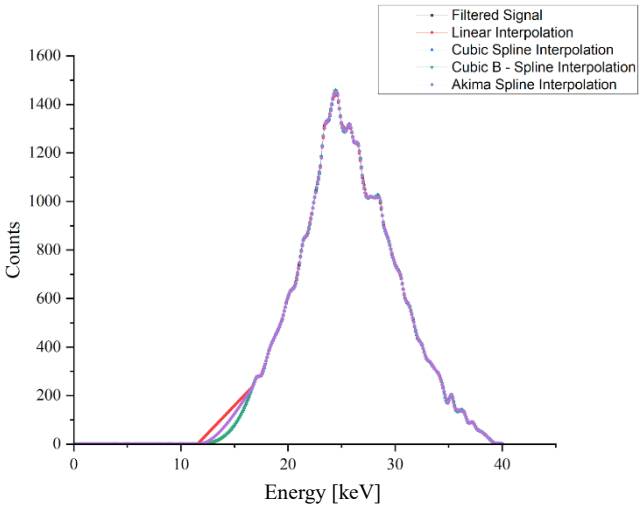

Figure 51. Interpolated 40 kV spectrum.

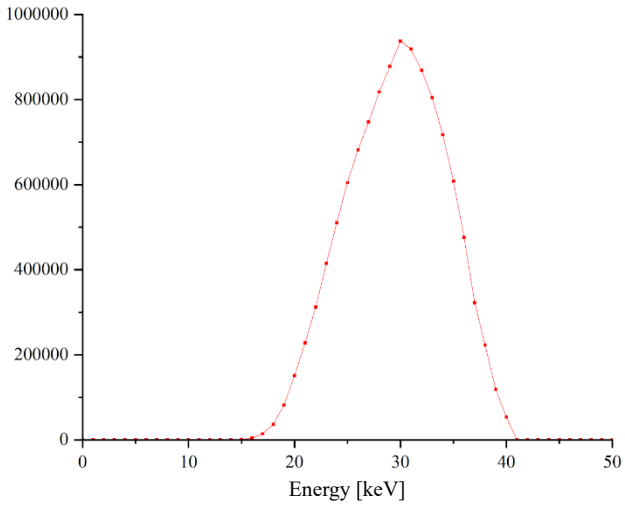

Figure 52. 40 kV spectrum from literature[97].

The images above show the post-processing process that was performed following image acquisition.

First, the spectrum was plotted on Origin software, where were observed strong initial noise (*Figure 49*). It was then filtered by cutting down to 16 keV (*Figure 50*) and interpolated in various ways in order to reconstruct the initial part of the spectrum (*Figure 51*).

The Cubic-B-Spline interpolation (in green) was chosen, and with this method an average energy of 25 keV was obtained, while from the literature the average energy should be 29.59 keV [97].

Figure 52 shows the spectrum obtained from the literature, that could be used for comparison [97].

5.2.2.2 60 kV spectrum

Spectrum obtained at 60 kV, *Figures 53, 54*.

Exposure setup:

- Distance: 40 cm.
- Current: 20 mA;
- Gain 3x;
- Exposure: 45 seconds;
- Collimator: 400 µm.

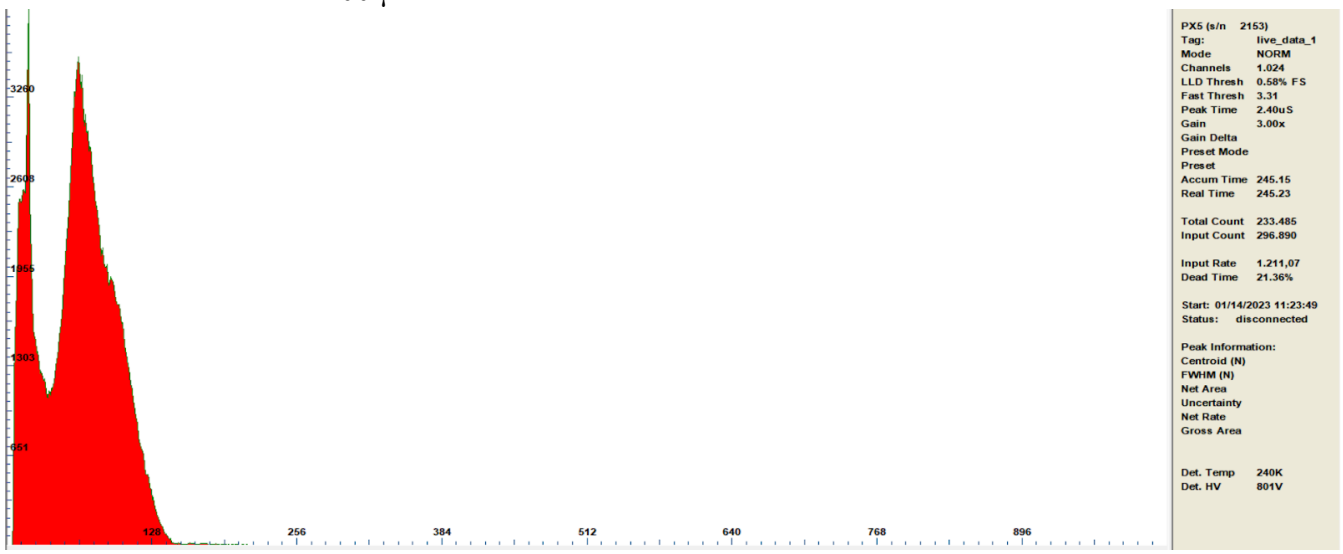

Figure 53. Raw spectrum 60 kV, linear scale, gain 3x.

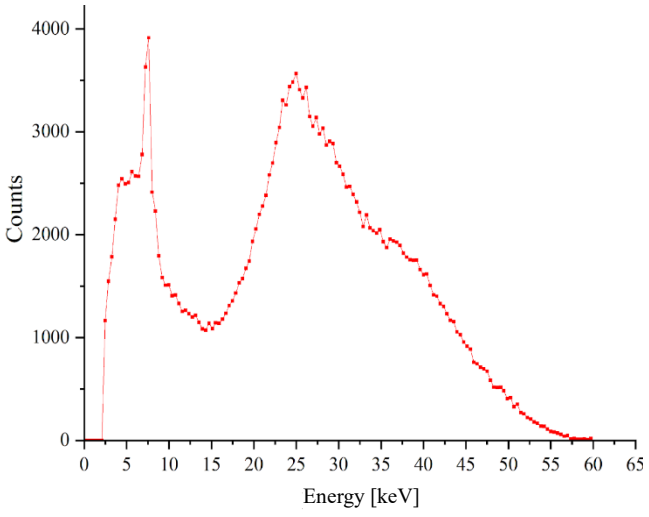

Figure 54. Calibrated raw 60 kV spectrum.

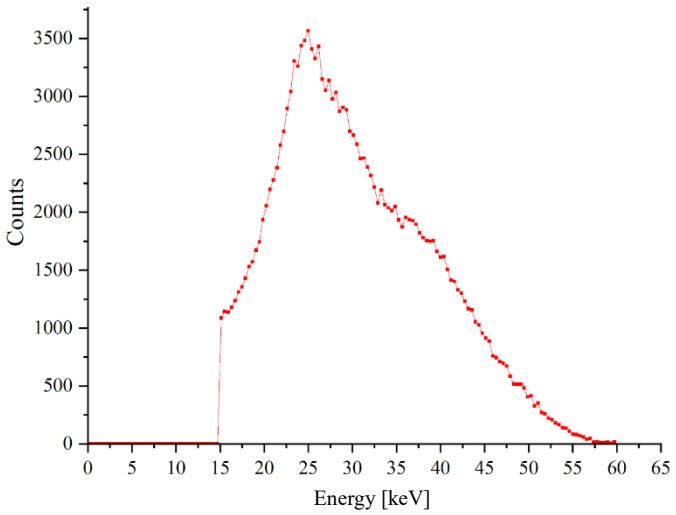

Figure 55. Processed and calibrated 60 kV spectrum.

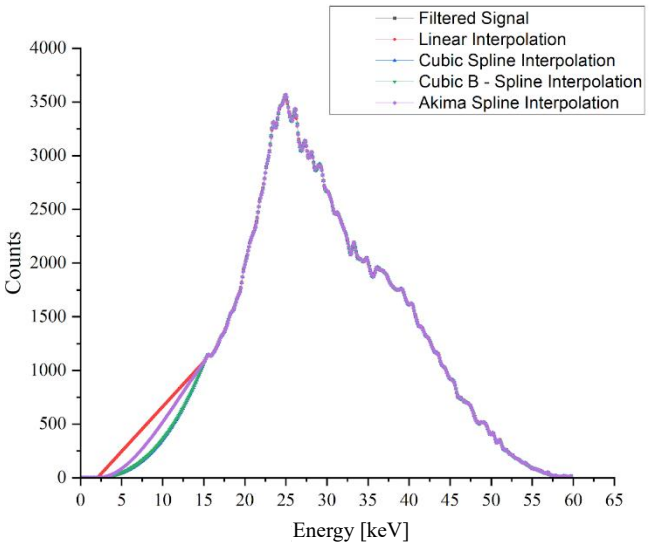

Figure 56. Interpolated 60 kV spectrum.

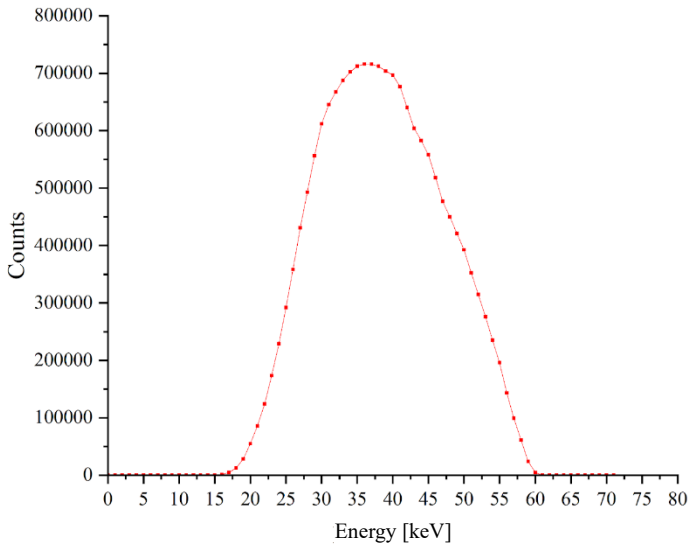

Figure 57. 60 kV spectrum from literature [97].

The *Figures 54,55,56* show the post-processing procedure that was performed following the image acquisition.

Also in this case, the Cubic-B-Spline interpolation (in green) was used. In this way the interpolated spectrum presents an average energy of 29.28 keV whereas from the literature the average energy should be 38.45 keV [97].

Figure 57 shows the spectrum obtained from the literature, that could be used for comparison [97].

5.2.2.3 80 kV spectrum

Spectrum obtained at 80 kV, *Figures 58, 59.*

Exposure setup:

- Distance: 40 cm.
- Current: 20 mA;
- Gain 3x;
- Exposure: 45 seconds;
- Collimator: 400 µm.

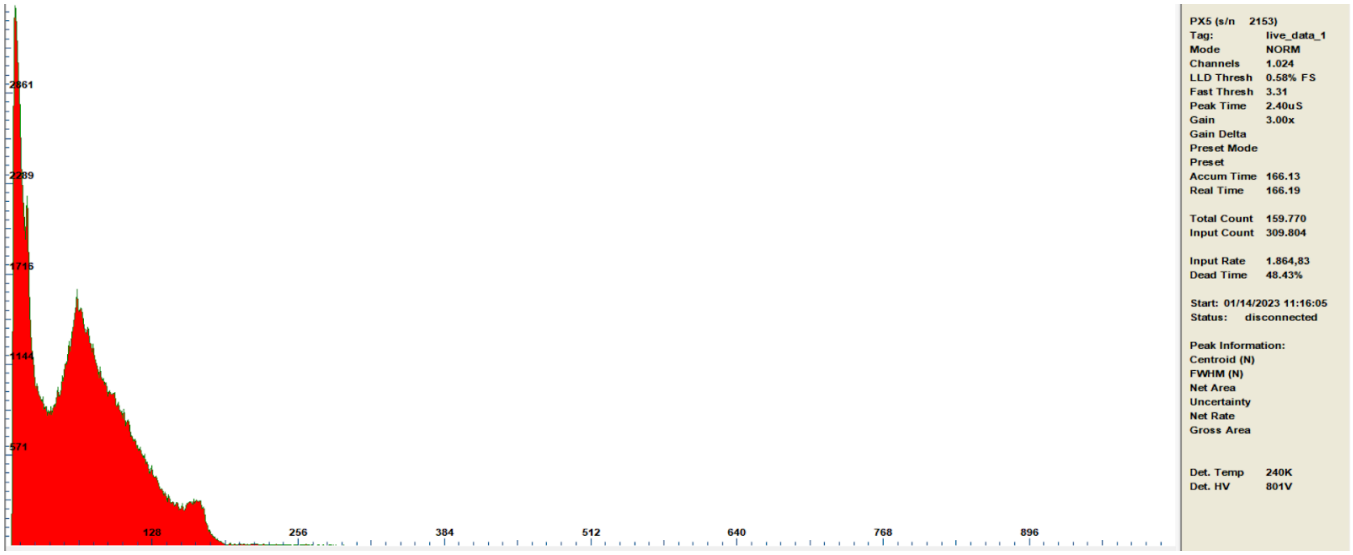

Figure 58. Raw spectrum 80 kV, linear scale, gain 3x.

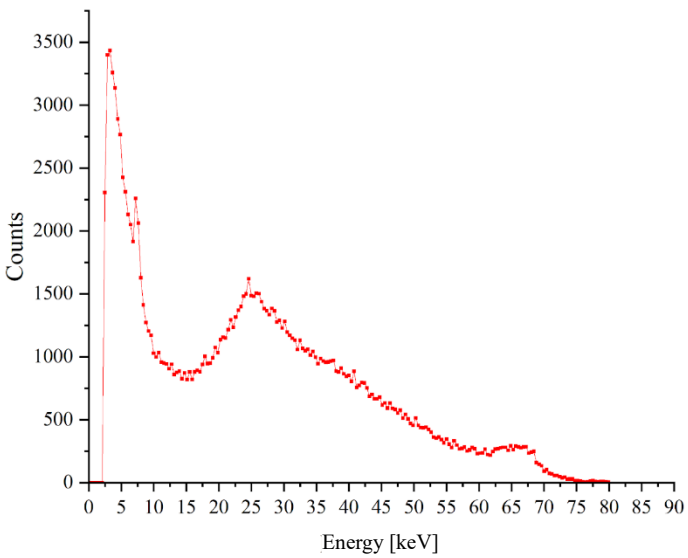

Figure 59. Calibrated raw 80 kV spectrum.

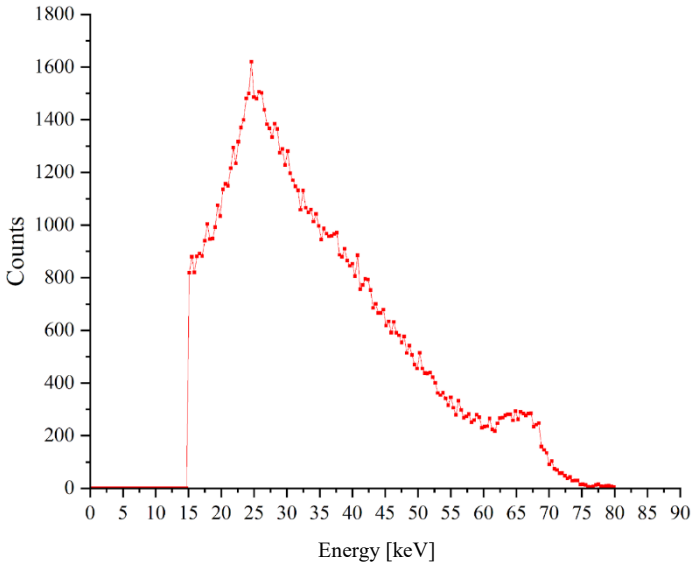

Figure 60. Processed and calibrated 80 kV spectrum.

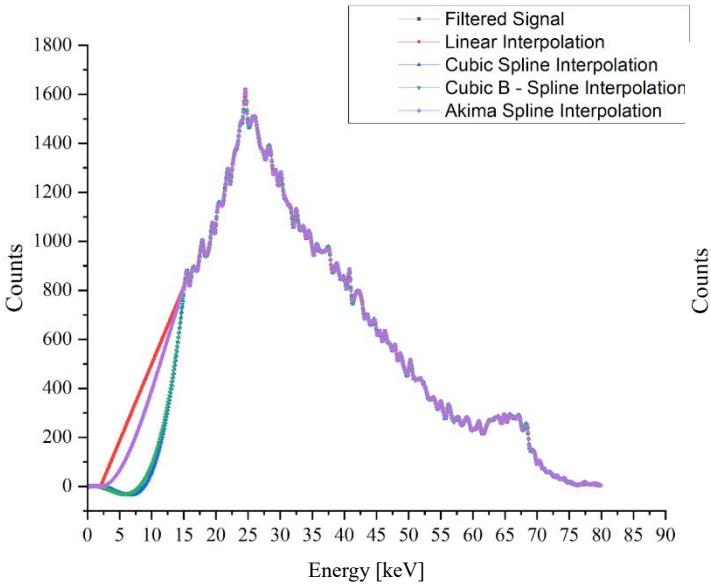

Figure 61. Interpolated 80kV spectrum.

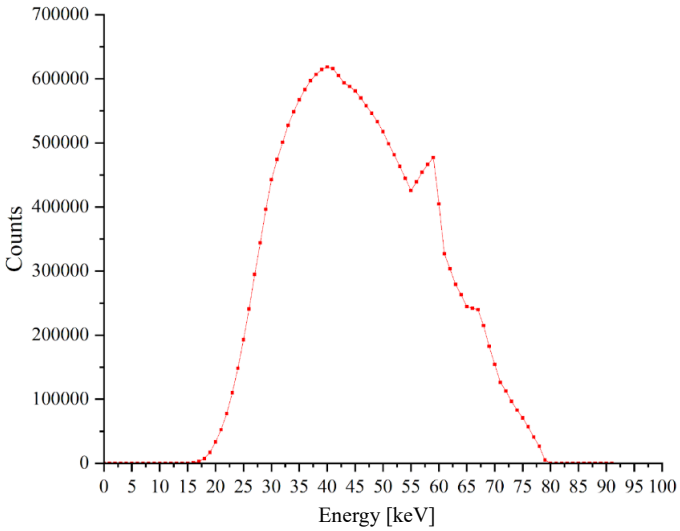

Figure 62. 80 kV spectrum from literature [97].

In this case the most suitable and accurate interpolation method was the Akima Spline interpolation (*Figure 61*, in violet). Now the interpolated spectrum presents an average energy of 34.84 keV whereas from the literature the average energy should be 45.98 keV [97].

Figure 62 shows the spectrum obtained from the literature, that could be used for comparison [97].

5.2.2.4 100 kV spectrum

Spectrum obtained at 100 kV, *Figures 63, 64*.

Exposure setup:

- Distance: 40 cm.
- Current: 20 mA;
- Gain 3x;
- Exposure: 45 seconds;
- Collimator: 400 µm.

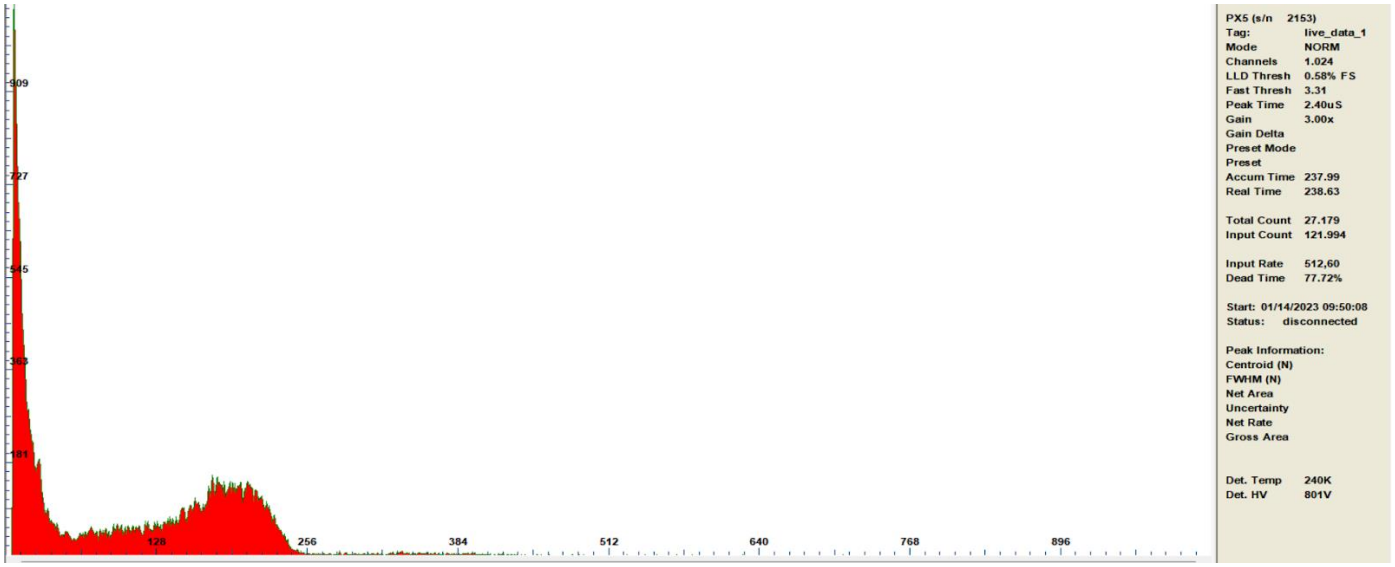

Figure 63. Raw spectrum 100 kV, linear scale, gain 3x.

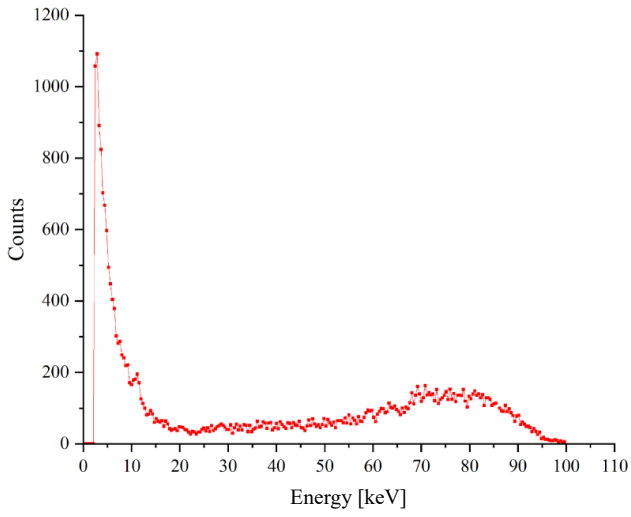

Figure 64. Calibrated raw 100 kV spectrum.

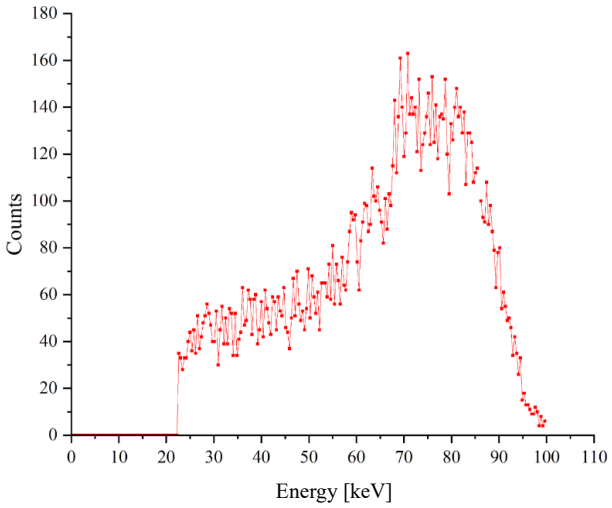

Figure 65. Porcessed and calibrated 100 kV spectrum.

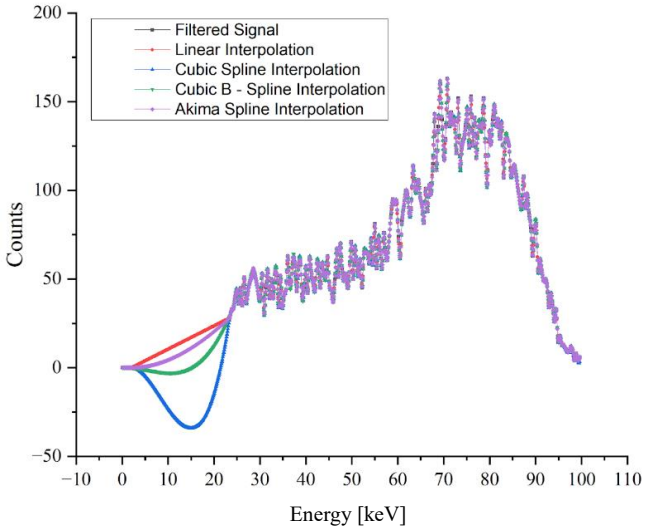

Figure 66. Interpolated 100 kV spectrum.

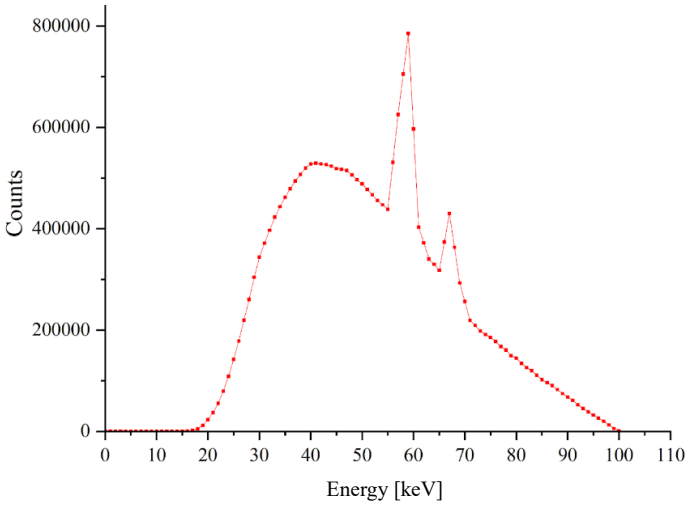

Figure 67. 100 kV spectrum from literature[97].

For the last spectrum the same analysis procedure was implemented: cut the initial noise to 23.4 keV (*Figure 65*), interpolate with an Akima Spline interpolation method (*Figure 66*) and then calculate the average energy.

In this case the spectrum presents an average energy of 63.64 keV while from the literature the average energy should be 52.09 keV [97] .

Figure 67 shows the spectrum obtained from the literature, that could be used for comparison [97].

For the sake of completeness, all the calculated average energies are reported in *Table 12* in order to show the values obtained for each kV acquisition, namely mean energy (Mean Exp. Energy), the expected value (Mean Lit. Energy) and the difference in percentage [97].

Table 12. Mean Energy & Differences

Energy [keV]	Mean Exp. Energy [keV]	Mean Lit. Energy [keV]	Difference [%]
40	25.00	29.59	-15.5%
60	29.28	38.45	-23.85
80	34.84	45.98	-24.23
100	63.64	52.09	+18.15

5.3 Results – Study III: Dose assessment in pediatric CBCT

5.3.1. Validation of the results

In order to confirm the robustness of the MC results obtained in this work, some validations of the results of this study were performed with data present in literature.

Specifically, the results were compared with the ones found in the literature by Chang et al. [116], in which they analysed the effective dose on the same pediatric phantoms to give a fixed starting point for subsequent studies.

The two studies differ in many ways, in this one the phantoms are scanned with a CBCT beam and certain imaging protocols were analysed, whereas in Chang's study mono-energetic and isotropic photon sources were simulated.

To validate our results, the definition of a dose coefficient was used. The dose coefficient represents the amount of absorbed dose per unit of activity or exposure of the source. The same geometry setup of Chang et al. [116] was reproduced.

A script simulating a mono-energy photon beam at an energy of 60 keV was created on PENELOPE and the 15F body was irradiated isotropically at an antero-posterior angle.

Before beam irradiation, an air cuboid with the dimensions of 18 cm x 18 cm x 0.3 cm was placed in front of the body and following the simulation, the energy deposited inside was measured. As a result Air Kerma was calculated (section 2.2.2).

To calculate the dose coefficient at 60 kV and compare it with the other study, the dose in the lungs were calculated (*Table 13*) and normalised by dividing by the Air Kerma (*Eq. 16*).

Table 13. Dose coefficient data.

15F Phantom	Energy Deposited [eV/hist]	Mass [kg]	Absorbed Dose [Gy/hist]
Lung	2.74E+02	0.75	5.84E-17
Air Cuboid	3.38E-02	0.00011907	4.54E-17

$$Dose\ coefficient\ \left[\frac{Gy}{Gy}\right] = \frac{D\ [Gy]}{AirKerma\ [Gy]} = \frac{5.84E-17}{4.54E-17} = 1.29;$$

(Eq.16 [116]*)*

In his study Chang et al.[116] found a dose coefficent value 1.17. The value can be comparable since we have to consider an uncertainty due to the simulation about 20%. However other types of uncertainties can contribute to explain this discrepancy, such as different MC code, phantom used, cross sections, among others.

5.3.2 Results of the Absorbed Dose in the organs of each protocol.

Simulations to calculate the dose in the phantom organs were performed for the 10F and 15F phantoms and 3 protocols were analysed: Thorax, Head & Neck and Pelvic.

For each protocol an isocenter point was chosen. For the Thorax protocol, the lungs, for the Head & Neck the skull and for the Pelvic the pelvis were selectes. The source-isocenter distance was always 100 cm.

The CBCT beam was modelled as a conical beam with the opening angle set as the standard protocols [68].

As for the CBCT beam, simulations were done with X-ray beams at different voltages, from 40 kV to 120 kV in 10 kV steps, in order to understand how the absorbed dose changed.

In this section some of the results of MC simulations are reported. The full results of each simulation can be found in *Appendix II*. It is important to remark that the absorbed dose and energy deposition values in the following tables, have the Gy/history and eV/history units, namely the absorbed dose values are not absolute dose values, since they should be normalized for the total current and exposure time and should include a complete 3D rotation. The absorbed dose values here reported are used to study the relative dose variation among different protocols and exposure setup.

Table 14 shows an example of the tables in *Appendix II* where all the data are reported. Here are presented the results of Energy Deposition evaluated by the MC simulation in the brain after a MC simulation of the Thorax protocol. Then the Absorbed dose with the relative uncertainty was calculated.

Table 14. Absorbed dose evaluated for the lungs in Thorax protocol.

Lungs	**Phantom 10F**			**Phantom 15F**		
Tube Voltage [kV]	**En. Deposition [eV/hist]**	**Absorbed Dose [Gy/hist]**	**Dose % SD**	**En. Deposition [eV/hist]**	**Absorbed Dose [Gy/hist]**	**Dose % SD**
40	2.01E+03	6.44E-16	0.16%	2.83E+03	6.05E-16	0.11%
50	2.43E+03	7.79E-16	0.16%	3.32E+03	7.09E-16	0.11%
60	2.64E+03	8.47E-16	0.16%	3.55E+03	7.59E-16	0.11%
70	2.75E+03	8.83E-16	0.18%	3.67E+03	7.84E-16	0.11%
80	2.84E+03	9.08E-16	0.16%	3.76E+03	8.03E-16	0.08%
90	2.89E+03	9.25E-16	0.17%	3.82E+03	8.17E-16	0.12%
100	2.93E+03	9.38E-16	0.15%	3.88E+03	8.29E-16	0.10%
110	2.97E+03	9.51E-16	0.15%	3.93E+03	8.38E-16	0.10%
120	3.00E+03	9.63E-16	0.16%	3.98E+03	8.50E-16	0.09%

Absorbed dose and relative uncertainty data were extracted from the tables in *Appendix II* and plotted in *Figures 68-81*. It is safe to say that not every table is shown in this section in order to report the most important data without writing excessive information.

➢ Organ: *Lung.*

Figures 68,69,70 show the absorbed dose trend in the lung based on the tube voltage in the Thorax, Head & Neck and Pelvic protocol, respectively. .

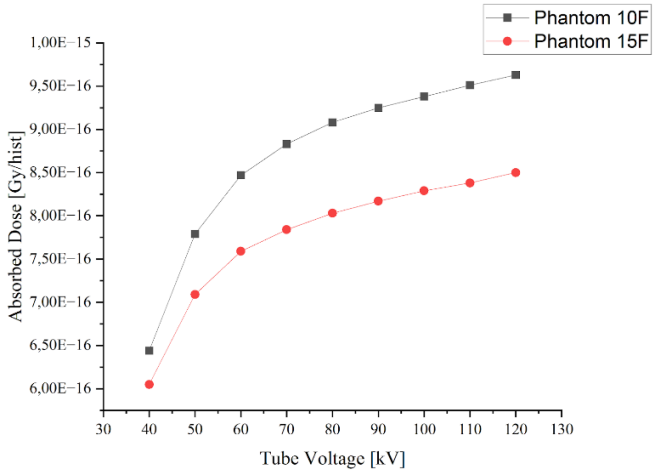

Figure 68. Absorbed dose in lung after Thorax protocol scan.

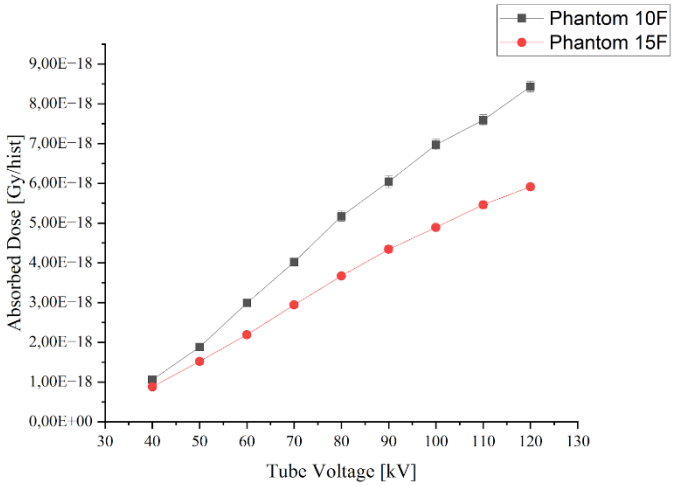

Figure 69. Absorbed dose in lung after Head & Neck protocol scan.

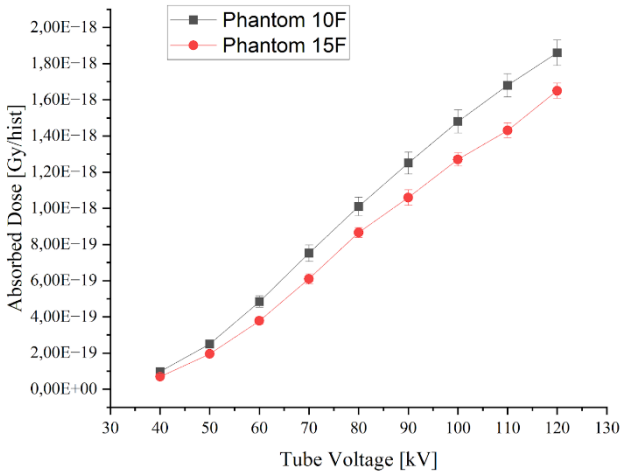

Figure 70. Absorbed dose in lung after Pelvic protocol scan.

➢ Organ: *Brain.*

Figures 71,72,73 show the absorbed dose trend in the brain based on the tube voltage in the Thorax, Head & Neck, and Pelvic protocol, respectively.

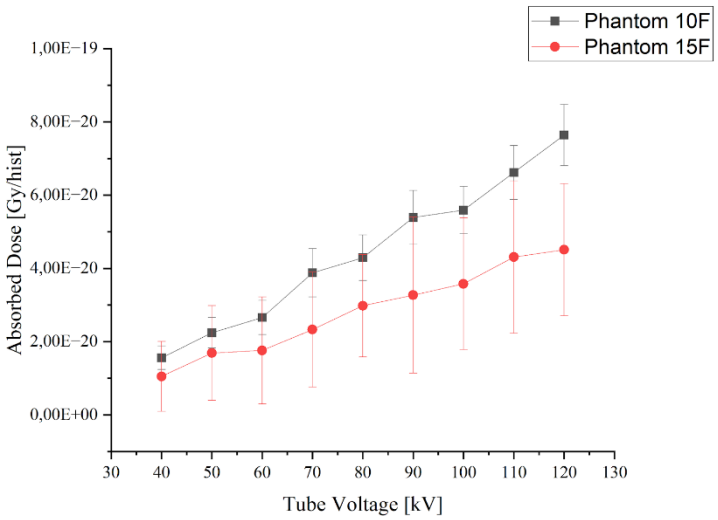

Figure 71. Absorbed dose in brain after Thorax protocol scan.

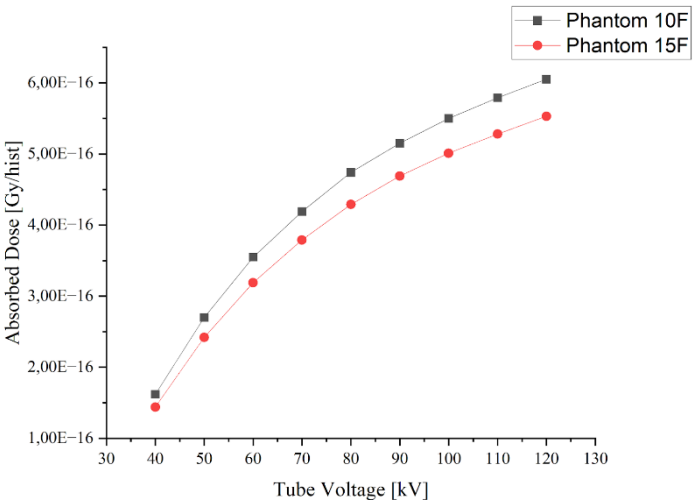

Figure 72. Absorbed dose in brain after Head & Neck protocol scan.

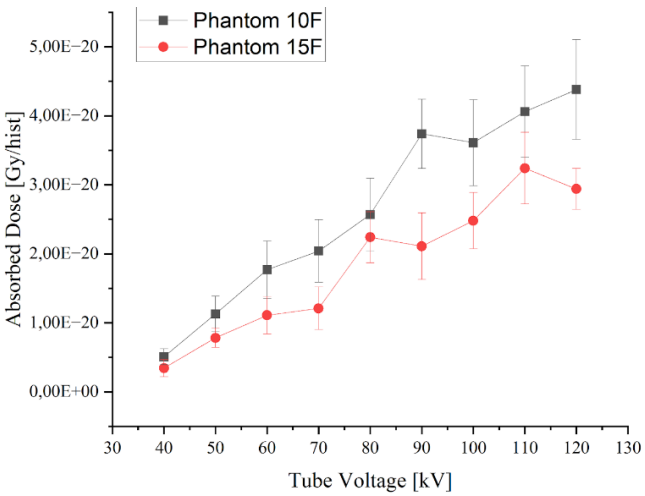

Figure 73. Absorbed dose in brain after Pelvic protocol scan.

➢ Organ: *Breast.*

Figures 74,75,76 show the absorbed dose trend in the breast based on the tube voltage in the Thorax, Head & Neck and Pelvic protocol, respectively.

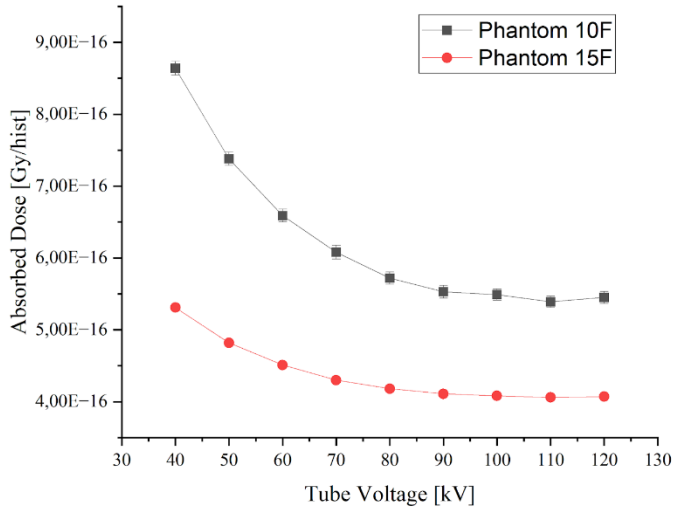

Figure 74. Absorbed dose in breast after Thorax protocol scan.

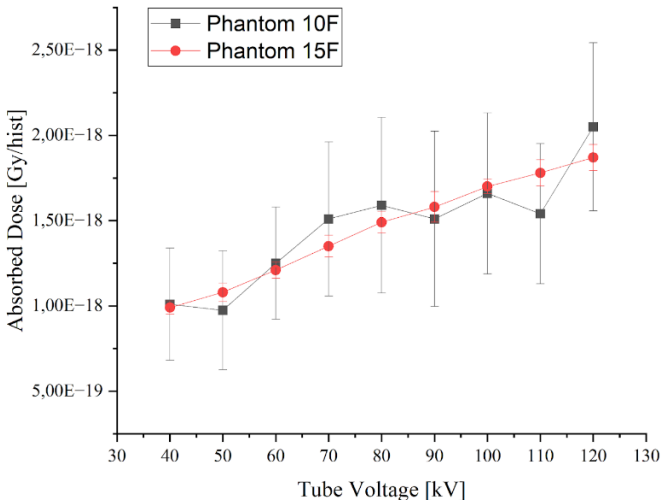

Figure 75. Absorbed dose in breast after Head & Neck protocol scan.

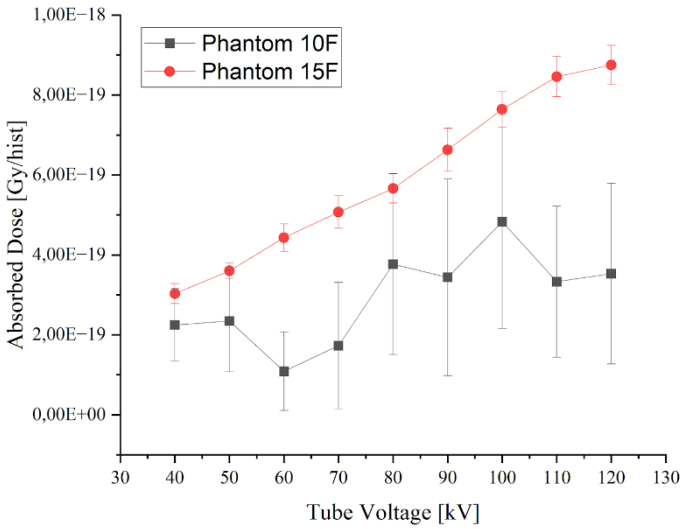

Figure 76. Absobed dose in breast after Pelvic protocol scan.

- Organ: *Heart Wall.*

  Figures 77,78,79 show the absorbed dose trend in the heart wall based on the tube voltage in the Thorax, Head & Neck and Pelvic protocol, respectively.

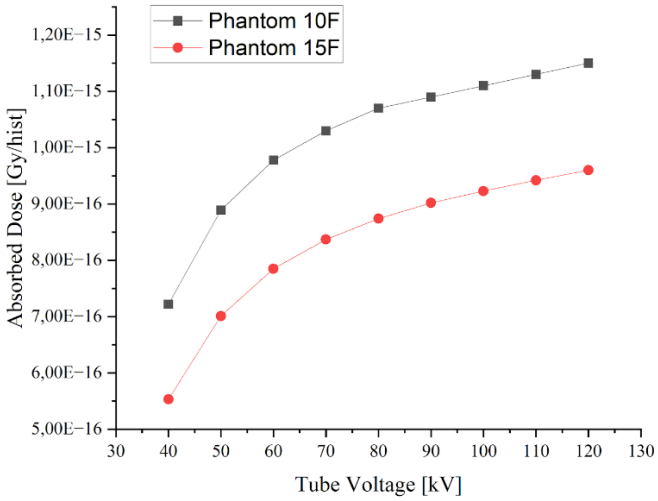

Figure 77. Absobed dose in heart wall after Thorax protocol scan.

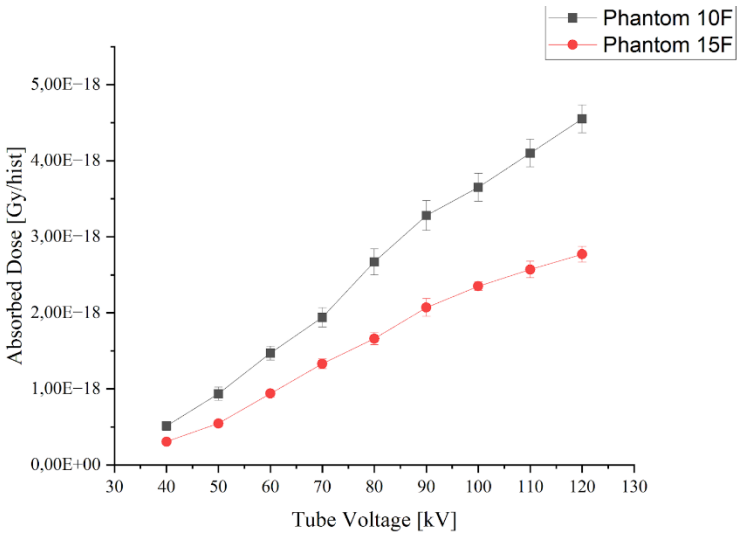

Figure 78. Absorbed dose in heart wall after Head & Neck protocol scan.

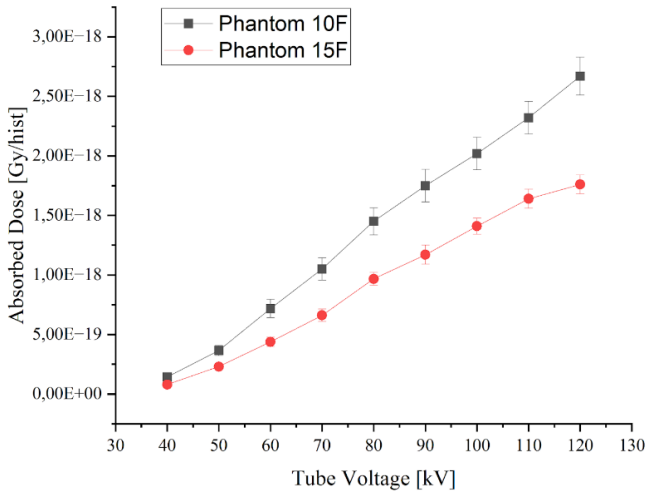

Figure 79. Absorbed dose in heart wall after Pelvic protocol scan.

- Organ: *Uterus*.

  Figures 80,81,82 show the absorbed dose trend in the uterus based on the tube voltage in the Thorax, Head & Neck and Pelvic protocol, respectively.

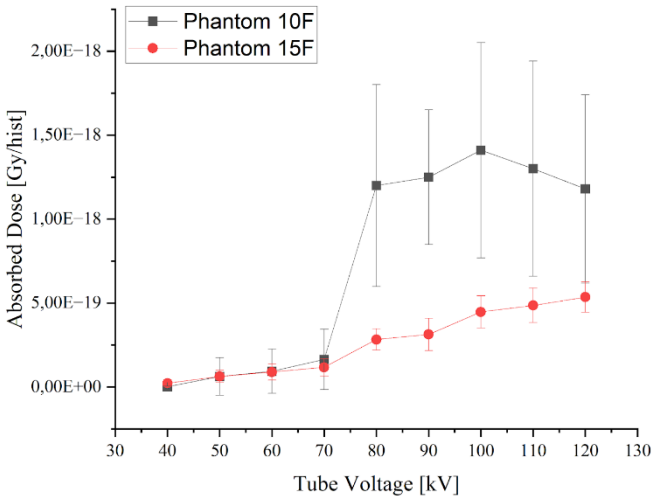

Figure 80. Absorbed dose in uterus after Thorax protocol scan.

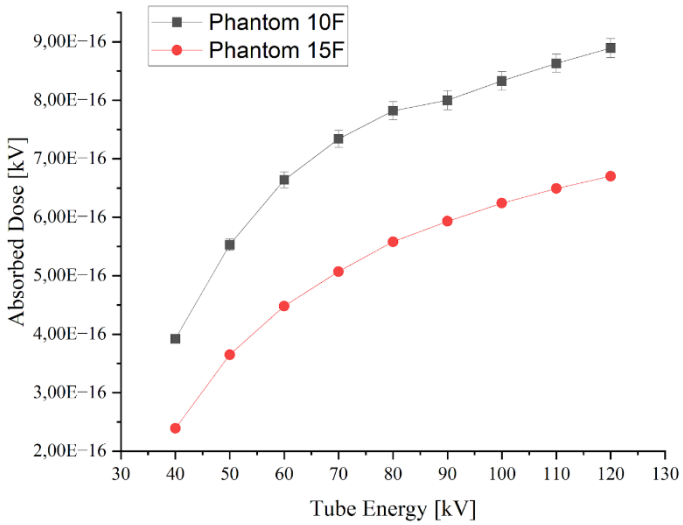

Figure 81. Absorbed dose in uterus after Head & Neck protocol scan.

5.3.3 Relative Variation of Absorbed Dose

The OBI Varian Clinac CBCT manual [68], shows the voltages at which the scans are done in the 3 different protocols:

- Thorax protocol: 100 kV;
- Head & Neck protocol: 100 kV;
- Pelvic protocol: 120 kV;

This chapter presents the results of the relative variation of absorbed dose, that would occur if a different tube voltage was used.

In this section, heart wall simulation results were taken as an example and plotted to show the decrease.

- Thorax protocol: 100 kV was taken as a reference, *Figure 82*.

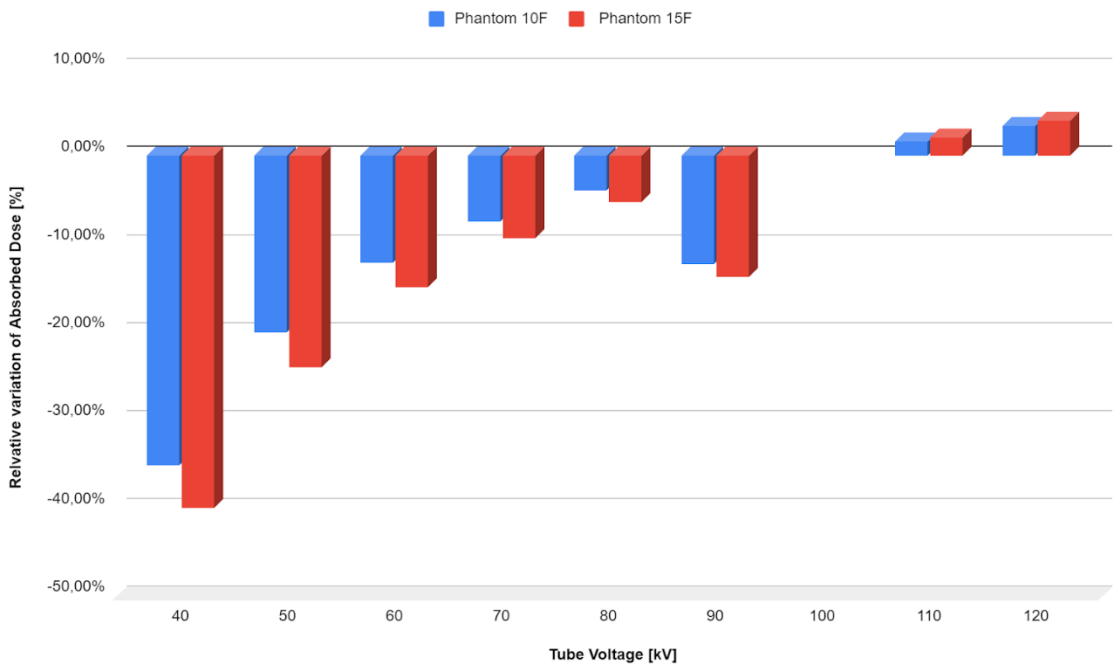

Figure 82. Relative Variation of Absorbed Dose based on the voltage in Thorax protocol.

➢ Head & Neck protocol: 100 kV was taken as a reference *Figure 83*.

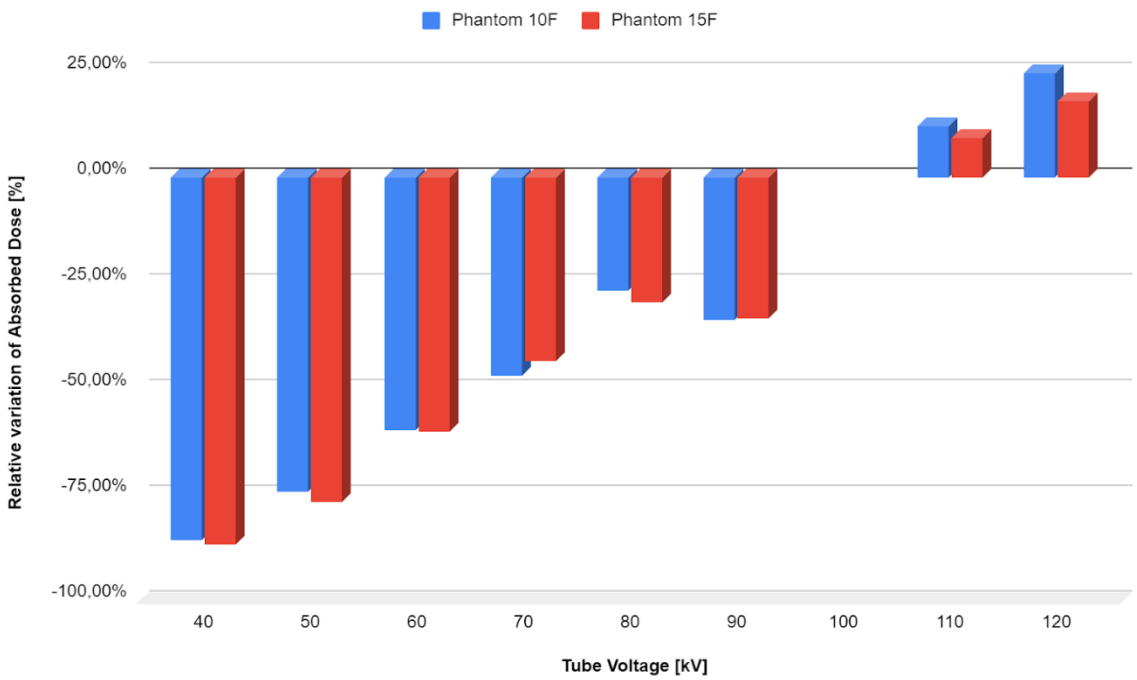

Figure 83. Relative Variation of Absorbed Dose based on the voltage in Head & Neck protocol.

➢ Pelvic protocol: 120 kV was taken as a reference, *Figure 84*.

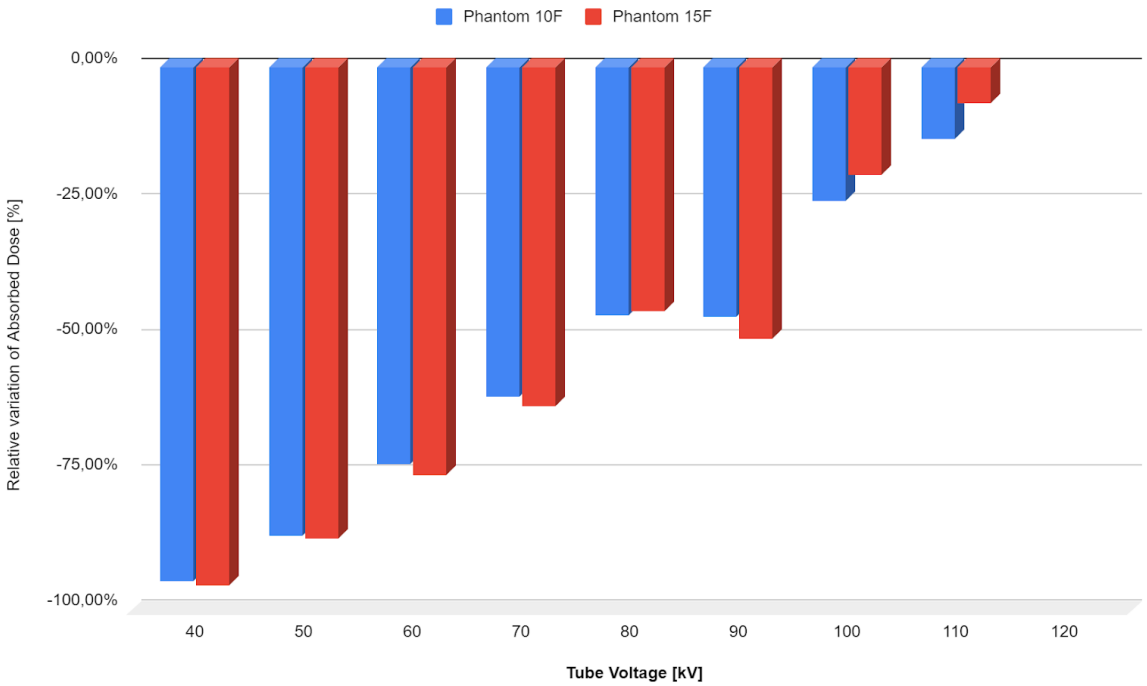

Figure 84. Relative Variation of Absorbed Dose based on the voltage in Pelvic protocol.

In first study of this thesis, it was found that a voltage of 60 kV would optimise the results from the point of view of the SDNR. If the voltage of 60 kV was used in the "heart wall" section of the body, there would be a decrease in dose of:

- Thorax protocol: 12.17% for the 10-year-old female body and 14.92% for the 15-year-old female body.
- Head & Neck protocol: 59.64% for the 10-year-old female body and 60.08% for the 15-year-old female body.
- Pelvic protocol: 73.12% for the 10-year-old female body and 75.06% for the 15-year-old female body.

The tables below show the decreases in dose absorbed by each organ if a 60 kV protocol were used instead of using standard clinac protocols.

Table 15. Relative variation of absorbed dose per organ at 60 kV.

	Phantom 10F			**Phantom 15F**		
Organ	**THORAX**	**HEAD**	**PELVIS**	**THORAX**	**HEAD**	**PELVIS**
Bladder	-70.66%	NC	-6.50%	-65.39%	NC	-16.71%
Brain	-52.36%	-35.50%	-59.60%	-50.88%	-36.25%	-62.12%
Breast	20.15%	-24.72%	-69.20%	10.47%	-28.77%	-49.36%
Eyes	-66.65%	18.65%	NC	-71.09%	18.64%	NC
Heart Wall	-12.17%	-59.64%	-73.12%	-14.92%	-60.08%	-75.06%
Kidney	-55.76%	NC	-58.71%	-61.64%	NC	-62.98%
Left Colon Cont	NC	NC	-23.76%	NC	NC	3.10%
Liver	-22.13%	NC	-64.84%	-27.90%	NC	-64.39%
Lung	-9.73%	-57.08%	-73.97%	-8.45%	-55.23%	-77.06%
Oesophagus	-24.59%	-60.31%	NC	-32.72%	-64.02%	NC
Ovaries	-68.40%	NC	-17.51%	-37.97%	-68.29%	-20.91%
Pancreas	-49.14%	NC	-57.52%	-56.30%	NC	-60.14%
Right Colon Cont	NC	NC	-12.51%	NC	NC	-0.17%
S intestine Cont	NC	NC	-10.12%	NC	NC	-11.34%
S intestine Wall	NC	NC	-11.58%	NC	NC	-13.48%
Spleen	-42.82%	NC	-66.14%	-49.00%	NC	-69.18%
Stomach Count	-39.65%	NC	-59.76%	-47.04%	NC	-61.01%
Stomach Wall	-37.70%	NC	-60.34%	-41.87%	NC	-58.89%
Thyroid	-5.26%	-59.61%	NC	-28.27%	-62.71%	NC
Uterus	-93.36%	NC	-25.38%	-80.19%	NC	-33.09%

Chapter 6

Discussion

6.1 Discussion – Study I: SDNR Analysis in a TOR phantom's CBCT Images

Looking at *Figures 40-41-42* results indicate that at Low-Medium-High contrast there is the same trend. From the first tube voltage measured, 40 kV, there is a slight increase up to 60 kV and then a slow decrease begins until 120 kV is reached.

As a first point, *Figures 36-37-38-39* show that as the energy increases, the values become saturated, and it is not even possible to identify parts of the object in the scans; this happens at voltages above 120 kV: 130 kV – 140 kV – 150kV.

Actually, this high energy level is not used in radiological imaging environments Voltages up to 125 kV are used in body sections with many bones, such as the pelvis, in order to be sure of obtaining an image with good resolution [66].

The values measured at these energies will not be considered in the percentage below because they are unused and saturated values, they were calculated to see the trend.

Returning to the data reported in the Results section 5.2.2, *Table 10*, the ROI data:

- At high contrast the SDNR values vary between 41.49 and 31.30 with a maximum at 60 kV and a minimum at 120 kV.
- At medium contrast, SDNR values vary between 22.98 and 18.12 with the maximum at 50 kV and the minimum at 120 kV.
- At low contrast, SDNR values vary between 11.44 and 6.49 with the maximum at 50 kV and the minimum at 120 kV.

The highest SDNR values were found when analysing the high-contrast section. Looking at the *Figures 29-40* the disc number 1 differs considerably from the background, consequently the SDNR ratio is higher.

When the SDNR is low it means that the ROI is more similar to the background and will therefore be more difficult to detect correctly.

Generally, for every disc selected, the SDNR's graphs show a decreasing trend and looking at the *Figures 41-42-43* the three graphs obtained show approximately the same trend.

Every graph has a peak around 50-60 kV, where the maximum SDNR value is reached, and then begin to decrease in a slightly linear fashion with an average percentage of 4.55% for the high-contrast region, 3.74% for the medium-contrast region and 7.63% for the low-contrast region, every 10 kV from 60 kV to 120 kV.

For example, if it's considered the high-contrast ROI, the maximum value at 60 kV is 41.49 while the minimum at 120 kV is 31.30, with an overall decrease in SDNR of 24.56%.

This shows how in reality having more energy does not always mean having more contrast, but it certainly means more exposure to radiation.
In each diagnostic imaging task, there is an optimal energy that is able to better visualize a given lesion or tumor mass with the lowest absorbed dose possible. Through the TOR phantom study, an optimal energy range was also identified. However, in order to deeply study the best energies for pediatric imaging in CBCT, further optimization studies, in terms of SDNR and absorbed dose are necessary, both with measurements with physical phantoms and MC simulations, and for each clinic task (e.g., lungs, liver, head, etc.).

6.2 Discussion – Study II: Experimental Acquisition of CBCT Spectra

Detector calibration

After the calibration line calculated (using the ^{241}Am and ^{152}Eu) the first trial was to calibrate the spectra of the radionuclides available and obtain graphs similar to those in the literature. The peaks found are in the same position and at the same distance it can be assumed the process of calibrating the detector was done correctly.

In the last session the collimator kit was used to filtering the beam, eliminating incorrect incoming photons. Collimators can have significant benefits, in particular they can be designed with specific holes or apertures to guide the X-ray beam to the best spot in the detector to acquire the signal. In semiconductor detectors such as the XR-100T-CdTe, one effect of collimators is to reduce the background photon count that may come from external sources or from the detector itself. This improves the sensitivity and accuracy of measurements, allowing a better distinction between signal and noise [96].

However, having a low photon count is not optimal for doing a proper statistical analysis, so the exposure time was increased. In this work the exposure time was 45 seconds acquiring at least 150’000 counts.

Acquisition took place at 40 kV, 60 kV, 80 kV and 100 kV.

The best results were found with:

- Distance: 40 cm;
- Collimator: 400 μm;
- Current: 20 mA;
- Exposure: 45 s

The spectra acquired, as reported in results section 5.2.2, present some differences with the ones shown in the literature. All the spectra acquired present the right endpoint at the kV peak of the voltage chosen, namely no photons were registered after the kV peak.

Spectra acquired in this study, like those in the literature and in accordance with this principle are lower than the indicated energy and have a Gaussian pattern, apart from the initial noise.

The Gaussian distribution in the X-ray beam is due to the statistical nature of the photon production processes. Inside the X-ray tube, high-energy electrons undergo random deviations when interacting with the target's atomic nuclei. This leads to the energies of the generated photons following a Gaussian distribution.

However, eventually, these are not comparable with the literature. To further investigate the differences, it has been also calculated the average energy of a spectrum.

The average energy of the spectrum refers to the weighted average of the energies of the photons in the spectrum. Since spectra can be characterised by a distribution of energies, calculating the average energy provides a representative value of the typical energy of the particles in the spectrum.

Even if the spectra have slightly different results from literature [97], the average energy is similar, and this could mean that the measured spectra present the same quality of the ones reported in literature.

- *Spectrum at 40 kV.*

The graph of the spectrum at 40 kV, *Figure 48* (section 5.2.2), shows that the trend is similar to the literature, *Figure 51*, but slightly shifted towards lower energies. In fact, the main peak in the measured spectrum is at about 25 keV, while in the literature, *Figure 51*, it is shifted to about 30 keV, and this observation is confirmed by the calculation of the average energy, which is 15.5% lower.

- *Spectrum at 60 kV.*

In the graph of the spectrum at 60 kV, *Figure 52* the trend is quite similar to the one reported in literature, *Figure 55*, even if the experimental spectrum is more "peaked", while the one in the literature is more "Gaussian". Both spectra have no counts beyond 60 keV which is correct as the beam was set to a maximum power of 60 kV.

As in the case of the 40 kV spectrum, the maximum in our spectrum is at a lower energy, at about 25 keV, whereas in the literature it is at about 37 keV, *Figure 55*.

One observation is that the peaks of the spectra at 40 kV and 60 kV were found at the same point even though different voltages were set.

The average energy value is 23.85% lower, 29.28 keV instead of 38.45 keV.

- *Spectrum at 80 kV.*

As the energy increases, the deviation from the literature becomes more relevant.

Figure 56 show the spectra at 80kV, looking at the image and comparing with the literature, *Figure 59*, it can be seen they are not very similar, in the experimental one an initial peak at 25 keV is found and then a downward trend up to 80 keV. In fact, in the literature the graph, *Figure 59* is more like a Gaussian, with a maximum at 42 keV and then a peak at around 60 keV is shown.

Figure 59 shows also the phenomenon of the 'tungsten peak'. In X-ray spectra above 60 keV occurs this characteristic due to the properties of the material used for the X-ray tube cathode, which is typically tungsten.

This peak is due to the emission of characteristic X-rays caused by the transition of an electron in the tungsten target from a higher to a lower energy state and manifests itself as a distinctive peak line in the X-ray spectrum at this specific energy.

It is important to note that the shape and intensity of the peak at 60 keV may vary depending on equipment settings and acquisition parameters.

In the experimental spectrum at 80 kV, given the tungsten anode of X-ray tube, it’s expected this peak at these energies. However, in the 60-65 keV range, only an increase in counts is present.

As in previous results, the spectrum is shifted towards the lower energies with an average energy of 34.84 keV, whereas it’s expected 45.98 keV (24.23% of difference).

- *Spectrum at 100 kV.*

The spectrum acquired at 100 kV is very different from the previous ones, *Figure 60*. The shape is shifted towards high energies. It starts with a very slow trend up to a maximum at 70 keV, then a stabilization up to 80 keV is noted, from which a fast downward trend starts up to 100 keV.

This is the only case where the calculated average energy is higher than in the literature, 63.64 keV against 52.09 keV of literature. An increase of 18.15% is observed.

To conclude, some possible explanation for the discrepancies between measured and literature spectra are:

- System settings: Check the settings of the CBCT beam acquisition system. Make sure that the X-ray tube is correctly configured to produce the desired energy range and that the energy setting is correct. Also check other system settings, such as tube current, exposure time and filtering options, as these can affect the shape and energy of the spectrum.
- Calibration: Ensure that the CBCT beam acquisition system is correctly calibrated. Inaccurate or incorrect calibration could affect the shape and energy of the measured spectrum. Also check if there are firmware or software updates available for the system that could correct any calibration problems.
- Problems with the X-ray tube: The X-ray tube may be damaged or malfunction, affecting the quality and energy of the spectrum. Check the X-ray tube for signs of failure or abnormality and consider the need for maintenance or replacement.
- Filter or collimator: Check whether the CBCT beam acquisition system is equipped with appropriate filters or collimators. These components can influence the shape and energy of the spectrum by adjusting the amount and energy of photons reaching the detector. Make sure they are correctly installed and configured for your specific needs.
- Misalignment: If the detector is not correctly aligned with the X-ray beam, several negative effects may occur such as reduced detection efficiency; spectrum distortion that may cause a shift in the average energy of the spectrum or a deformation of its shape; unwanted scattering effects, which may introduce photons with different energies into the spectrum, affecting the energy distribution and shape of the acquired spectrum.

However, considering the system settings, calibration, and problems with the X-ray tube, everything was verified in section 5.2.1, showing that the calibration was done correctly and the same X-ray tube and system settings were used for other studies, such as the SDNR study.

The various filters of the machine and the detector do indeed influence the spectrum shape a lot and should be better investigated. Alignment is very critical for CdTe detectors and should be always treated with great accuracy.

Given the lack of information of other spectra present in literature, a comparison was also made without considering the 2.8 mm aluminium filter.

➢ *Spectrum at 40 kV.*

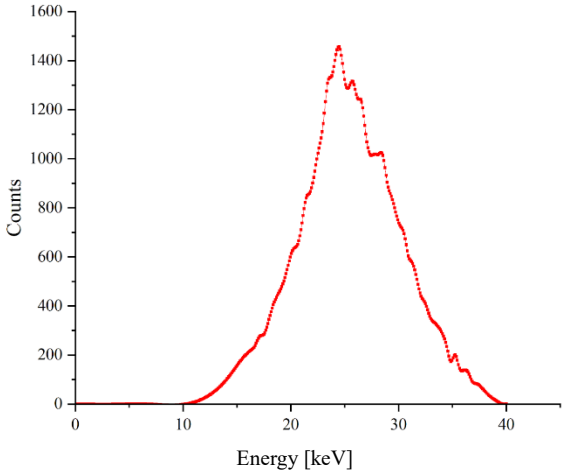

Figure 85. Experimental 40 kV spectrum post processed.

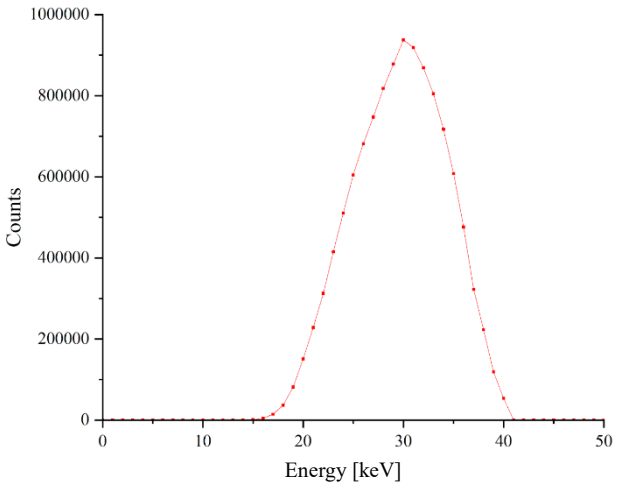

Figure 86. 40 kV spectrum with 2.8 mm Al filter [97].

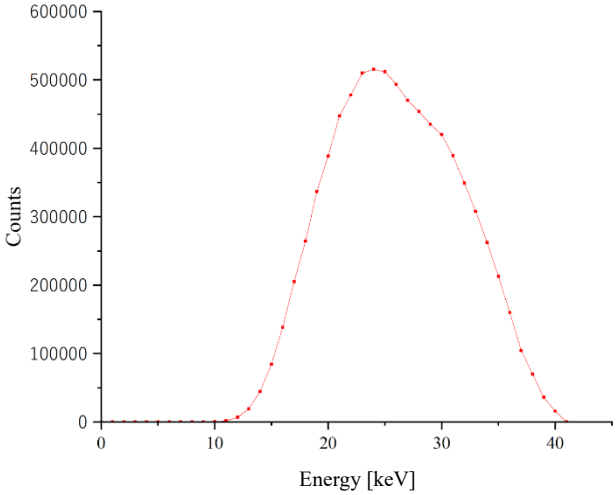

Figure 87. 40 kV spectrum no filter [97].

The difference between the two spectra taken from the literature is the presence of a 2.8 mm aluminium filter in the *Figure 87*. The spectrum is shifted towards the higher energies, so it can be said that the filter cuts the lower energies.

Comparing the experimental spectrum, *Figure 85*, of this study with that in the literature without the filter, *Figure 86*, some similarities can be observed. Both graphs show a peak around 25 keV, with a subsequent downward trend with a small rise around 30 keV.

The graph of the spectrum at 40 kV without filter seems to be more similar to that obtained from this research.

➢ *Spectrum at 60 kV.*

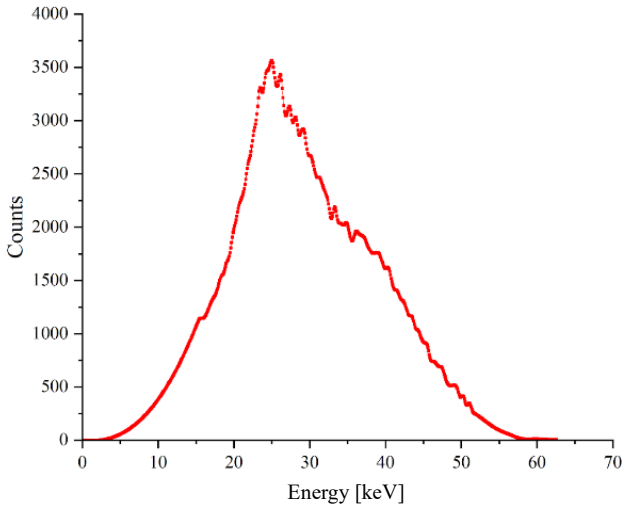

Figure 88. Experimental 60 kV spectrum post processed.

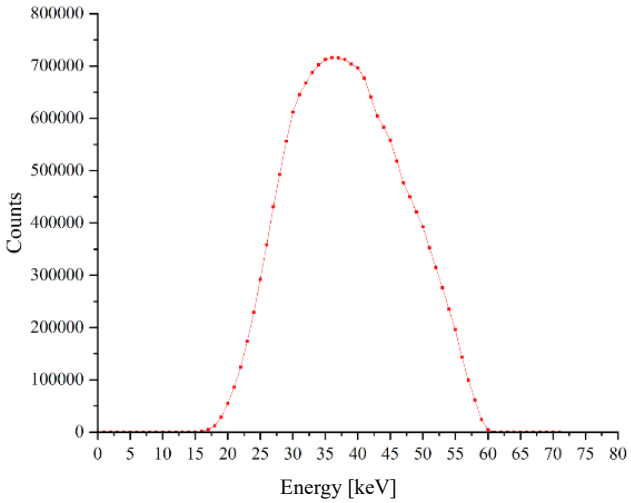

Figure 89. 60 kV spectrum with 2.8 mm Al filter [97].

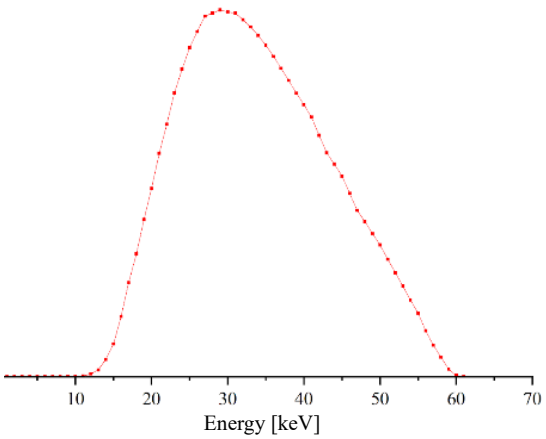

Figure 90. 60 kV spectrum no filter [97].

As in the case of the spectrum at 40 kV, the effect of the aluminium filter can also be seen at 60 kV, which shifts the maximum towards higher energies, *Figure 89*.

However, even in this case the graph of the spectrum without the filter, *Figure 90*, seems to be more similar to the experimental one, *Figure 88*, presenting a peak around 30 keV and then a downward trend up to 60 keV.

➢ *Spectrum at 80 kV.*

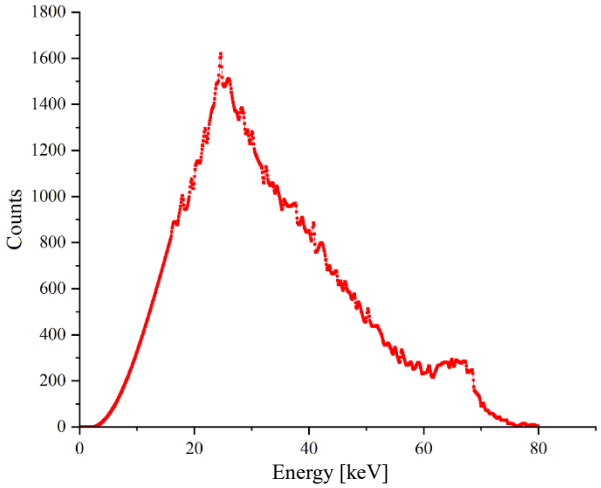

Figure 91. Experimental 80 kV spectrum post processed.

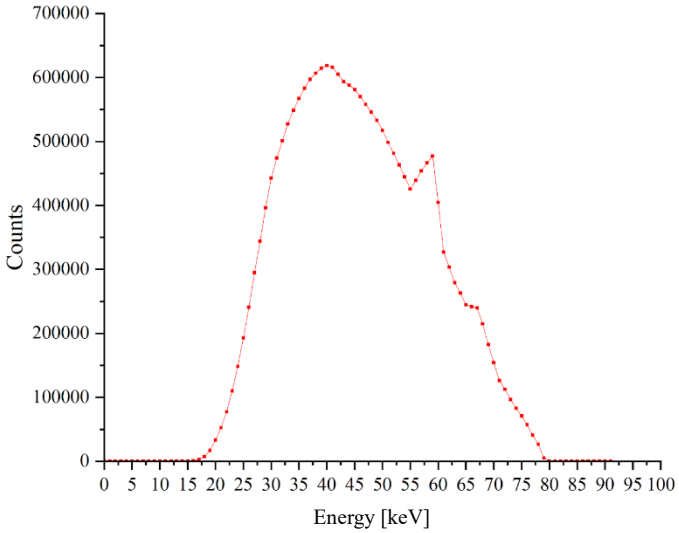

Figure 92. 80 kV spectrum with 2.8 mm Al filter [97].

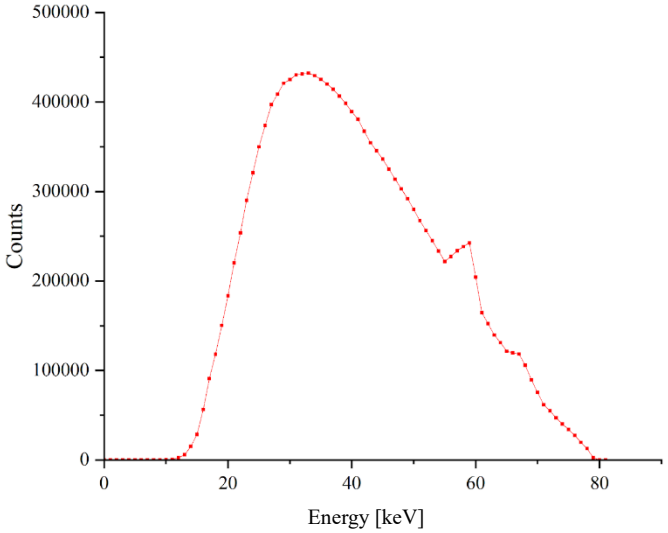

Figure 93. 80 kV spectrum with no filter [97].

The same reasoning can be done at 80 kV, the spectrum without filtering, *Figure 93*, seems to be more similar.

In general, what can be seen in all these graphs is that in the literature, *Figure 92 & 93* the trend follows a Gaussian, whereas the experimental ones, *Figure 91,* have a sharp peak, this is the major difference and may be due to not having accumulated enough photons for a good statistical probability.

To complete the discussion, the average of the spectra without filter was calculated and compared with those found previously (section 5.2.2).

Without filter, the average energy is much closer to that found experimentally:

- at 40 kV with the Al filter there was a difference of 15.5%, changed to 1.2%;
- at 60 kV with the Al filter there was a difference of 23.85%, changed to 13.63%;
- at 80 kV with the Al filter there was a difference of 24.23%, changed to 14.61%.

Table 16. Mean energy comparison between experimental and literature spectra.

Tube Voltage [kV]	**Experimental Mean Energy [keV]**	**No filter Mean Energy (literature spectrum) [keV]** [97]	**Relvative Variation [%]**	**2.8 mm Al filter Mean Energy (literature spectrum) [keV]** [97]	**Relative Variation [%]**
40	25.65	25.96	1.2%	29.59	15.5
60	29.28	33.90	13.63%	38.45	23.85
80	34.84	40.80	14.61	45.98	24.23

Since the experimental spectra presented significant differences with literature data, it was decided to use literature data for the MC simulations in the next chapter. However, energy spectra study performed in this Thesis, highlights the importance to accurately estimate the CBCT X-ray, since it could greatly influence the imaging and dosimetry aspects.

6.3 Discussion – Study III: Dose assessment in pediatric CBCT

In this study, were analysed the radiation dose absorbed by organs of three different imaging protocols using CBCT imaging. Depending on the part of the body to be analysed, a certain protocol is used to optimize the acquisition. The three main protocols are: Thorax, Head & Neck and Pelvic. For each of these, a target point was taken and a CBCT beam was simulated.

Thorax protocol

In the Thorax protocol the first organ analysed is the lung.

Figure 94 shows the trend of the absorbed dose based on the voltage level. In the brain as the energy increases, the values of the absorbed dose increase, this is an expected effect for the higher photon average energy.

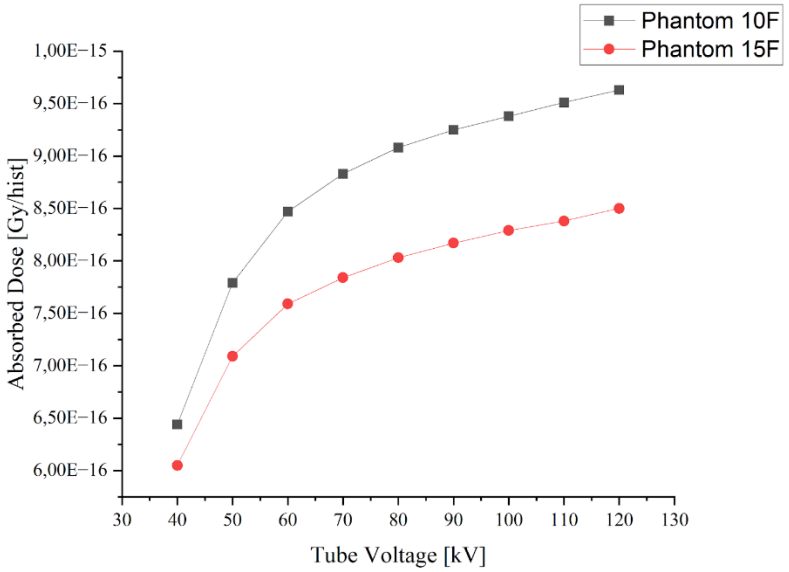

Figure 94. Absorbed dose by the lung during CBCT Thorax protocol.

The trend is upward and there is a variation between the absorbed dose from the 15F phantom and the 10F phantom. In detail the 10F absorbed more dose, because the mass of the organ is smaller, so per unit mass the radiation is higher.

The *Table 36 (Appendix II)* shows that the energy deposited, in the smaller body is inferior because the organ is smaller, but the absorbed dose is higher.

This is one of the reasons why attention must be paid to pediatric patients[13],[14].

A further observation in *Table 36* is that in this simulation the uncertainty found is very low, about 0.2%. This is good result obtained because the organ was the point of scan and there were less scattered effects.

Analysing the brain, an organ out of the range of the CBCT scan in this Thorax protocol, *Table 26 (Appendix II)* the absorbed dose values are significantly lower than those of the previous lung. This is because the CBCT beam is not centred in the brain, so only scatter effect could be figured out.

Figure 95 shows the trend of the absorbed dose in the brain with the relative uncertainty.

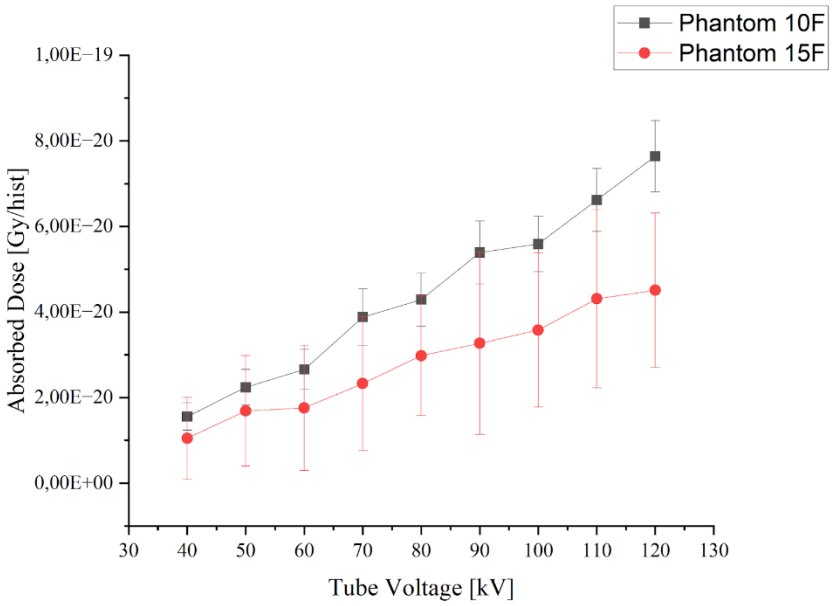

Figure 95. Absorbed dose by the brain during CBCT Thorax protocol.

An upward linear trend can be seen in *Figure 95*. There is a high uncertainty (about 20%), probably due to the presence of only secondary radiation. To obtain a more accurate measurement, the simulation should run more time to have more statistics.

Below, in *Figure 96* the plot of the absorbed dose in the uterus is reported. This organ is far from the cone beam trajectory and present a small dimension. In the 10F phantom it's 327.5 times smaller than the brain *(Tables 21 – 22 in Annex I)*.

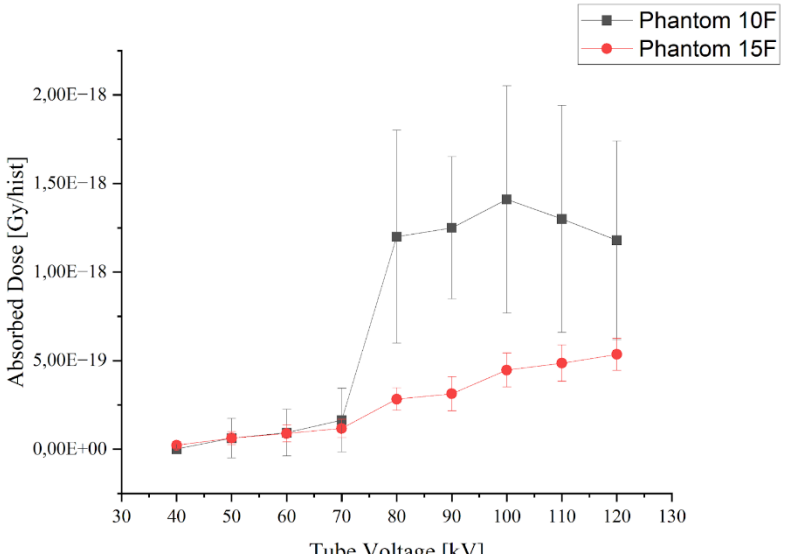

Figure 96. Absorbed dose by the uterus during CBCT Thorax protocol.

Figure 96 shows a trend similar to the previous organs, the energy deposited is even less than in the brain *(Table 34 in Appendix II)*. Both because it is not the main target organ and because it is a very small organ. It's to remark that the uncertainty is very high, even reaching the 100%.

An interesting organ to analyse is the breast, the data in *Table 35* in *Appendix II* are resumed in *Figure 97* below and show how the trend decreases with the increasing energy:

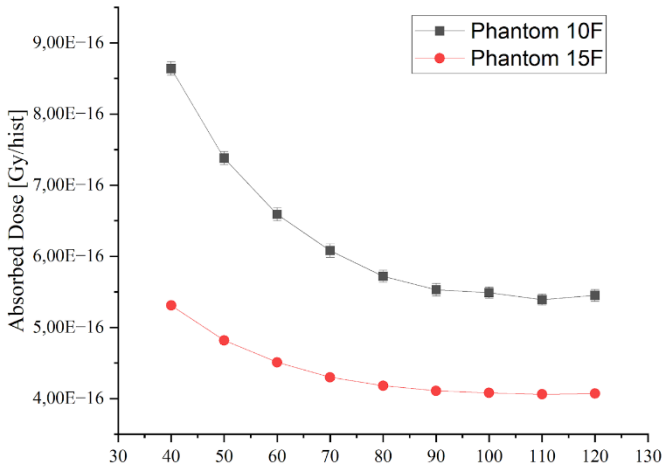

Figure 97. Absorbed dose by the breast during CBCT Thorax protocol.

This is the only organ of this protocol representing an inverse trend. As one of the most exposed organs in the thorax protocol, the deposited energy is accurately calculated, with an average uncertainty of about 1%.

In general, in the Thorax protocol the most affected organs with the highest absorbed dose are those directly irradiated by the CBCT beam: lung, liver, heart wall and breast.

Slightly more distant, there are the: pancreas, kidney, spleen, thyroid and oesophagus.

The most distant and less affected organs that also have a very high uncertainty are the: brain, bladder, eyes, stomach, ovaries and uterus.

For the general calculation of the relative variance of the absorbed dose these last organs were not counted because they always present an uncertainty of more than 10%, up to 100%, which was not considered acceptable.

The *Table 17* below displays for every organ the relative variation in percentage of absorbed dose of a 60 kV Thorax protocol scan, compared to a standard protocol at 100 kV.

Table 17. Relative variation of absorbed dose in a Thorax protocol at 60 kV compared to 100 kV.

60 kV - Thorax protocol	**Relative Variation of Absorbed Dose [%]**	
Organ	**Phantom 10F**	**Phantom 15F**
LIVER	-22.13%	-27.90%
PANCREAS	-49.14%	-56.30%
EYES	-66.65%*	-71.09%*
HEART WALL	-12.17%	-14.92%
BRAIN	-52.36%*	-50.88%*
KIDNEY	-55.76%	-61.64%
STOMACH_WALL	-37.70%	-41.87%
SPLEEN	-42.82%	-49.00%
THYROID	-5.26%	-28.27%
BLADDER	-70.66%*	-65.39%*
OVARIES	-68.40%*	-37.97%*
OESOPHAGUS	-24.59%	-32.72%
UTERUS	-93.36%*	-80.19%*
BREAST	20.15%	10.47%
LUNGS	-9.73%	-8.45%
STOMACH_COUNT	-39.65%	-47.04%

For the measurement of the average decrease of absorbed dose, organs with an uncertainty higher than 10% were not considered because the statistical uncertainty was too high (in * those not counted in the average). For the 10F phantom an average decrease of 25.35% was reached, whereas in the 15F a decrease of 32.51% was observed.

Before the organs were divided based on the distance from the beam, the relative variation of the absorbed dose could change depending on where the part of the body analysed is, below the data found dividing in 3 areas:

1. Irradiated area: lung, liver, heart wall and breast where the percentage decreases of 5.97% in the 10F phantom and 10.20% in the 15F;
2. Peripherals are: pancreas, eyes, kidney, stomach, spleen, thyroid and oesophagus where in the 10F phantom decreases of 35.51%, while in the 15F of 45.59%;
3. Distant area: brain, bladder, eyes, stomach, ovaries and uterus in which the relative variance is for the 10F phantom of 61.25% and for the 15F of 56.35%.

The most distant organs would be the ones with the best benefit. It's safe to remark that the same organs are the ones with the highest uncertainties.

Head & Neck protocol

In the Head & Neck protocol the isocenter was placed in the cranium.

Data obtained from the brain, the main organ irradiated, are shown in *Figure 98* below. As the voltage increases, there is an increase in the absorbed dose. The difference between the two phantom is tight, less than 10%, firstly because the mass of the organ is approximately the same *(Tables 21-22 in Annex I)* secondly for the 10F phantom could be higher because of the smaller body size that increases the exposure.

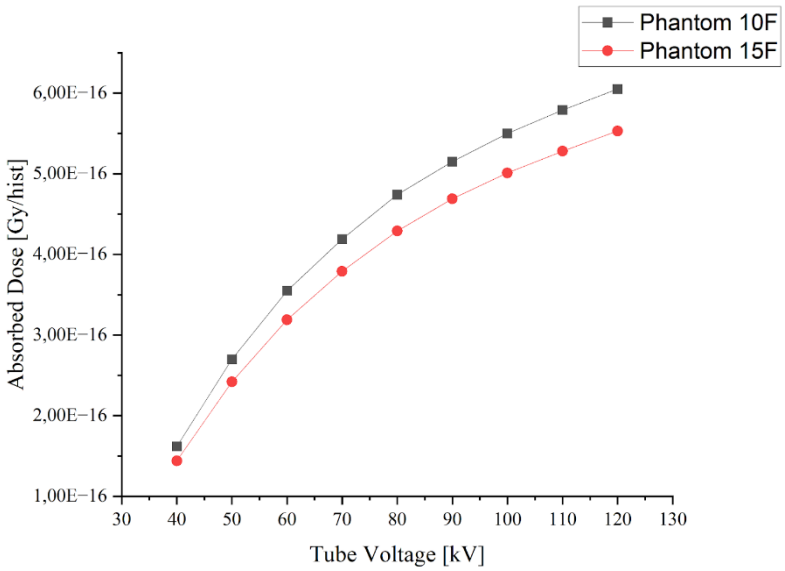

Figure 98. Absorbed dose by the brain during CBCT Head & Neck Protocol.

The trend represented in *Figure 98* confirms the results of the first protocol analysed, in this organ the percentage uncertainty less than 0.3% (*Table 38 in Appendix II*). The brain was also studied in the first protocol and the main difference shown by the *Figure 95* is the graph trend, in this case it seems to be logarithmic, while in *Figure 95* is linear.

Probably when the organ is directly irradiated moves with logarithmic trend, while if it's in a peripheral area it grows with a linear trend.

To confirm this hypothesis the graph of the lungs is reported below, *Figure 99*.

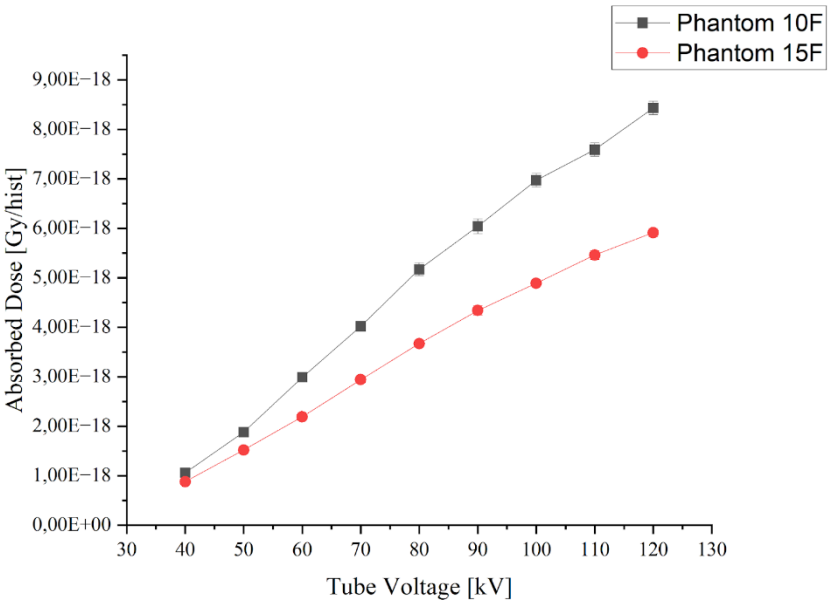

Figure 99. Absorbed dose by the lungs during CBCT Head & Neck Protocol.

This graph confirms the hypothesis. Here the absorbed dose grows in linear scale, while in *Figure 94*, in the thorax protocol, the trend is logarithmic.

With the brain, the other most irradiated organ in this protocol are the eyes.

The absorbed dose graph is shown in *Figure 100*.

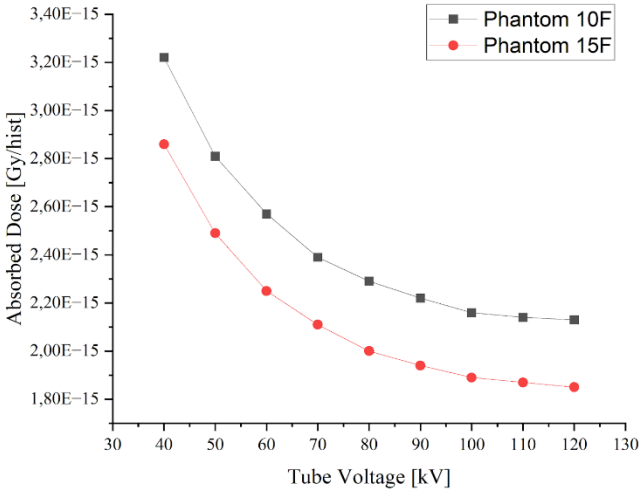

Figure 100. Absorbed dose by the eyes during CBCT Head & Neck Protocol.

Similarly, to the trend of the breast in the thorax protocol, eyes have the same downward trend. Decreasing the voltage increases the absorbed dose. The percentage uncertainty is really low, in average of about 0.5%.

In the Head & Neck protocol the organs with the highest absorbed dose are the brain and eyes, then out of the radiation fields the thyroid and oesophagus and more distant the breast, lung, heart wall and ovaries present a decreasing absorbed dose trend.

Some organs were not included in the general calculation of the relative variation of the absorbed dose because they consistently exhibit statistical uncertainty of more than 10%, up to 100%.

Table 18 displays for every organ the relative variation in percentage of absorbed dose of a 60 kV Head & Neck protocol scan, compared to a standard clinical protocol at 100 kV.

Table 18. Relative variation of absorbed dose in a Head & Neck protocol at 60 kV compared to 100 kV.

60 kV – Head & Neck protocol	**Relative Variation of Absorbed Dose [%]**	
Organ	**Phantom 10F**	**Phantom 15F**
EYES	18.65%	18.64%
HEART WALL	-59.64%	-60.08%
BRAIN	-35.50%	-36.25%
THYROID	-59.61%	-62.71%
OVARIES	-96.12%*	-68.29%*
OESOPHAGUS	-60.31%	-64.02%
BREAST	-24.72%*	-28.77%
LUNGS	-57.08%	-55.23%

Overall, in the 10F phantom an average decrease of 36.86 % and in the 15F of 41.20 % was observed, if using a 60 kV protocol instead than a 100 kV one.

Dividing the body in 3 different areas was found:

1. Irradiated area: eyes and brain the percentage decreases of 8.43% in the 10F phantom and 8.81% in the 15F;
2. Peripheral area: thyroid and oesophagus where in the 10F phantom decreases of 59.96%, while in the 15F of 62.71%;
3. Distant Area: breast, lung, heart wall, ovaries in which the relative variance is for the 10F phantom of 59.39% and for the 15F of 53.09%.

Also in this protocol, directly irradiated organs have a smaller percentage decrease, while peripheral organs would have a larger decrease. On the other hand, when analysing the differences between the two phantoms, no particular changes can be seen, the percentages are very similar.

Pelvic protocol

In the Pelvic protocol the CBCT beam was focused to the pelvic area which involves a series of organs located in the lower part of the abdomen.

Figure 101 represented the plot of the absorbed dose of the bladder, one of the most exposed organs. A slight logarithmic increasing of the dose is noticed. The absorbed dose in the phantom 10F is double with respect to the 15F, probably because the mass is almost the half in the 10F, 30g (*Table 21 in Annex I)* compared to the 50g of the 15F, and the energy deposited in the organ is almost the same (*Table 55 in Appendix II).*

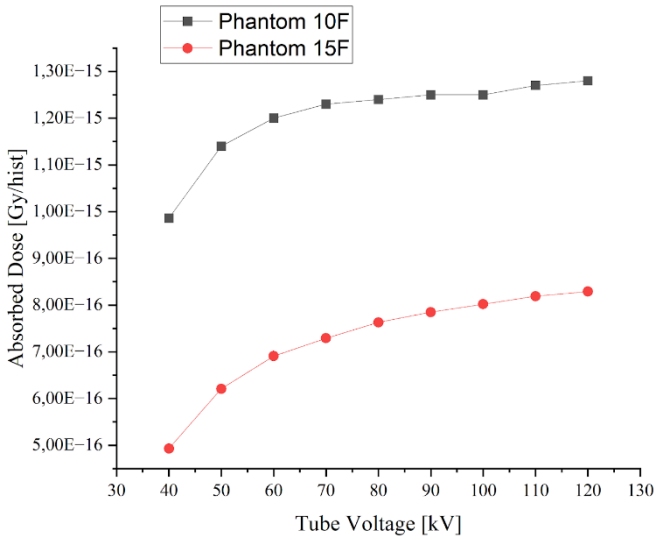

Figure 101. Absorbed dose by the bladder during CBCT Pelvic Protocol.

Figure 101 confirms the logarithmic upward trend found in the previous protocols and the small statistical uncertainty of less than 1%.

Analysing a more distant organ from the CBCT beam radiation field, the same trend for the peripheral organs was found. In the *Figure 102* are represented the data of the lungs to be analysed and compared with the other protocols.

The image displays a linear upward trend with a close difference between the two phantoms.

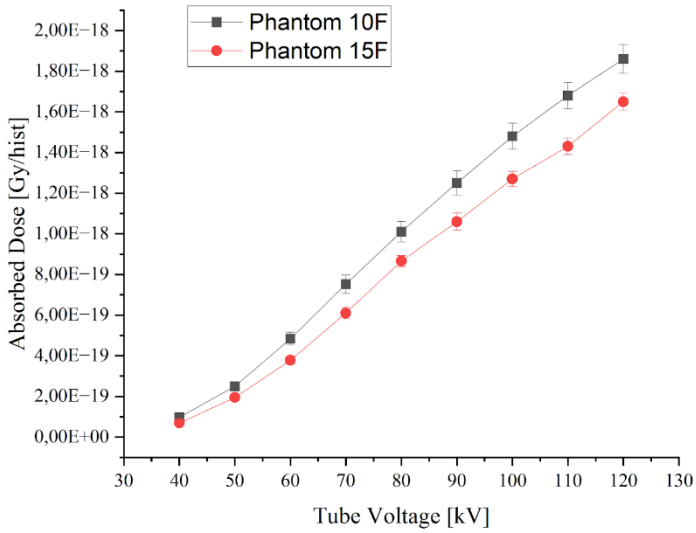

Figure 102. Absorbed dose by the lungs during CBCT Pelvic Protocol.

The statistical uncertainty is not irrelevant but always below the 10%, with an average of about 5%. The plot is more pendent respect the previous one with an increase of 1898% for the 10F and 2376% for the 15F from 40 kV and 120 kV.

Pelvic protocol is a critical protocol [117] because the irradiated area contains a lot of vital and sensitive organs, especially for female: bladder, ovaries, uterus, intestine and near the stomach, liver, spleen, pancreas, kidney can be found. Furthermore, is difficult to analyse due to the pelvis bones that may obstruct imaging analysis [118].

The *Table 19* displays for every organ the relative variation in percentage of absorbed dose of a 60 kV Pelvic protocol scan, compared to a standard clinical protocol at 120 kV. The brain is not included in the general calculation of the relative variance of the absorbed dose because of the high uncertainty margin of more than 10%, up to 40%.

Table 19. Relative variation of absorbed dose in a Pelvic protocol at 60 kV compared to 100 kV.

60 kV - Pelvic protocol	Relative Variation of Absorbed Dose [%]	
Organ	**Phantom 10F**	**Phantom 15F**
LIVER	-64.84%	-64.39%
PANCREAS	-57.52%	-60.14%
HEART WALL	-73.12%	-62.12%
BRAIN	-59.60%*	-75.06%*
KIDNEY	-58.71%	-62.98%
STOMACH_WALL	-60.34%	-58.89%
S intestine Wall	-11.58%	-13.48%
SPLEEN	-66.14%	-69.18%
BLADDER	-6.50%	-16.71%
OVARIES	-17.51%	-20.91%
UTERUS	-25.38%	-33.09%
BREAST	-69.20%	-49.36%
LUNGS	-73.97%	-77.06%
STOMACH_COUNT	-59.76%	-61.01%
S intestine Cont	-10.12%	-11.34%
Right Colon Cont	-12.51%	-0.17%
Left Colon Cont	-23.76%	3.10%

Analysing data was found that 10F phantom has an average absorbed dose decrease of 43.19 % and in the 15F of 41.11%.

With this protocol the highest number of organs was analysed, can be divided in:

1. Irradiated area: bladder, uterus, ovaries, intestine decreases of 15.34% in the 10F phantom and 13.22% in the 15F;
2. Peripheral area: liver, pancreas, spleen, kidney and stomach where in the 10F phantom decreases of 61.80%, while in the 15F of 64.17%;
3. Distant Area: breast, lung, heart and brain in which the relative variance is for the 10F phantom of 68.97% and for the 15F of 65.90%.

Organs not directly irradiated could have a great decrease of absorbed dose if the voltage would reduce. These results compared to the other protocols are consistent and aligned showing the same trend. However, it is important to remark that the absorbed dose results should be always analysed taking into account also the imaging performances for real clinical case applications.

After analysing the three protocols the main features observed are:

- Most of the time the trend is upward, increasing the voltage increases the average energy of the spectrum and thus increases the energy deposited in the organ.
- The breasts during the thorax protocol and the eyes during a head & neck protocol, present an inverse trend with respect to the general increasing trend of the absorbed dose with kV. In these two cases decrease in voltage would lead to a higher absorbed dose. The radiation exposure in the other protocols is in line with the main trend; while considering these organs as 'target point' they show an inverse behaviour. The trend of absorbed doses mainly depends on the tissue materials, exposure to primary or scatter radiation and energy of the beam, among others. In conclusion, this trend reflects the issue that for each clinical task there a unique trend that depends on the parameters before discussed.
- The peripheral organs are those that would benefit most from a decrease in voltage, reducing the absorbed dose by up to 60%. The organs under the x-ray beam would also have an improvement of up to 15%.
- The pattern of absorbed dose in organs is the same in both phantom 10F and 15F. However, all graphs show that the 10F is more exposed to radiation. This could be due to the body size, which being smaller, the CBCT beam directly irradiates more parts of the body. From the Tables in *Appendix II*, the deposited energy is similar between the two bodies, but the 10F has the smaller and less developed organ and therefore the absorbed radiation is higher.

Chapter 7

Limitations

In this paragraph the possible limitations linked to the methods used in this study are reported.

I think it is useful to talk about them in order to provide an accurate assessment of the results and to ensure the transparency and integrity of the research. Limitations represent the constraints, restrictions or weaknesses inherent in the study that may affect the reliability or applicability of the results obtained.

In particular, I would like to report the limitations of this scientific study for the following reasons:

- Accuracy and scientific honesty: The inclusion of limitations helps to avoid incorrect or misleading presentation of results. Making the limitations explicit allows readers and other researchers to correctly assess the scope and interpretation of the results, avoiding overestimates or invalid conclusions.
- Awareness of bias: Limitations may arise from biases intrinsic to the study, such as the use of non-ideal measurement instruments or the effect of uncontrolled independent variables. Highlighting these limitations allows readers to better understand potential weaknesses in the study and critically evaluate the results.
- Scientific progress: Identifying and discussing limitations can stimulate further research and future investigations. Recognising what has been limited or not fully addressed in a study can provide insights into new research questions and improve the design of future studies.

7.1 Limitations – Study I: SDNR Analysis in a TOR phantom's CBCT Images

1. The first and most important limitation concerns the density and composition of the TOR 18FG phantom, since the densities of the object are not reported in literature, increasing in this way the uncertainties about real lesion composition.

We personally tried to contact the company that manufactures the phantom by email but was told that the material it is made of is private information and the same about the density value.

Contrast in radiographic or tomographic images is affected by the difference in X-ray attenuation between different structures or tissues in the image. X-ray attenuation depends on the composition of the material passed through (atomic number) and the density of the material (Section 2.1) [119].

If we had the densities of the different discs in the phantom available, we would have been able to draw more accurate conclusions regarding the comparison with the human body.

However, to overcome this problem, 3 different ROIs at different densities were selected in order to have a more complete view, at various densities and to try to replicate the more and less dense elements of the body.

2. The second limitation found is that a 2D acquisition mode to acquire the CBCT images of the phantom was used.

The system also uses the 3D mode, but it was not used (3D acquisition is more time consuming and in the frame of clinical measurements I had to optimize the time to perform measurements) because the purpose was to analyse the relative variation of the SDNR. However, it is expected that with 3D acquisition mode, the relative variation of the SDNR values is similar to the one obtained with 2D mode since the eventual use of image reconstruction algorithm could mainly influence the absolute values of SDNR.

However, for a future study one could try using the 3D acquisition mode to see the differences between 2D and 3D modes.

7.2 Limitations - Study II: Experimental Acquisition of CBCT Spectra

The knowledge of an X-ray spectra is an important task, both for imaging and dosimetry purposes. The use of real X-ray spectra could for example reduce a lot of the uncertainties in the absorbed dose estimations, however very often literature X-ray spectra are used.

To the best of our knowledge there are no comparable CBCT X-ray spectra measurements that can be used for comparison with our measurements. The Amptek CdTe detector is a very useful detector, mainly because it is a portable device and can be easily used in clinical setups in the diagnostic energy range. However, it is quite sensitive to the geometry setup, internal background noise, among others, and each minimal variation could reflect in a not complete spectra acquisition [120], [121]. The partial knowledge of the filter used to obtain the X-ray spectra could be also another aspect that can hinder the exact acquisition of the CBCT spectra. After several trials we obtained some reasonable spectra acquisition, that are well correlated with the increasing kV acquisition, however a further analysis and acquisition should be performed in order to understand the differences among acquired and literature CBCT spectra.:

Another important issue is to understand the variability of the different CBCT systems. For this work the linear accelerator Varian CLINAC DHX, equipped with the OBI Varian Medical Systems was used, but every machine is different and built differently.

Finally, there was also the chance to write to a team that had written a paper in which they had made the same acquisitions to ask what set-up and materials they had used, but no answer or reply was received [122].

7.3 Limitations – Study III: Dose assessment in pediatric CBCT

1. As a first limitation, it's important to notice that X-ray beams taken from the literature were used. Even if literature spectra are quite reliable, they do not reflect the eventual variability of each CBCT system. The use of experimental data could have permitted to lower the uncertainties due to spectrum estimation and consequently to increase the accuracy of the absorbed dose estimation.

   However, the actual beams should not differ much from those in the literature, as they were generated in precise laboratories or in previous studies, created using standardised X-ray sources or specific experimental equipment.

2. The second limitation concerns the X-ray beam irradiation setup. In section 4.3.4 it's explained how the various imaging protocols have an exposure area delimited by blades, which then filters the beam and makes it rectangular.

   The CBCT beam is conical with a circular cross-section but is filtered out by blocking part of it. In this study, that filter was not applied, but the conical beam irradiated directly, with a circular cross-section so as to circumscribe the rectangular cross-section. In this way, my beam irradiated slightly more part of the body, approximating the dose data obtained by excess.

   Surely in future studies this situation can be resolved by inserting, as in reality, a filter that blocks the X-rays beyond the selected section.

3. The last limitation concerns the choice of the isocenter point.

   In the last study 3 protocols, "Thorax", "Head & Neck" and "Pelvic" were analysed, and for each one an isocenter point was chosen.

   In the case of the 'Thorax' protocol for example, the isocenter was the lungs and calculated the dose to the surrounding organs from that position. However, the choice of the isocenter depends on the clinical task of each patient. So, if for example a patient has a suspicious mass near the heart, the CBCT isocenter beam will be at the heart.

It would therefore be useful and interesting to investigate this further by taking measurements by targeting each organ and analysing the absorbed dose in that organ as well as in adjacent organs, to have an overview of all possible treatment options.

Chapter 8

Conclusions

Cone Beam Computed Tomography is a medical imaging technique that has continued to evolve and improve over the past few years. In the current period, CBCT has reached a remarkable degree of technological maturity, with increasingly advanced and sophisticated imaging systems.

Modern CBCT devices are capable of capturing high-quality 3D images with a relatively low radiation dose. Another important current issue is its increasing application in guiding surgical interventions and treatment planning. This brings on one hand greater accuracy and safety in more complex operations, but on the other hand more frequent radiation exposure that accumulated over time can increase side effects.

Specifically in this work this work, the radiation dose distribution of CBCT scanning pediatric patients, was studied. Nowadays, there are different guidelines from country to country for radiation imaging. However, for CBCT there are still no specific guidelines to follow, so they do not distinguish whether the patient is an adult or a child and do not take into consideration physiognomic characteristics. Because of their small body size and incomplete body development (e.g., cellular replication time quite different from adults), children are more susceptible to ionizing radiation.

In this study, the aim was to understand whether it was possible to optimize the energy of X-ray exposure and the image quality parameter, with the intent to have the optimum image quality parameter with the lowest possible absorbed dose.

First, the goal was to verify if at 100 -120 kV, voltages used in clinical standard protocols provide a better SDNR or if it’s possible to lower the energy and still maintain a good image quality parameter.

50-60 kV CBCT images have a higher SDNR than at 100-120 kV ones. In this study were considered 3 ROI with different levels of contrast and on average it’s confirmed that the SDNR from 60 kV to 100 kV decreases of about 24,56%.

Having verified that it makes sense to analyse low energies for CBCT imaging, in the next study was analysed how the radiation dose might change depending on the energy level. Two 10- and 15-year-old female pediatric computational phantoms were used, and the radiation absorbed dose by the various organs following three different CBCT imaging protocols were calculated: Thorax, Head & Neck and Pelvic.

The results of this work indicate that voltages of 60 kV for the Thorax protocol would decrease the absorbed dose by 28.93%, for the Head & Neck protocol it would decrease by 39.02%, for the Pelvic protocol by 42.14%.

Several experimental studies would be required to confirm these results; however, it's important to remark that the results of this study could only be seen as an indication for the future optimization work in pediatric image guided/diagnostic imaging.

Also, the measurement of the X-ray spectra for a CBCT system could help to decrease the uncertainty on final absorbed dose estimation, since very often the literature spectra are used. In this work a tentative measurement was performed, and preliminary results indicate some significant differences with the literature spectra, indicating that more effort will be needed in order to make a good estimation of a CBCT X-ray system.

The ultimate goal is to ensure the highest quality of medical care while minimizing risks to patients as much as possible. This means continuing to improve diagnostic and therapeutic accuracy, while reducing exposure to ionizing radiation and other potential adverse effects,

Importantly, modern medicine is constantly evolving and constantly seeking to improve diagnostic and treatment modalities, taking into account scientific evidence and patient safety considerations. Findings from studies such as those conducted on pediatric CBCT provide valuable input to direct further research and develop optimized protocols.

Finally, it is important to highlight that for this Thesis work, several methodologies were used, namely statistical simulations, experimental measurements with radiation detectors and phantom image analysis. For this reason, this study suggests that the use of several approaches to problem solving could be inspiring and give several input idea for future studies.

Acknowledgments

My most honest and heartfelt thanks go to Prof. Gianni Coppa for accepting the task of supervisor for this thesis and for giving me the opportunity to have this experience in Portugal.

Gostaria também de estender o mesmo agradecimento, sentido e sincero, a Salvatore Di Maria, Ana Cravo Sá e Jorge Borbinha que, no papel de co-orientadores, ofereceram de imediato o seu profissionalismo e experiência na matéria. Muito obrigado por me acompanharem ao longo deste percurso e pela vossa permanente disponibilidade, estando sempre disponíveis para quaisquer esclarecimentos e pedidos. Um último agradecimento à Clínica de Radioncologia de Santarém e a Paulo Fernandes que me permitiu utilizar o melhor equipamento hospitalar disponível.

Finally, I would like to thank both for making me passionate during this scientific research and analysis, which has certainly contributed to expanding my knowledge in the biomedical field.

I would also like to thank my family for their support during this course of study I have undertaken, my fiancée for standing with me and supporting me, my close friends and all the people I met in Lisbon that I will never forget.

Bibliography

[1] L. A. Dawson and D. A. Jaffray, "Advances in image-guided radiation therapy," *Journal of Clinical Oncology*, vol. 25, no. 8. pp. 938–946, Mar. 10, 2007. doi: 10.1200/JCO.2006.09.9515.

[2] D. T. Ginat and R. Gupta, "Advances in computed tomography imaging technology," *Annual Review of Biomedical Engineering*, vol. 16. Annual Reviews Inc., pp. 431–453, 2014. doi: 10.1146/annurev-bioeng-121813-113601.

[3] K. Nakagawa *et al.*, "PII S0360-3016(97)00911-5 • Clinical Investigation HIGH-DOSE CONFORMAL RADIOTHERAPY INFLUENCED THE PATTERN OF FAILURE BUT DID NOT IMPROVE SURVIVAL IN GLIOBLASTOMA MULTIFORME," 1998.

[4] C. A. McBain *et al.*, "X-ray volumetric imaging in image-guided radiotherapy: The new standard in on-treatment imaging," *Int J Radiat Oncol Biol Phys*, vol. 64, no. 2, pp. 625–634, Feb. 2006, doi: 10.1016/j.ijrobp.2005.09.018.

[5] M. Oldham *et al.*, "Cone-beam-CT guided radiation therapy: A model for on-line application," *Radiotherapy and Oncology*, vol. 75, no. 3, pp. 271.E1-271.E8, 2005, doi: 10.1016/j.radonc.2005.03.026.

[6] A. Richter *et al.*, "Investigation of the usability of conebeam CT data sets for dose calculation," *Radiation Oncology*, vol. 3, no. 1, Dec. 2008, doi: 10.1186/1748-717X-3-42.

[7] N. Burridge *et al.*, "Online adaptive radiotherapy of the bladder: Small bowel irradiated-volume reduction," *Int J Radiat Oncol Biol Phys*, vol. 66, no. 3, pp. 892–897, Nov. 2006, doi: 10.1016/j.ijrobp.2006.07.013.

[8] R. L. Dixon and J. M. Boone, "Cone beam CT dosimetry: A unified and self-consistent approach including all scan modalities-With or without phantom motion," *Med Phys*, vol. 37, no. 6, pp. 2703–2718, 2010, doi: 10.1118/1.3395578.

[9] "OBI-IGRT MEDICAL CLINICAL SCHOOL https://it.scribd.com/document/528357912/OBI-IGRT-Clinical-School-Manual-ENG-Secured-1."

[10] M. J. Murphy *et al.*, "The management of imaging dose during image-guided radiotherapy: Report of the AAPM Task Group 75," *Medical Physics*, vol. 34, no. 10. John Wiley and Sons Ltd, pp. 4041–4063, 2007. doi: 10.1118/1.2775667.

[11] S. Korreman *et al.*, "The European Society of Therapeutic Radiology and Oncology-European Institute of Radiotherapy (ESTRO-EIR) report on 3D CT-based in-room image guidance systems: A practical and technical review and guide," *Radiotherapy and Oncology*, vol. 94, no. 2. Elsevier Ireland Ltd, pp. 129–144, 2010. doi: 10.1016/j.radonc.2010.01.004.

[12] T. C. Hsu, L. M. Cherry, and N. A. Samaan, "Differential Mutagen Susceptibility in Cultured Lymphocytes of Normal Individuals and Cancer Patients," 1985.

[13] Y. Zhang, Y. Yan, R. Nath, S. Bao, and J. Deng, "Personalized assessment of kV cone beam computed tomography doses in image-guided radiotherapy of pediatric cancer patients," *Int J Radiat Oncol Biol Phys*, vol. 83, no. 5, pp. 1649–1654, Aug. 2012, doi: 10.1016/j.ijrobp.2011.10.072.

[14] J. Deng, Z. Chen, K. B. Roberts, and R. Nath, "Kilovoltage imaging doses in the radiotherapy of pediatric cancer patients," *Int J Radiat Oncol Biol Phys*, vol. 82, no. 5, pp. 1680–1688, Apr. 2012, doi: 10.1016/j.ijrobp.2011.01.062.

[15] K. Son, J. S. Kim, H. Lee, and S. Cho, "Imaging dose of human organs from KV-CBCT in image-guided radiation therapy," *Radiat Prot Dosimetry*, vol. 175, no. 2, pp. 194–200, Jun. 2017, doi: 10.1093/rpd/ncw285.

[16] S. R. Alcorn *et al.*, "Practice patterns of photon and proton pediatric image guided radiation treatment: Results from an International Pediatric Research Consortium," *Pract Radiat Oncol*, vol. 4, no. 5, pp. 336–341, Sep. 2014, doi: 10.1016/j.prro.2014.03.014.

[17] C. ho Hua *et al.*, "Practice patterns and recommendations for pediatric image-guided radiotherapy: A Children's Oncology Group report," *Pediatr Blood Cancer*, vol. 67, no. 10, Oct. 2020, doi: 10.1002/pbc.28629.

[18] G. X. Ding and C. W. Coffey, “Radiation Dose From Kilovoltage Cone Beam Computed Tomography in an Image-Guided Radiotherapy Procedure,” *Int J Radiat Oncol Biol Phys*, vol. 73, no. 2, pp. 610–617, Feb. 2009, doi: 10.1016/j.ijrobp.2008.10.006.

[19] M. S. Pearce *et al.*, “Radiation exposure from CT scans in childhood and subsequent risk of leukaemia and brain tumours: A retrospective cohort study,” *The Lancet*, vol. 380, no. 9840, pp. 499–505, 2012, doi: 10.1016/S0140-6736(12)60815-0.

[20] L. Zhou, S. Bai, Y. Zhang, X. Ming, Y. Zhang, and J. Deng, “Imaging dose, cancer risk and cost analysis in image-guided radiotherapy of cancers,” *Sci Rep*, vol. 8, no. 1, Dec. 2018, doi: 10.1038/s41598-018-28431-9.

[21] S. Kim, T. T. Yoshizumi, D. P. Frush, G. Toncheva, and F. F. Yin, “Radiation dose from cone beam CT in a pediatric phantom: Risk estimation of cancer incidence,” *American Journal of Roentgenology*, vol. 194, no. 1, pp. 186–190, Jan. 2010, doi: 10.2214/AJR.08.2168.

[22] S. and C. of R. and C. C. and L. G. Royal College of Radiologists, “Good practice guide for paediatric radiotherapy, second edition,” 2018. [Online]. Available: www.rcr.ac.uk

[23] M. J. Goske *et al.*, “The ‘Image Gently’ campaign: Increasing CT radiation dose awareness through a national education and awareness program,” *Pediatric Radiology*, vol. 38, no. 3. pp. 265–269, Mar. 2008. doi: 10.1007/s00247-007-0743-3.

[24] K. J. Strauss *et al.*, “Image gently: Ten steps you can take to optimize image quality and lower CT dose for pediatric patients,” *American Journal of Roentgenology*, vol. 194, no. 4. pp. 868–873, Apr. 2010. doi: 10.2214/AJR.09.4091.

[25] P. Roxby *et al.*, “Simple methods to reduce patient dose in a Varian cone beam CT system for delivery verification in pelvic radiotherapy,” *British Journal of Radiology*, vol. 82, no. 982, pp. 855–859, Oct. 2009, doi: 10.1259/bjr/37579222.

[26] Cancer.net, “https://www.cancer.net/cancer-types/childhood-cancer/statistics,” *Cancer.net*.

[27] B. A. McDonald *et al.*, “Dose accumulation for MR-guided adaptive radiotherapy: From practical considerations to state-of-the-art clinical implementation,” *Frontiers in Oncology*, vol. 12. Frontiers Media S.A., Jan. 26, 2023. doi: 10.3389/fonc.2022.1086258.

[28] W. A. Kalender, “Kalender, W.A. (2011) Computed Tomography: Fundamentals, System Technology, Image Quality, Applications. John Wiley & Sons, Hoboken.,” 2011.

[29] D. J. Brenner, C. D. Elliston, E. J. Hall, and W. E. Berdon, “Estimated Risks of Radiation-Induced Fatal Cancer from Pediatric CT,” 2001. [Online]. Available: www.ajronline.org

[30] W. C. Scarfe and A. G. Farman, “What is Cone-Beam CT and How Does it Work?,” *Dental Clinics of North America*, vol. 52, no. 4. pp. 707–730, Oct. 2008. doi: 10.1016/j.cden.2008.05.005.

[31] V. Tsapaki, “Radiation dose optimization in diagnostic and interventional radiology: Current issues and future perspectives,” *Physica Medica*, vol. 79. Associazione Italiana di Fisica Medica, pp. 16–21, Nov. 01, 2020. doi: 10.1016/j.ejmp.2020.09.015.

[32] O. A. Catalano *et al.*, “clinical impact of PeT/Mr imaging in Patients with cancer Undergoing same-Day PeT/cT: Initial Experience in 134 Patients-A Hypothesis-generating Exploratory Study 1,” *Radiology*, vol. 269, doi: 10.1148/radiol.13131306/-/DC1.

[33] M. Dave, J. Davies, R. Wilson, and R. Palmer, “A comparison of cone beam computed tomography and conventional periapical radiography at detecting peri-implant bone defects,” *Clin Oral Implants Res*, vol. 24, no. 6, pp. 671–678, Jun. 2013, doi: 10.1111/j.1600-0501.2012.02473.x.

[34] L. Lechuga and G. A. Weidlich, “Cone Beam CT vs. Fan Beam CT: A Comparison of Image Quality and Dose Delivered Between Two Differing CT Imaging Modalities,” *Cureus*, Sep. 2016, doi: 10.7759/cureus.778.

[35] rxdental.it, “CT VS CBCT.” https://rxdental.it/differenze-sostanziali-tra-il-dentalscan-e-la-cbct/ (accessed Jul. 05, 2023).

[36] https://www.my-personaltrainer.it/, “ModerMedicalCThttps://www.my-personaltrainer.it/salute-benessere/tac-contrasto.html.” https://www.my-personaltrainer.it/salute-benessere/tac-contrasto.html (accessed Jul. 05, 2023).

[37] D. Maret *et al.*, “Effect of voxel size on the accuracy of 3D reconstructions with cone beam CT,” *Dentomaxillofacial Radiology*, vol. 41, no. 8, pp. 649–655, Dec. 2012, doi: 10.1259/dmf/81804525.

[38] A. A. Schegerer *et al.*, “Dose and Image Quality of Cone-Beam Computed Tomography as Compared With Conventional Multislice Computed Tomography in Abdominal Imaging,” 2014. [Online]. Available: www.investigativeradiology.com675

[39] C. Tomasetti, L. Li, and B. Vogelstein, “CANCER ETIOLOGY Stem cell divisions, somatic mutations, cancer etiology, and cancer prevention.” [Online]. Available: http://science.sciencemag.org/

[40] D. J. Brenner *et al.*, “Cancer risks attributable to low doses of ionizing radiation: Assessing what we really know,” 2003. [Online]. Available: www.pnas.orgcgidoi10.1073pnas.2235592100

[41] G. Chodick, K. P. Kim, M. Shwarz, G. Horev, V. Shalev, and E. Ron, “Radiation Risks from Pediatric Computed Tomography Scanning.”

[42] Icrp, “Annals of the ICRP Published on behalf of the International Commission on Radiological Protection.”

[43] D. J. Brenner, “Estimating cancer risks from pediatric CT: Going from the qualitative to the quantitative,” *Pediatr Radiol*, vol. 32, no. 4, pp. 228–231, 2002, doi: 10.1007/s00247-002-0671-1.

[44] “UNSCEAR 2013 Report Volume I.”

[45] L. Krille *et al.*, “Risk of cancer incidence before the age of 15 years after exposure to ionising radiation from computed tomography: results from a German cohort study,” *Radiat Environ Biophys*, vol. 54, no. 1, pp. 1–12, Mar. 2015, doi: 10.1007/s00411-014-0580-3.

[46] M. S. Pearce *et al.*, “Radiation exposure from CT scans in childhood and subsequent risk of leukaemia and brain tumours: A retrospective cohort study,” *The Lancet*, vol. 380, no. 9840, pp. 499–505, 2012, doi: 10.1016/S0140-6736(12)60815-0.

[47] J. D. Mathews *et al.*, “Cancer risk in 680 000 people exposed to computed tomography scans in childhood or adolescence: Data linkage study of 11 million Australians,” *BMJ (Online)*, vol. 346, no. 7910, Jun. 2013, doi: 10.1136/bmj.f2360.

[48] R. J.-L. , D. L. P. H. , L. C. , B. H. , C. J.-F. , C.-L. S. , L. D. and B. M.-O. Journy N., “Are the studies on cancer risk from CT scans biased by indication? Elements of answer from a large-scale cohort study in France.”.

[49] H. B. Harvey, J. A. Brink, and D. P. Frush, “Informed consent for radiation risk from CT is unjustified based on the current scientific evidence,” *Radiology*, vol. 275, no. 2. Radiological Society of North America Inc., pp. 321–325, May 01, 2015. doi: 10.1148/radiol.2015142859.

[50] J. D. Boice, “Radiation epidemiology and recent paediatric computed tomography studies,” 2015.

[51] Iaea, “GC(57)/3 - IAEA Annual Report 2012,” 2012.

[52] European Commission 2018, “European Commission (2018) European guidelines on diagnostic reference levels for paediatric imaging. Radiation Protection 185. http://www.eurosafeimaging.org/wp/wp-content/uploads/2018/09/ rp_185.pdf. Accessed 2 December 2018”.

[53] Europen Commission (1999), “European Commission (1999) Guidance on diagnostic reference levels (DRLS) for medical exposures. Radiation Protection 109. https://ec.europa.eu/energy/sites/ener/files/documents/109_en.pdf. Accessed 2 December 2018”.

[54] L. F. Donnelly *et al.*, “Minimizing Radiation Dose for Pediatric Body Applications of Single-Detector Helical CT: Strategies at a Large Children’s Hospital.” [Online]. Available: www.ajronline.org

[55] A. Paterson, D. P. Frush, and L. F. Donnelly, “Helical CT of the Body: Are Settings Adjusted for Pediatric Patients? H,” 2001. [Online]. Available: www.ajronline.org

[56] the E. P. and the E. E. and S. C. Commission to the Council, “4 final COMMISSION STAFF WORKING DOCUMENT Accompanying the document Report from the Commission to the Council, the European Parliament and the European Economic and Social Committee on the implementation by the Member States of Council Directive 2006/117/EURATOM on the supervision and control of shipments of radioactive waste and spent fuel Second Report {COM(2018) 6 final}”, doi: 10.2760/25402.

[57] “DDM2 Project Report Part 2: Diagnostic Reference Levels (DRL) in Europe Study on European Population Doses from Medical Exposure (Dose Datamed 2, DDM2) DDM2 Project Report Part 2: Diagnostic Reference Levels (DRLs) in Europe.”

[58] H. O. Elford Johns and Ds. John Robert Cunningham, “THE PHYSICS OF RADIOLOGY FOURTH EDITION.”
[59] S. Naeem Ahmed, “Physics and Engineering of Radiation Detection.”
[60] U. di T. Franco Dalfovo Dipartimento di Fisica, “La fisica dei quanti da Planck a Schrödinger.”
[61] R. Di Capua, F. Offi, and F. Fontana, “Check the Lambert-Beer-Bouguer law: A simple trick to boost the confidence of students toward both exponential laws and the discrete approach to experimental physics,” *Eur J Phys*, vol. 35, no. 4, Jul. 2014, doi: 10.1088/0143-0807/35/4/045025.
[62] I. Rosenberg, “Radiation Oncology Physics: A Handbook for Teachers and Students,” *Br J Cancer*, vol. 98, no. 5, pp. 1020–1020, Mar. 2008, doi: 10.1038/sj.bjc.6604224.
[63] O. Daniel, G. Ogbanje, and S. A. Jonah, “X-Rays and Scattering from Filters Used in Diagnostic Radiology,” 2013. [Online]. Available: www.ijsrp.org
[64] F. M. Khan, *The physics of radiation therapy*. Lippincott Williams & Wilkins, 2003.
[65] J. E. Parks and J. E. Parks, “The Compton Effect-Compton Scattering and Gamma Ray Spectroscopy.”
[66] N. Tomic, S. Devic, F. Deblois, and J. Seuntjens, “Reference radiochromic film dosimetry in kilovoltage photon beams during CBCT image acquisition,” *Med Phys*, vol. 37, no. 3, pp. 1083–1092, 2010, doi: 10.1118/1.3302140.
[67] 2007 INTERNATIONAL ATOMIC ENERGY AGENCY VIENNA, “DOSIMETRY IN DIAGNOSTIC RADIOLOGY: AN INTERNATIONAL CODE OF PRACTICE.”
[68] E.B. Podgorsak, “Radiation Physics for Medical Physicists”.
[69] F. HERBERT ATTlX, W. WILEY-VCH Verlag GmbH, and C. KGaA, “INTRODUCTION TO RADIOLOGICAL PHYSICS AND RADIATION DOSIMETRY.”
[70] “Status of Computed Tomography Dosimetry for Wide Cone Beam Scanners,” [Online]. Available: http://www.iaea.org/Publications/index.html
[71] Diagnostic Imaging Council CT Committee, “The Measurement, Reporting, and Management of Radiation Dose in CT”.
[72] X. Li, D. Zhang, and B. Liu, “A practical approach to estimate the weighted CT dose index over an infinite integration length,” *Phys Med Biol*, vol. 56, no. 18, pp. 5789–5803, Sep. 2011, doi: 10.1088/0031-9155/56/18/002.
[73] C. Anam, F. Haryanto, R. Widita, I. Arif, G. Dougherty, and D. McLean, “Volume computed tomography dose index (CTDIvol) and size-specific dose estimate (SSDE) for tube current modulation (TCM) in CT scanning,” *International Journal of Radiation Research*, vol. 16, no. 3, pp. 289–297, Jul. 2018, doi: 10.18869/acadpub.ijrr.16.2.289.
[74] I. A. Tsalafoutas and S. I. Metallidis, “A method for calculating the dose length product from CT DICOM images,” *British Journal of Radiology*, vol. 84, no. 999, pp. 236–243, Mar. 2011, doi: 10.1259/bjr/37630380.
[75] F. Noo, J. Pack, and D. Heuscher, “Exact helical reconstruction using native cone-beam geometries INSTITUTE OF PHYSICS PUBLISHING PHYSICS IN MEDICINE Exact helical reconstruction using native cone-beam geometries,” 2003. [Online]. Available: http://iopscience.iop.org/0031-9155/48/23/001
[76] “https://leedstestobjects.com/index.php/phantom/tor-18fg/.”
[77] A. M. Mendrik, E. J. Vonken, A. Rutten, M. A. Viergever, and B. Van Ginneken, “Noise reduction in computed tomography scans using 3-D anisotropic hybrid diffusion with continuous switch,” *IEEE Trans Med Imaging*, vol. 28, no. 10, pp. 1585–1594, Oct. 2009, doi: 10.1109/TMI.2009.2022368.
[78] “TOR 18FG X-ray Phantoms user manual Leeds Test Objects.” [Online]. Available: www.leedstestobjects.com
[79] “https://www.oncologysystems.com/inventory/medical-equipment-for-sale/used-linear-accelerators/varian-dhx-linear-accelerator.”
[80] S. Yoo *et al.*, “A quality assurance program for the on-board imager®,” *Med Phys*, vol. 33, no. 11, pp. 4431–4447, 2006, doi: 10.1118/1.2362872.
[81] A. Maldera, P. De Marco, P. E. Colombo, D. Origgi, and A. Torresin, “Digital breast tomosynthesis: Dose and image quality assessment,” *Physica Medica*, vol. 33, pp. 56–67, Jan. 2017, doi: 10.1016/j.ejmp.2016.12.004.

[82] C. A. Schneider, W. S. Rasband, and K. W. Eliceiri, “NIH Image to ImageJ: 25 years of image analysis,” *Nature Methods*, vol. 9, no. 7. pp. 671–675, Jul. 2012. doi: 10.1038/nmeth.2089.
[83] “https://www.amptek.com/internal-products/xr-100cdte-x-ray-and-gamma-ray-detector.”
[84] T. Takahashi *et al.*, “High resolution CdTe detector and applications to imaging devices,” in *IEEE Nuclear Science Symposium and Medical Imaging Conference*, 2000. doi: 10.1109/nssmic.2000.949043.
[85] “https://www.amptek.com/software/dp5-digital-pulse-processor-software/dppmca-display-acquisition-software.”
[86] C. Alaoui, “Peltier Thermoelectric Modules Modeling and Evaluation Electric Vehicle Energy Management View project Advanced FPGA applications View project Peltier Thermoelectric Modules Modeling and Evaluation,” 2011. [Online]. Available: https://www.researchgate.net/publication/228865590
[87] C. Ponchut *et al.*, “Evaluation of a photon-counting hybrid pixel detector array with a synchrotron X-ray source,” 2002. [Online]. Available: http://www.cern.ch/MEDIPIX/
[88] E. Guni *et al.*, “The influence of pixel pitch and electrode pad size on the spectroscopic performance of a photon counting pixel detector with CdTe sensor,” *IEEE Trans Nucl Sci*, vol. 58, no. 1 PART 1, pp. 17–25, Feb. 2011, doi: 10.1109/TNS.2010.2095883.
[89] S. Van Loo, E. Keto, and Q. Zhang, “Core and filament formation in magnetized, self-gravitating isothermal layers,” *Astrophysical Journal*, vol. 789, no. 1, Jul. 2014, doi: 10.1088/0004-637X/789/1/37.
[90] R. Ballabriga *et al.*, “Characterization of the Medipix3 pixel readout chip,” in *Journal of Instrumentation*, Jan. 2011. doi: 10.1088/1748-0221/6/01/C01052.
[91] J. P. Ronaldson *et al.*, “Characterization of Medipix3 with the MARS readout and software,” in *Journal of Instrumentation*, Jan. 2011. doi: 10.1088/1748-0221/6/01/C01056.
[92] M.-M. Bé, V. Chisté, C. Dulieu, and Bureau International des Poids et Mesures., *Table of radionuclides. Vol. 3, A = 3 to 244*. Bureau International des Poids et Mesures, 2006.
[93] D. Demir, P. Önder, and T. Öznülüer, “Performance of CdTe detector in the 13-1333keV energy range,” *Radiation Physics and Chemistry*, vol. 79, no. 11, pp. 1132–1136, Nov. 2010, doi: 10.1016/j.radphyschem.2010.06.001.
[94] J. Ródenas, S. Gallardo, and J. Ortiz, “Comparison of a laboratory spectrum of Eu-152 with results of simulation using the MCNP code,” *Nucl Instrum Methods Phys Res A*, vol. 580, no. 1 SPEC. ISS., pp. 303–305, Sep. 2007, doi: 10.1016/j.nima.2007.05.162.
[95] “Confidential information taken from the clinical CBCT Varian manual.”
[96] Y. J. Lee, H. J. Ryu, H. M. Cho, S. W. Lee, Y. N. Choi, and H. J. Kim, “Optimization of an ultra-high-resolution parallel-hole collimator for CdTe semiconductor SPECT system,” in *Journal of Instrumentation*, Jan. 2013. doi: 10.1088/1748-0221/8/01/C01044.
[97] Siemens, “https://bps.healthcare.siemens-healthineers.com/booneweb/index.html.”
[98] J. S. Lee, D. G. Kang, S. O. Jin, I. Kim, and S. Y. Lee, “Energy calibration of a CdTe photon counting spectral detector with consideration of its non-convergent behavior,” *Sensors (Switzerland)*, vol. 16, no. 4, Apr. 2016, doi: 10.3390/s16040518.
[99] OriginLab, “https://www.originlab.com/”.
[100] WILEY, “Linear Regression Analysis”.
[101] J. R. and C. de Boor, “A Practical Guide to Splines.,” *Math Comput*, vol. 34, no. 149, p. 325, Jan. 1980, doi: 10.2307/2006241.
[102] “‘Il piano cartesiano e la retta’ Mappe, esercizi, approfondimenti.”
[103] A. Di Matteo *et al.*, “Evolutionary power spectral density estimation using energy spectrum equation Simulation of Non-Stationary stochastic process View project Evolutionary Spectra Estimation View project Evolutionary power spectral density estimation using energy spectrum equation.” [Online]. Available: https://www.researchgate.net/publication/363762766
[104] M. Nascimento and J. Peixoto, “Monte Carlo method and their codes applied to ionizing radiation,” in *Journal of Physics: Conference Series*, IOP Publishing Ltd, Apr. 2021. doi: 10.1088/1742-6596/1826/1/012049.
[105] T. Wagener, M. Lees, M. J. Lees, and H. S. Wheater, “Monte-Carlo Analysis Toolbox User Manual Adding the human dimension to drought View project Development and Use of Global Teleconnection

Operators (GTOs) View project MONTE-CARLO ANALYSIS TOOLBOX USER MANUAL." [Online]. Available: https://www.researchgate.net/publication/267818673

[106] I. Sechopoulos *et al.*, "Monte Carlo reference data sets for imaging research: Executive summary of the report of AAPM Research Committee Task Group 195," *Med Phys*, vol. 42, no. 10, Oct. 2015, doi: 10.1118/1.4928676.

[107] H. Moughli, A. Belghachi, A. Bouida, A. Hasni, and L. Varani, "The Monte Carlo Simulation Coupled with Poisson Equation Applied to the Study of a Diode base of Hg0.8Cd0.2Te The Monte Carlo Simulation Coupled with Poisson Equation Applied to the Study of a Diode base of Hg0 The Monte Carlo Simulation Coupled With Poisson Equation Applied to the study of a Diode base of Hg 0.8 Cd 0.2 Te," vol. 36, pp. 50–56, 2013, doi: 10.1016/j.egypro.2013.07.007ï.

[108] A. F. Bielajew, "Fundamentals of the Monte Carlo method for neutral and charged particle transport," 2001.

[109] OECD Nuclear Energy Agency., *PENELOPE : a code system for Monte Carlo simulation of electron and photon transport : workshop proceedings, Issy-les-Moulineaux, France, 7-10 July 2003.* Nuclear Energy Agency, Organisation for Economic Co-operation and Development, 2003.

[110] W. R. Nelson and Y. Namitot, "THE EGS4 CODE SYSTEM: SOLUTION OF GAMMA-RAY AND ELECTRON TRANSPORT PROBLEMS*."

[111] J. Sempau, "PENELOPE/penEasy User Manual," 2003. [Online]. Available: https://rsicc.ornl.gov

[112] M. G. W. E. E. C. M. R. J. C. E. K. F. [1]; D. J. L. [2]; M. D. [3]; G. M. K. [4] Stabin, "Mathematical models and specific absorbed fractions of photon energy in the nonpregnant adult female and at the end of each trimester of pregnancy".

[113] "https://www.icrp.org/."

[114] International Commission on Radiological Protection. and International Commission on Radiation Units and Measurements., *Adult reference computational phantoms : joint ICRP/ICRU report*. Polestar Wheatons Ltd, 2009.

[115] C. H. Clement, H. Fujita, W. E. Bolch, and International Commission on Radiological Protection., *Paediatric reference computational phantoms*.

[116] L. A. Chang, S. L. Simon, T. J. Jorgensen, D. A. Schauer, and C. Lee, "Dose coefficients for ICRP reference pediatric phantoms exposed to idealised external gamma fields," *Journal of Radiological Protection*, vol. 37, no. 1, pp. 127–144, Mar. 2017, doi: 10.1088/1361-6498/aa559e.

[117] "Best Practice Pathway for Pelvic Radiation Disease Lead Partner."

[118] A. Webster, A. L. Appelt, and G. Eminowicz, "Image-Guided Radiotherapy for Pelvic Cancers: A Review of Current Evidence and Clinical Utilisation," *Clin Oncol*, vol. 32, no. 12, pp. 805–816, Dec. 2020, doi: 10.1016/j.clon.2020.09.010.

[119] B. Saritha and A. S. Nageswara Rao, "A study on photon attenuation coefficients of different wood materials with different densities," in *Journal of Physics: Conference Series*, Institute of Physics Publishing, Dec. 2015. doi: 10.1088/1742-6596/662/1/012030.

[120] T. Takahashi and S. Watanabe, "Recent Progress in CdTe and CdZnTe Detectors."

[121] T. Takahashi and S. Watanabe, "Recent progress in CdTe and CdZnTe detectors," in *IEEE Transactions on Nuclear Science*, Aug. 2001, pp. 950–959. doi: 10.1109/23.958705.

[122] A. Maldera, P. De Marco, P. E. Colombo, D. Origgi, and A. Torresin, "Digital breast tomosynthesis: Dose and image quality assessment," *Physica Medica*, vol. 33, pp. 56–67, Jan. 2017, doi: 10.1016/j.ejmp.2016.12.004.

[123] L. Abbene and S. Del Sordo, "CdTe Detectors," in *Comprehensive Biomedical Physics*, Elsevier, 2014, pp. 285–314. doi: 10.1016/B978-0-444-53632-7.00619-5.

Appendix

Appendix I

```
# >>>> SIMULATION CONFIG FILE FOR penEasy >>>>>>>>>>>>>>>>>>>>>>>>>>>>
#
#   Case description:
#   Phantom 15 years old Female, 40 kV beam, thorax protocol pointed in the middle of
the  #   lungs.
#
# Last update:
#   2019-09-21 by JS


# >>>> GENERAL INSTRUCTIONS >>>>>>>>>>>>>>>>>>>>>>>>>>>>>>>>>>>>>>>>>>>>
#
# * Lines starting with a '#' (in column 1) and blank lines are
#   comments. Comments are NOT allowed inside data sections.
#
# * Do not change the order in which sections appear, neither the order
#   of data fields in each section.
#
# * Each data section has a version number of the form yyyy-mm-dd that is
#   written in the corresponding section title. Should an incorrect
#   version be introduced an error message would be issued and the
#   execution halted.
#
# * Character strings (e.g. file names) are introduced in free-format
#   style, that is, leading and trailing blanks are allowed. Their
#   maximum extension (except when noted) is 80 characters and they must
#   not contain blanks. Thus, for instance, 'stainless steel' should be
#   introduced as 'stainlessSteel' or 'stainless_Steel'.
#
# * Most syntax errors can be easily identified by looking for error
#   messages or inconsistencies within the last lines of penEasy output.
#   It is advisable to check the output to make sure that the
#   information written after processing each section coincides with what
#   is expected from the input.


# >>>> GENERAL >>>>>>>>>>>>>>>>>>>>>>>>>>>>>>>>>>>>>>>>>>>>>>>>>>>>>>>>>>

[SECTION CONFIG v.2013-03-18]
1.0e10              NUMBER OF HISTORIES (1.0e15 MAX)
1.0e30              ALLOTTED TIME (s) (+ FOR REAL TIME, - FOR CPU TIME)
60.0                UPDATE INTERVAL (s)
1  1                INITIAL RANDOM SEEDS
-                   SEEDS FILE; MUST ENTER SEEDS=0,0 TO APPLY
-                   RESTART FILE; MUST ENTER SEEDS=-1,-1 TO APPLY
penEasy.dmp         OUTPUT DUMP FILE; ENTER '-' FOR 'NO DUMP'
2000.0              INTERVAL BETWEEN DUMPS (s)
```

```
[END OF CONFIG SECTION]


# >>>> SOURCES >>>>>>>>>>>>>>>>>>>>>>>>>>>>>>>>>>>>>>>>>>>>>>>>>>>>>>>>>>>>>>>>

[SECTION SOURCE BOX ISOTROPIC GAUSS SPECTRUM v.2014-12-21]

ON                      STATUS (ON or OFF)
2                       PARTICLE TYPE (1=ELECTRON, 2=PHOTON, 3=POSITRON) OR
RADIONUCLIDE FILENAME (e.g., Co-60.nuc)

SUBSECTION FOR PHOTON POLARIZATION:
 0                      ACTIVATE PHOTON POLARIZATION PHYSICS (0=NO, 1=YES)
 0.0 0.0 0.0            STOKES PARAMETERS (USED ONLY IF ACTIVATE
POLARIZATION=1)

SUBSECTION FOR PARTICLE POSITION:
24.36 -100 124.99       COORDINATES (cm) OF BOX CENTER
0.0  0.0  0.0           BOX SIDES (cm)
0.0  0.0                FWHMs (cm) OF GAUSSIAN X,Y DISTRIBUTIONS
0.0  0.0  0.0           EULER ANGLES [OMEGA,THETA,PHI](deg) FOR BOX
ROTATION Rz(PHI).Ry(THETA).Rz(OMEGA).r
0.0  0.0  0.0           TRANSLATION [DX,DY,DZ](cm) OF BOX CENTER POSITION
0                       SOURCE MATERIAL (0=DON'T CARE, >0 FOR LOCAL
SOURCE, <0 FOR IN-FIELD BEAM)

SUBSECTION FOR PARTICLE DIRECTION:
0.0  1.0  0.0           DIRECTION VECTOR; NO NEED TO NORMALIZE
0.0 4.97                DIRECTION POLAR ANGLE INTERVAL [THETA0,THETA1],
BOTH VALUES IN [0,180]deg
0.0 360.0               DIRECTION AZIMUTHAL ANGLE INTERVAL PHI0 IN [0,360)deg
AND DeltaPHI IN [0,360]deg
1                       APPLY ALSO TO DIRECTION THE ROTATION USED FOR BOX
POSITION (0=NO, 1=YES)

SUBSECTION FOR PARTICLE ENERGY:  (REMOVE THIS SUBSECTION IF
RADIONUCLIDE IS USED AS PARTICLE TYPE)
40kVLITSPECTRUM.dat     ENERGY SPECTRUM FILE NAME
0.0                     FWHM(eV) OF GAUSSIAN
[END OF BIGS SECTION]
FWHM(eV) OF GAUSSIAN ENERGY DISTRIB. [NOTE FWHM=SIGMA*sqrt(8*ln(2))]

[SECTION SOURCE PHASE SPACE FILE v.2009-06-15]
OFF                     STATUS (ON or OFF)
0                       PSF FORMAT (0=STANDARD penEasy ASCII, 1=IAEA BINARY)
particles.psf           PSF FILENAME, REMOVE EXTENSION IF PSF FORMAT=1
1                       SPLITTING FACTOR
0.0  0.0  0.0           EULER ANGLES [Rz,Ry,Rz](deg) TO ROTATE POSITION AND
DIRECTION
0.0  0.0  0.0           TRANSLATION [DX,DY,DZ](cm) OF POSITION
1                       VALIDATE BEFORE SIMULATION (1=YES, MAY TAKE A
WHILE; 0=NO)
```

```
0.000e0                    MAX PSF ENERGY (eV) (UNUSED IF VALIDATE=1 OR IAEA
FORMAT. ADD 1023 keV FOR e+)
[END OF SPSF SECTION]


# >>>> PENGEOM+PENVOX >>>>>>>>>>>>>>>>>>>>>>>>>>>>>>>>>>>>>>>>>>>>>>>>>>>>>>>

[SECTION PENGEOM+PENVOX v.2009-06-15]
15f_geometry.geo          QUADRICS FILE NAME, USE '-' IF NONE
15F_ICRP143_ref.vox       VOXELS FILE NAME, USE '-' IF NONE
58                        TRANSPARENT QUADRIC MAT (USED ONLY IF QUAD&VOX)
10                        GRANULARITY TO SCAN VOXELS (USED ONLY IF
QUAD&VOX)
[END OF GEO SECTION]


# >>>> TRANSPORT PARAMETERS >>>>>>>>>>>>>>>>>>>>>>>>>>>>>>>>>>>>>>>>>>>>>>>>
#
# * Write one line of data per defined material. Each line starts with
#   the material index (MAT#), which should be an integer starting from 1.
#   Set MAT to -1 in the last line to indicate the end of the list.
#
# * Use 20 characters at most to introduce the material data file name.
#   Blanks or special characters are not allowed in file names. Thus,
#   instead of "stainless steel.mat" use "stainlessSteel.mat".
#
# * If, for a certain material, the transport parameters after the file
#   name are left empty, then they are set automatically. See the User
#   Manual for details.

[SECTION PENELOPE v.2019-08-06]
MAT# FILE___(max 20 char) EABS(e-)  EABS(ph)  EABS(e+)
C1   C2   WCC  WCR  DSMAX    COMMENTS
  1   m/Teeth.m               1e4      1e3      1e4      0.1  0.1  1e4  1e3  9.90e-2
  2   m/Mineralbone.m         1e4      1e3      1e4      0.1  0.1  1e4  1e3  9.90e-2
  3   m/Hum_up_ha_sp.m        1e4      1e3      1e4      0.1  0.1  1e4  1e3  9.90e-2
  4   m/Hum_lw_ha_sp.m        1e4      1e3      1e4      0.1  0.1  1e4  1e3  9.90e-2
  5   m/Ulnae_rad_sp.m        1e4      1e3      1e4      0.1  0.1  1e4  1e3  9.90e-2
  6   m/Wrist_hand_sp.m       1e4      1e3      1e4      0.1  0.1  1e4  1e3  9.90e-2
  7   m/Clavicles.m           1e4      1e3      1e4      0.1  0.1  1e4  1e3  9.90e-2
  8   m/Cranium.m             1e4      1e3      1e4      0.1  0.1  1e4  1e3  9.90e-2
  9   m/Femora_up,sp.m        1e4      1e3      1e4      0.1  0.1  1e4  1e3  9.90e-2
  10  m/Femora_lw,sp.m        1e4      1e3      1e4      0.1  0.1  1e4  1e3  9.90e-2
  11  m/Legbones.m            1e4      1e3      1e4      0.1  0.1  1e4  1e3  9.90e-2
  12  m/Foot,sp.m             1e4      1e3      1e4      0.1  0.1  1e4  1e3  9.90e-2
  13  m/Mandible,sp.m         1e4      1e3      1e4      0.1  0.1  1e4  1e3  9.90e-2
  14  m/Pelvis,sp.m           1e4      1e3      1e4      0.1  0.1  1e4  1e3  9.90e-2
  15  m/Ribs,sp.m             1e4      1e3      1e4      0.1  0.1  1e4  1e3  9.90e-2
  16  m/Scapulae,sp.m         1e4      1e3      1e4      0.1  0.1  1e4  1e3  9.90e-2
  17  m/Cervical,sp.m         1e4      1e3      1e4      0.1  0.1  1e4  1e3  9.90e-2
  18  m/Thoracic,sp.m         1e4      1e3      1e4      0.1  0.1  1e4  1e3  9.90e-2
  19  m/Lumbar,sp.m           1e4      1e3      1e4      0.1  0.1  1e4  1e3  9.90e-2
  20  m/Sacrum,sp.m           1e4      1e3      1e4      0.1  0.1  1e4  1e3  9.90e-2
  21  m/Sternum,sp.m          1e4      1e3      1e4      0.1  0.1  1e4  1e3  9.90e-2
```

```
 22  m/Humfem_up_mc.m    1e4      1e3      1e4      0.1  0.1  1e4  1e3  9.90e-2
 23  m/Humfem_lw_mc.m    1e4      1e3      1e4      0.1  0.1  1e4  1e3  9.90e-2
 24  m/Ulnae_rad_mc.m    1e4      1e3      1e4      0.1  0.1  1e4  1e3  9.90e-2
 25  m/Legbones_mc.m     1e4      1e3      1e4      0.1  0.1  1e4  1e3  9.90e-2
 26  m/Cartilage.m       1e4      1e3      1e4      0.1  0.1  1e4  1e3  9.90e-2
 27  m/Skin.m            1e4      1e3      1e4      0.1  0.1  1e4  1e3  9.90e-2
 28  m/Blood.m           1e4      1e3      1e4      0.1  0.1  1e4  1e3  9.90e-2
 29  m/Oral_muc.m        1e4      1e3      1e4      0.1  0.1  1e4  1e3  9.90e-2
 30  m/Liver.m           1e4      1e3      1e4      0.1  0.1  1e4  1e3  9.90e-2
 31  m/Pancreas.m        1e4      1e3      1e4      0.1  0.1  1e4  1e3  9.90e-2
 32  m/Brain.m           1e4      1e3      1e4      0.1  0.1  1e4  1e3  9.90e-2
 33  m/Heart_wall.m      1e4      1e3      1e4      0.1  0.1  1e4  1e3  9.90e-2
 34  m/Eyes.m            1e4      1e3      1e4      0.1  0.1  1e4  1e3  9.90e-2
 35  m/Kidney.m          1e4      1e3      1e4      0.1  0.1  1e4  1e3  9.90e-2
 36  m/Stomach_wall.m    1e4      1e3      1e4      0.1  0.1  1e4  1e3  9.90e-2
 37  m/S_intestine_w.m   1e4      1e3      1e4      0.1  0.1  1e4  1e3  9.90e-2
 38  m/Colonrectum_w.m   1e4      1e3      1e4      0.1  0.1  1e4  1e3  9.90e-2
 39  m/Spleen.m          1e4      1e3      1e4      0.1  0.1  1e4  1e3  9.90e-2
 40  m/Thyroid.m         1e4      1e3      1e4      0.1  0.1  1e4  1e3  9.90e-2
 41  m/Bladder_w.m       1e4      1e3      1e4      0.1  0.1  1e4  1e3  9.90e-2
 42  m/Ovaries.m         1e4      1e3      1e4      0.1  0.1  1e4  1e3  9.90e-2
 43  m/Adrenalglands.m   1e4      1e3      1e4      0.1  0.1  1e4  1e3  9.90e-2
 44  m/Oesophagus.m      1e4      1e3      1e4      0.1  0.1  1e4  1e3  9.90e-2
 45  m/Softtissue.m      1e4      1e3      1e4      0.1  0.1  1e4  1e3  9.90e-2
 46  m/Uterus.m          1e4      1e3      1e4      0.1  0.1  1e4  1e3  9.90e-2
 47  m/Lymphnodes.m      1e4      1e3      1e4      0.1  0.1  1e4  1e3  9.90e-2
 48  m/Breast.m          1e4      1e3      1e4      0.1  0.1  1e4  1e3  9.90e-2
 49  m/Adiposetissue.m   1e4      1e3      1e4      0.1  0.1  1e4  1e3  9.90e-2
 50  m/Lung.m            1e4      1e3      1e4      0.1  0.1  1e4  1e3  9.90e-2
 51  m/Stomach_cont.m    1e4      1e3      1e4      0.1  0.1  1e4  1e3  9.90e-2
 52  m/S_intest_cont.m   1e4      1e3      1e4      0.1  0.1  1e4  1e3  9.90e-2
 53  m/Rcolon_cont.m     1e4      1e3      1e4      0.1  0.1  1e4  1e3  9.90e-2
 54  m/Lcolon_cont.m     1e4      1e3      1e4      0.1  0.1  1e4  1e3  9.90e-2
 55  m/Sigmoid_cont.m    1e4      1e3      1e4      0.1  0.1  1e4  1e3  9.90e-2
 56  m/Urine.m           1e4      1e3      1e4      0.1  0.1  1e4  1e3  9.90e-2
 57  m/Air_in.m          1e4      1e3      1e4      0.1  0.1  1e4  1e3  9.90e-2
 58  m/Air_out.m         1e4      1e3      1e4      0.1  0.1  1e4  1e3  9.90e-2
 -1 (SET MAT=-1 TO END THE LIST)
[END OF PEN SECTION]


# >>>> TALLIES >>>>>>>>>>>>>>>>>>>>>>>>>>>>>>>>>>>>>>>>>>>>>>>>>>>>>>>>>>>>

[SECTION TALLY VOXEL DOSE v.2014-12-27]
 OFF                    STATUS (ON or OFF)
200  210                ROI X-INDEX MIN,MAX (0 0 FOR ALL VOXELS)
128  130                ROI Y-INDEX MIN,MAX (0 0 FOR ALL VOXELS)
500  510                ROI Z-INDEX MIN,MAX (0 0 FOR ALL VOXELS)
 1                      PRINT VOXELS MASS IN REPORT (1=YES,0=NO)
 1                      PRINT COORDINATES IN REPORT (1=YES,0=NO,-
1=NO&BINARYFORMAT)
 0.0                    RELATIVE UNCERTAINTY (%) REQUESTED
[END OF VDD SECTION]
```

```
[SECTION TALLY SPATIAL DOSE DISTRIB v.2009-06-15]
STATUS (ON or OFF)
 OFF
 100.0  300.0   20              XMIN,XMAX(cm),NXBIN (0 FOR DX=infty)
 0.0  0.0   0                   YMIN,YMAX(cm),NYBIN (0 FOR DY=infty)
 100.0  1300.0   20             ZMIN,ZMAX(cm),NZBIN (0 FOR DZ=infty)
 1                              PRINT COORDINATES IN REPORT (1=YES,0=NO,-
1=NO&BINARYFORMAT)
 1.0                            RELATIVE UNCERTAINTY (%) REQUESTED
[END OF SDD SECTION]

[SECTION TALLY CYLINDRICAL DOSE DISTRIB v.2009-06-15]
 OFF                            STATUS (ON or OFF)
 0.0  8.0  80                   RMIN,RMAX(cm),NRBIN (>0)
 0.0  7.0  40                   ZMIN,ZMAX(cm),NZBIN (0 FOR DZ=infty)
 1                              PRINT COORDINATES IN REPORT (1=YES,0=NO)
 0.0                            RELATIVE UNCERTAINTY (%) REQUESTED
[END OF CDD SECTION]

[SECTION TALLY SPHERICAL DOSE DISTRIB v.2009-06-15]
 OFF                            STATUS (ON or OFF)
 0.0  1.0  50                   RMIN,RMAX(cm),NRBIN (>0)
 1                              PRINT COORDINATES IN REPORT (1=YES,0=NO)
 0.0                            RELATIVE UNCERTAINTY (%) REQUESTED
[END OF SPD SECTION]

[SECTION TALLY ENERGY DEPOSITION v.2012-06-01]
 ON                             STATUS (ON or OFF)
 51                             DETECTION MATERIAL
 0.00                           RELATIVE UNCERTAINTY (%) REQUESTED
[END OF EDP SECTION]

[SECTION TALLY PULSE HEIGHT SPECTRUM v.2012-06-01]
 OFF                            STATUS (ON or OFF)
 1                              DETECTION MATERIAL
 0.0  1.0e9  100                EMIN,EMAX(eV), No. OF E BINS
 0.0  0.0                       A(eV^2),B(eV) FOR GAUSSIAN CONVOLUTION
FWHM[eV]=sqrt(A+B*E[eV])
 0.0                            RELATIVE UNCERTAINTY (%) REQUESTED
[END OF PHS SECTION]

[SECTION TALLY PIXELATED IMAGING DETECTOR v.2016-07-04]
 OFF                            STATUS (ON or OFF)
 1                              DETECTION MATERIAL
 0                              FILTER PHOTON INTERACTION (0=NOFILTER, -
1=UNSCATTERED, 1=RAYLEIGH, 2=COMPTON, 3=SECONDARIES,
9=MULTISCATTERED)
 0   100                        X-PIXEL SIZE(cm), No. X-PIXELS (ENTER 0 IN EITHER FIELD
FOR AUTO)
 0   100                        Y-PIXEL SIZE(cm), No. Y-PIXELS (ENTER 0 IN EITHER FIELD
FOR AUTO)
 1                              DETECTION MODE (1=ENERGY INTEGRATING, 2=PHOTON
COUNTING, 3=PULSE HEIGHT SPECTRUM aka ENERGY DISCRIMINATING)
```

```
 0.0  1.0e6  100                EMIN,EMAX(eV), No. OF E BINS (EMIN,EMAX USED ONLY
FOR MODE=2,3; No.BINS USED ONLY FOR MODE=3)
 1                              REPORT FORMAT (1=COLUMNAR, 2=MATRIX, 3=BINARY)
 0.0                            RELATIVE UNCERTAINTY (%) REQUESTED

SUBSECTION FOR SIGNAL COLLECTION EFFECTS:
 OFF                            ACTIVATE SIGNAL COLLECTION EFFECTS (ON or OFF)
 1                              WRITE POINT SPREAD FUNCTION TO A FILE (1=YES,0=NO)
 0.5      26.7                  CE0,CE1(cm^-1); COEFFS FOR COLLECTION EFFICIENCY:
CE(z)=CE0+CE1*z
 30.0e-4  -0.2                  FW0(cm),FW1; COEFFS FOR FWHM(z)= FW0+FW1*z
 0.0       0.0                  A,B FOR SIGNAL (S) GAUSSIAN NOISE WITH
FWHM(S)=sqrt(A+B*S) (USED ONLY FOR DET MODE=2,3)
[END OF PID SECTION]

#
# Illustrative values for the parameters of the signal collections effects for a 150-um-thick
CsI(Tl) scintillator
# irradiated with 25 keV photons. See M. Freed et al., Medical Physics 37 (2010) 2593.
#
# z coordinate in the detector ref. frame assumed to be 0 at the x-ray entrance face and
zmax=150 um at the photodiode face.
#
# Collection efficiency dependency on depth z:
#   CE(z) = CE0 + CE1*z  (linear approx)
#   z1 & collection efficiency at z1 (x-ray entrance):
#     0.0 cm      0.5
#   z2 & collection efficiency at z2 (photodiode):
#     150e-4 cm   0.9
#
#   => CE0 = 0.5
#      CE1 = 26.7 cm^-1
#
# FWHM dependency on depth z:
#   (note that FWHM is expected to decrease with z)
#   FWHM(z) = FW0 + FW1*z  (linear approx)
#   z1 & FWHM at z1 (x-ray entrance):
#     0.0 cm      30e-4 cm
#   z2 & FWHM at z2 (photodiode):
#     150e-4 cm   0.0 cm (a guess)
#
#   => FW0 = 30e-4 cm
#      FW1 = -0.2

[SECTION TALLY FLUENCE TRACK LENGTH v.2012-06-01]
 OFF                            STATUS (ON or OFF)
 1                              DETECTION MATERIAL
 1.0e2  1.0e9  70 LOG           EMIN,EMAX(eV), No. OF E BINS, APPEND 'LOG' FOR A LOG
SCALE
 0.0                            RELATIVE UNCERTAINTY (%) REQUESTED
[END OF FTL SECTION]

[SECTION TALLY PHOTON FLUENCE POINT v.2015-05-31]
 OFF                            STATUS (ON or OFF)
```

```
 OFF                          DEBUG ATTENUATION COEFFICIENTS (ON or OFF)
 0.0  0.0  1.0                DETECTOR POSITION COORDINATES (cm)
-0.1                          RADIUS OF EXCLUSION SPHERE AROUND DETECTOR (+
FOR cm, - FOR No. MFPs AT MAX E)
 0.0  1.0e6  100              EMIN,EMAX(eV), No. OF E BINS IN SPECTRUM
 0.0                          RELATIVE UNCERTAINTY (%) REQUESTED
[END OF PFP SECTION]

[SECTION TALLY PHASE SPACE FILE v.2009-06-15]
 OFF                          STATUS (ON or OFF)
 0                            PSF FORMAT (0=STANDARD penEasy ASCII, 1=IAEA BINARY)
 1                            DETECTION MATERIAL (MUST BE A PERFECT ABSORBENT,
EABS=+infty)
 output.psf                   PSF FILENAME, REMOVE EXTENSION IF FORMAT=1
[END OF PSF SECTION]

[SECTION TALLY PARTICLE CURRENT SPECTRUM v.2009-06-15]
 OFF                          STATUS (ON or OFF)
 50                           DETECTION MATERIAL
 0.0 1.0e5   100              EMIN,EMAX(eV), No. OF E BINS
 0.0                          RELATIVE UNCERTAINTY (%) REQUESTED
[END OF PCS SECTION]

[SECTION TALLY PARTICLE TRACK STRUCTURE v.2009-06-15]
 OFF                          STATUS (ON or OFF)
 100                          NUMBER OF HISTORIES TO DISPLAY (~100 RECOMMENDED)
[END OF PTS SECTION]


# >>>> VARIANCE-REDUCTION >>>>>>>>>>>>>>>>>>>>>>>>>>>>>>>>>>>>>>>>>>>>>>>>>>>>
#
# * For INTERACTION FORCING, interaction mechanisms are identified by the ICOL
#   label, as indicated in the following table (adapted from PENELOPE documentation):
#
#     +----+----------------+----------------+----------------+
#     |ICOL|electron (KPAR=1)|photon (KPAR=2)  |positron (KPAR=3)|
#     +----+----------------+----------------+----------------+
#     | 1  |hinge           |Rayleigh        |hinge           |
#     +----+----------------+----------------+----------------+
#     | 2  |elastic         |Compton         |elastic         |
#     +----+----------------+----------------+----------------+
#     | 3  |inelastic       |photoabsorption  |inelastic       |
#     +----+----------------+----------------+----------------+
#     | 4  |bremsstrahlung   |pair production  |bremsstrahlung   |
#     +----+----------------+----------------+----------------+
#     | 5  |inner-shell ion. |not defined      |inner-shell ion. |
#     +----+----------------+----------------+----------------+
#     | 6  |not defined      |not defined      |annihilation     |
#     +----+----------------+----------------+----------------+
#     | 7  |delta scattering |delta scattering |delta scattering |
#     +----+----------------+----------------+----------------+
#     | 8  |not defined      |not defined      |not defined      |
#     +----+----------------+----------------+----------------+
```

```
[SECTION INTERACTION FORCING v.2009-06-15]
 OFF                    STATUS (ON or OFF)
 1.0                    DO NOT APPLY BELOW THIS STATISTICAL WEIGHT (WMIN)
 MAT  KPAR  ICOL  FORCING  (SET MAT=-1 TO END LIST)
  1   1     0     1.0
 -1   0     0     1.0
[END OF VRIF SECTION]

[SECTION SPLITTING v.2015-05-30]
 OFF                    STATUS (ON or OFF)
 1.0                    WGHTMIN, DO NOT SPLIT BELOW THIS STATISTICAL WEIGHT
 1                      SPLITTING MATERIAL
 1                      SPLITTING MODE (1=SIMPLE; 2=ROTATIONAL; 3=XY)
 1                      SPLITTING FACTOR
 0.0  0.0  0.0          EULER ANGLES [Rz,Ry,Rz](deg), USED ONLY FOR MODES=2,3
 0.0  0.0  0.0          SHIFT (cm), USED ONLY FOR MODES=2,3
 0                      SIGN OF W ('+', '-' OR '0'=BOTH), USED ONLY FOR MODES=2,3
 0.0  360.0             AZIMUTHAL INTERVAL PHI0 IN [0,360)deg AND DeltaPHI IN
(0,360]deg, USED ONLY FOR MODE=2
[END OF VRS SECTION]

[SECTION RUSSIAN ROULETTE v.2009-06-15]
 OFF                    STATUS (ON or OFF)
 1.0                    WGHTMAX, DO NOT PLAY ABOVE THIS STATISTICAL WEIGHT
 1                      RUSSIAN ROULETTE MATERIAL
 1.0                    SURVIVAL PROBABILITY
[END OF VRRR SECTION]


# >>>> END OF FILE >>>>>>>>>>>>>>>>>>>>>>>>>>>>>>>>>>>>>>>>>>>>>>>>>>>>>>>>>
```

Appendix II

Thorax protocol Results

Specifications:

As scan points of the thorax protocols, we used:

- Phantom 10F: the center of the lungs, which is 107.19 cm in height and 20.30 cm laterally.
- Phantom 15F: the center of the lungs, which is 125.00 cm in height and 24.42 cm laterally.

  The cone beam has an angle of 4.97°.

  As reference for the relative percentage is considered 100 kV.

Table 22. Energy deposited, absorbed dose and relative variation evaluated in liver from CBCT Thorax protocol.

LIVER	**Phantom 10F**				**Phantom 15F**			
Tube Voltage [kV]	**En. Deposition [eV/hist]**	**Absorbed Dose [Gy/hist]**	**Dose % SD**	**Relvative variation [%]**	**En. Deposition [eV/hist]**	**Absorbed Dose [Gy/hist]**	**Dose % SD**	**Relvative variation [%]**
40	8.46E+02	1.63E-16	0.26%	-51.03%	5.84E+02	7.20E-17	0.24%	-59.38%
50	1.15E+03	2.22E-16	0.23%	-33.35%	8.46E+02	1.04E-16	0.22%	-41.15%
60	1.35E+03	2.60E-16	0.23%	-22.13%	1.04E+03	1.28E-16	0.22%	-27.90%
70	1.48E+03	2.86E-16	0.25%	-14.16%	1.18E+03	1.45E-16	0.20%	-18.25%
80	1.59E+03	3.06E-16	0.23%	-8.25%	1.28E+03	1.58E-16	0.15%	-10.70%
90	1.66E+03	3.21E-16	0.23%	-3.79%	1.37E+03	1.69E-16	0.21%	-4.67%
100	1.73E+03	3.33E-16	0.20%	REF	1.44E+03	1.77E-16	0.17%	REF
110	1.78E+03	3.43E-16	0.20%	2.88%	1.50E+03	1.84E-16	0.17%	4.08%
120	1.83E+03	3.52E-16	0.21%	5.69%	1.54E+03	1.90E-16	0.15%	7.12%

Table 23. Energy deposited, absorbed dose and relative variation evaluated in pancreas from CBCT Thorax protocol.

PANCREAS	Phantom 10F				Phantom 15F			
Tube Voltage [kV]	**En. Deposition [eV/hist]**	**Absorbed Dose [Gy/hist]**	**Dose % SD**	**Relvative variation [%]**	**En. Deposition [eV/hist]**	**Absorbed Dose [Gy/hist]**	**Dose % SD**	**Relvative variation [%]**
40	3.22E+00	8.61E-18	4.03%	-85.43%	1.74E+00	2.78E-18	4.44%	-90.51%
50	7.21E+00	1.93E-17	2.91%	-67.40%	4.60E+00	7.38E-18	3.04%	-74.83%
60	1.12E+01	3.00E-17	2.49%	-49.14%	7.99E+00	1.28E-17	2.50%	-56.30%
70	1.45E+01	3.86E-17	2.42%	-34.62%	1.11E+01	1.77E-17	1.99%	-39.50%
80	1.82E+01	4.86E-17	2.03%	-17.65%	1.40E+01	2.24E-17	1.36%	-23.68%
90	2.03E+01	5.43E-17	2.02%	-8.08%	1.63E+01	2.62E-17	1.90%	-10.69%
100	2.21E+01	5.91E-17	1.72%	REF	1.83E+01	2.93E-17	1.42%	REF
110	2.39E+01	6.39E-17	1.67%	8.26%	1.96E+01	3.15E-17	1.43%	7.32%
120	2.59E+01	6.91E-17	1.70%	17.07%	2.12E+01	3.40E-17	1.23%	15.91%

Table 24. Energy deposited, absorbed dose and relative variation evaluated in eyes from CBCT Thorax protocol.

EYES	Phantom 10F				Phantom 15F			
Tube Voltage [kV]	**En. Deposition [eV/hist]**	**Absorbed Dose [Gy/hist]**	**Dose % SD**	**Relvative variation [%]**	**En. Deposition [eV/hist]**	**Absorbed Dose [Gy/hist]**	**Dose % SD**	**Relvative variation [%]**
40	2.41E+00	3.22E-17	4.97%	-94.53%	8.02E-01	9.41E-18	6.73%	-95.87%
50	7.55E+00	1.01E-16	3.05%	-82.88%	2.59E+00	3.04E-17	4.24%	-86.65%
60	1.47E+01	1.96E-16	2.24%	-66.65%	5.62E+00	6.59E-17	3.21%	-71.09%
70	2.24E+01	2.99E-16	2.14%	-49.17%	9.11E+00	1.07E-16	2.30%	-53.09%
80	3.11E+01	4.16E-16	1.70%	-29.46%	1.28E+01	1.50E-16	1.49%	-34.16%
90	3.75E+01	5.00E-16	1.31%	-15.10%	1.66E+01	1.95E-16	2.05%	-14.56%
100	4.41E+01	5.89E-16	1.34%	REF	1.94E+01	2.28E-16	1.54%	REF
110	4.86E+01	6.49E-16	1.28%	10.10%	2.25E+01	2.63E-16	1.47%	15.58%
120	5.32E+01	7.11E-16	1.30%	20.65%	2.47E+01	2.90E-16	1.25%	27.27%

Table 25. Energy deposited, absorbed dose and relative variation evaluated in heart wall from CBCT Thorax protocol.

HEART WALL	Phantom 10F				Phantom 15F			
Tube Voltage [kV]	**En. Deposition [eV/hist]**	**Absorbed Dose [Gy/hist]**	**Dose % SD**	**Relvative variation [%]**	**En. Deposition [eV/hist]**	**Absorbed Dose [Gy/hist]**	**Dose % SD**	**Relvative variation [%]**
40	6.31E+02	7.22E-16	0.29%	-35.17%	7.60E+02	5.53E-16	0.21%	-40.10%
50	7.77E+02	8.89E-16	0.28%	-20.14%	9.64E+02	7.01E-16	0.20%	-24.02%
60	8.54E+02	9.78E-16	0.28%	-12.17%	1.08E+03	7.85E-16	0.21%	-14.92%
70	8.99E+02	1.03E-15	0.31%	-7.53%	1.15E+03	8.37E-16	0.19%	-9.32%
80	9.34E+02	1.07E-15	0.28%	-4.03%	1.20E+03	8.74E-16	0.14%	-5.26%
90	9.54E+02	1.09E-15	0.29%	-1.92%	1.24E+03	9.02E-16	0.21%	-2.24%
100	9.73E+02	1.11E-15	0.26%	REF	1.27E+03	9.23E-16	0.17%	REF
110	9.88E+02	1.13E-15	0.25%	1.55%	1.29E+03	9.42E-16	0.17%	2.03%
120	1.01E+03	1.15E-15	0.27%	3.43%	1.32E+03	9.60E-16	0.15%	3.95%

Table 26. Energy deposited, absorbed dose and relative variation evaluated in brain from CBCT Thorax protocol.

BRAIN	Phantom 10F				Phantom 15F			
Tube Voltage [kV]	**En. Deposition [eV/hist]**	**Absorbed Dose [Gy/hist]**	**Dose % SD**	**Relvative variation [%]**	**En. Deposition [eV/hist]**	**Absorbed Dose [Gy/hist]**	**Dose % SD**	**Relvative variation [%]**
40	1.28E-01	1.56E-20	20.36%	-72.05%	8.49E-02	1.05E-20	90.96%	-70.66%
50	1.83E-01	2.24E-20	18.59%	-59.97%	1.37E-01	1.69E-20	76.20%	-52.62%
60	2.18E-01	2.66E-20	17.45%	-52.36%	1.42E-01	1.76E-20	83.09%	-50.88%
70	3.17E-01	3.88E-20	17.02%	-30.59%	1.88E-01	2.33E-20	67.61%	-35.00%
80	3.51E-01	4.29E-20	14.53%	-23.19%	2.41E-01	2.98E-20	47.08%	-16.65%
90	4.40E-01	5.39E-20	13.63%	-3.63%	2.64E-01	3.27E-20	65.32%	-8.68%
100	4.57E-01	5.59E-20	11.60%	0.00%	2.89E-01	3.58E-20	50.23%	REF
110	5.41E-01	6.62E-20	11.09%	18.40%	3.48E-01	4.31E-20	48.25%	20.38%
120	6.25E-01	7.64E-20	10.88%	36.79%	3.65E-01	4.51E-20	39.80%	26.22%

Table 27. Energy deposited, absorbed dose and relative variation evaluated in kidney from CBCT Thorax protocol.

KIDNEY	Phantom 10F				Phantom 15F			
Tube Voltage [kV]	**En. Deposition [eV/hist]**	**Absorbed Dose [Gy/hist]**	**Dose % SD**	**Relvative variation [%]**	**En. Deposition [eV/hist]**	**Absorbed Dose [Gy/hist]**	**Dose % SD**	**Relvative variation [%]**
40	3.98E+00	3.54E-18	3.77%	-89.62%	1.93E+00	1.22E-18	4.26%	-92.46%
50	1.01E+01	8.96E-18	2.58%	-73.71%	5.58E+00	3.55E-18	2.69%	-78.16%
60	1.69E+01	1.51E-17	2.01%	-55.76%	9.80E+00	6.23E-18	2.25%	-61.64%
70	2.33E+01	2.08E-17	1.97%	-39.13%	1.46E+01	9.26E-18	1.79%	-43.02%
80	2.94E+01	2.62E-17	1.63%	-23.29%	1.87E+01	1.19E-17	1.17%	-26.64%
90	3.43E+01	3.05E-17	1.58%	-10.51%	2.23E+01	1.42E-17	1.66%	-12.63%
100	3.83E+01	3.41E-17	1.33%	REF	2.55E+01	1.62E-17	1.25%	REF
110	4.17E+01	3.71E-17	1.30%	8.84%	2.82E+01	1.79E-17	1.21%	10.27%
120	4.49E+01	3.99E-17	1.31%	17.16%	3.05E+01	1.94E-17	1.02%	19.42%

Table 28. Energy deposited, absorbed dose and relative variation evaluated in stomach wall from CBCT Thorax protocol.

STOMACH WALL	Phantom 10F				Phantom 15F			
Tube Voltage [kV]	**En. Deposition [eV/hist]**	**Absorbed Dose [Gy/hist]**	**Dose % SD**	**Relvative variation [%]**	**En. Deposition [eV/hist]**	**Absorbed Dose [Gy/hist]**	**Dose % SD**	**Relvative variation [%]**
40	1.85E+01	3.49E-17	1.73%	-72.65%	1.25E+01	1.67E-17	1.60%	-77.38%
50	3.16E+01	5.95E-17	1.39%	-53.34%	2.27E+01	3.04E-17	1.32%	-58.95%
60	4.22E+01	7.95E-17	1.26%	-37.70%	3.21E+01	4.30E-17	1.22%	-41.87%
70	5.10E+01	9.62E-17	1.29%	-24.58%	3.96E+01	5.31E-17	1.04%	-28.22%
80	5.81E+01	1.09E-16	1.14%	-14.19%	4.61E+01	6.17E-17	0.72%	-16.52%
90	6.39E+01	1.20E-16	1.11%	-5.64%	5.08E+01	6.81E-17	1.04%	-7.88%
100	6.77E+01	1.28E-16	0.98%	REF	5.52E+01	7.40E-17	0.82%	REF
110	7.09E+01	1.34E-16	0.94%	4.80%	5.87E+01	7.86E-17	0.80%	6.32%
120	7.39E+01	1.39E-16	0.97%	9.16%	6.13E+01	8.22E-17	0.68%	11.17%

Table 29. Energy deposited, absorbed dose and relative variation evaluated in spleen from CBCT Thorax protocol.

SPLEEN	Phantom 10F				Phantom 15F			
Tube Voltage [kV]	**En. Deposition [eV/hist]**	**Absorbed Dose [Gy/hist]**	**Dose % SD**	**Relvative variation [%]**	**En. Deposition [eV/hist]**	**Absorbed Dose [Gy/hist]**	**Dose % SD**	**Relvative variation [%]**
40	8.05E+00	1.61E-17	2.61%	-79.93%	5.57E+00	6.90E-18	2.51%	-85.08%
50	1.58E+01	3.16E-17	2.03%	-60.63%	1.21E+01	1.50E-17	1.82%	-67.53%
60	2.29E+01	4.59E-17	1.74%	-42.82%	1.90E+01	2.36E-17	1.63%	-49.00%
70	2.85E+01	5.70E-17	1.79%	-29.07%	2.49E+01	3.08E-17	1.33%	-33.37%
80	3.31E+01	6.64E-17	1.54%	-17.40%	3.02E+01	3.74E-17	0.93%	-19.08%
90	3.70E+01	7.41E-17	1.51%	-7.82%	3.43E+01	4.25E-17	1.31%	-8.10%
100	4.01E+01	8.04E-17	1.30%	REF	3.73E+01	4.63E-17	1.02%	REF
110	4.23E+01	8.48E-17	1.28%	5.47%	4.04E+01	5.01E-17	1.01%	8.37%
120	4.43E+01	8.88E-17	1.31%	10.45%	4.26E+01	5.28E-17	0.87%	14.12%

Table 30. Energy deposited, absorbed dose and relative variation evaluated in thyroid from CBCT Thorax protocol.

THYROID	Phantom 10F				Phantom 15F			
Tube Voltage [kV]	**En. Deposition [eV/hist]**	**Absorbed Dose [Gy/hist]**	**Dose % SD**	**Relvative variation [%]**	**En. Deposition [eV/hist]**	**Absorbed Dose [Gy/hist]**	**Dose % SD**	**Relvative variation [%]**
40	3.91E+01	7.93E-16	1.15%	-19.48%	9.93E+00	1.33E-16	1.81%	-61.41%
50	4.34E+01	8.80E-16	1.18%	-10.69%	1.43E+01	1.92E-16	1.61%	-44.35%
60	4.60E+01	9.33E-16	1.17%	-5.26%	1.85E+01	2.47E-16	1.57%	-28.27%
70	4.73E+01	9.59E-16	1.33%	-2.67%	2.07E+01	2.77E-16	1.40%	-19.72%
80	4.85E+01	9.84E-16	1.24%	-0.07%	2.30E+01	3.08E-16	1.04%	-10.62%
90	4.90E+01	9.93E-16	1.27%	0.81%	2.46E+01	3.29E-16	1.50%	-4.42%
100	4.86E+01	9.85E-16	1.15%	REF	2.57E+01	3.44E-16	1.20%	REF
110	4.90E+01	9.95E-16	1.16%	0.99%	2.66E+01	3.57E-16	1.24%	3.54%
120	4.95E+01	1.00E-15	1.23%	1.98%	2.72E+01	3.64E-16	1.07%	5.76%

Table 31. Energy deposited, absorbed dose and relative variation evaluated in bladder from CBCT Thorax protocol.

BLADDER	Phantom 10F				Phantom 15F			
Tube Voltage [kV]	**En. Deposition [eV/hist]**	**Absorbed Dose [Gy/hist]**	**Dose % SD**	**Relvative variation [%]**	**En. Deposition [eV/hist]**	**Absorbed Dose [Gy/hist]**	**Dose % SD**	**Relvative variation [%]**
40	7.66E-03	4.04E-20	84.88%	-95.15%	1.04E-02	3.37E-20	57.93%	-89.22%
50	2.57E-02	1.35E-19	46.77%	-83.74%	2.41E-02	7.82E-20	40.74%	-74.96%
60	4.63E-02	2.44E-19	36.72%	-70.66%	3.33E-02	1.08E-19	36.08%	-65.39%
70	7.94E-02	4.19E-19	33.99%	-49.66%	4.31E-02	1.40E-19	30.15%	-55.13%
80	1.03E-01	5.41E-19	25.34%	-34.95%	7.22E-02	2.35E-19	18.01%	-24.87%
90	1.52E-01	8.02E-19	22.99%	-3.49%	6.61E-02	2.15E-19	27.25%	10.52%
100	1.58E-01	8.31E-19	20.28%	REF	9.61E-02	3.12E-19	19.78%	REF
110	1.91E-01	1.01E-18	18.33%	21.01%	1.09E-01	3.55E-19	19.22%	13.73%
120	2.03E-01	1.07E-18	18.75%	28.46%	1.26E-01	4.09E-19	15.10%	30.96%

Table 32. Energy deposited, absorbed dose and relative variation evaluated in ovaries from CBCT Thorax protocol.

OVARIES	Phantom 10F				Phantom 15F			
Tube Voltage [kV]	**En. Deposition [eV/hist]**	**Absorbed Dose [Gy/hist]**	**Dose % SD**	**Relvative variation [%]**	**En. Deposition [eV/hist]**	**Absorbed Dose [Gy/hist]**	**Dose % SD**	**Relvative variation [%]**
40	3.11E-03	1.42E-19	135.22%	-86.14%	5.90E-02	1.57E-18	23.74%	-74.13%
50	3.79E-03	1.74E-19	110.73%	-83.08%	1.22E-01	3.26E-18	17.99%	-46.37%
60	7.08E-03	3.24E-19	90.36%	-68.40%	1.41E-01	3.77E-18	18.39%	-37.97%
70	7.39E-03	3.38E-19	90.71%	-67.05%	1.67E-01	4.45E-18	16.16%	-26.71%
80	1.80E-02	8.26E-19	60.98%	-19.54%	1.84E-01	4.90E-18	11.42%	-19.33%
90	4.24E-02	1.94E-18	44.77%	89.31%	1.91E-01	5.09E-18	16.75%	-16.19%
100	2.24E-02	1.03E-18	53.53%	REF	2.28E-01	6.08E-18	12.28%	REF
110	4.35E-02	1.99E-18	39.05%	94.21%	2.25E-01	5.99E-18	12.90%	-1.41%
120	3.80E-02	1.74E-18	39.46%	69.56%	2.35E-01	6.26E-18	11.08%	2.92%

Table 33. Energy deposited, absorbed dose and relative variation evaluated in oesophagous from CBCT Thorax protocol.

OESOPHAGOUS	Phantom 10F				Phantom 15F			
Tube Voltage [kV]	**En. Deposition [eV/hist]**	**Absorbed Dose [Gy/hist]**	**Dose % SD**	**Relvative variation [%]**	**En. Deposition [eV/hist]**	**Absorbed Dose [Gy/hist]**	**Dose % SD**	**Relvative variation [%]**
40	2.55E+01	2.27E-16	1.45%	-55.02%	2.06E+01	1.11E-16	1.31%	-67.43%
50	3.56E+01	3.17E-16	1.32%	-37.32%	3.29E+01	1.77E-16	1.09%	-47.94%
60	4.28E+01	3.81E-16	1.26%	-24.59%	4.25E+01	2.29E-16	1.06%	-32.72%
70	4.73E+01	4.21E-16	1.35%	-16.74%	4.97E+01	2.67E-16	0.93%	-21.30%
80	5.13E+01	4.56E-16	1.21%	-9.73%	5.47E+01	2.94E-16	0.68%	-13.45%
90	5.46E+01	4.86E-16	1.21%	-3.90%	5.94E+01	3.20E-16	0.98%	-5.90%
100	5.68E+01	5.06E-16	1.06%	REF	6.32E+01	3.40E-16	0.76%	REF
110	5.84E+01	5.20E-16	1.05%	2.75%	6.61E+01	3.56E-16	0.77%	4.74%
120	6.06E+01	5.40E-16	1.09%	6.72%	6.88E+01	3.70E-16	0.65%	8.88%

Table 34. Energy deposited, absorbed dose and relative variation evaluated in uterus from CBCT Thorax protocol.

UTERUS	Phantom 10F				Phantom 15F			
Tube Voltage [kV]	**En. Deposition [eV/hist]**	**Absorbed Dose [Gy/hist]**	**Dose % SD**	**Relvative variation [%]**	**En. Deposition [eV/hist]**	**Absorbed Dose [Gy/hist]**	**Dose % SD**	**Relvative variation [%]**
40	3.66E-05	1.47E-21	199.26%	-99.90%	4.13E-03	2.21E-20	89.69%	-95.06%
50	1.55E-03	6.21E-20	180.55%	-95.58%	1.17E-02	6.24E-20	58.34%	-86.05%
60	2.33E-03	9.34E-20	141.53%	-93.36%	1.65E-02	8.86E-20	53.18%	-80.19%
70	4.09E-03	1.64E-19	109.89%	-88.33%	2.19E-02	1.17E-19	43.84%	-73.79%
80	2.99E-02	1.20E-18	50.17%	-14.81%	5.29E-02	2.83E-19	22.70%	-36.70%
90	3.13E-02	1.25E-18	31.94%	-10.81%	5.86E-02	3.13E-19	30.73%	-29.87%
100	3.51E-02	1.41E-18	45.59%	REF	8.35E-02	4.47E-19	21.55%	REF
110	3.26E-02	1.30E-18	49.11%	-7.18%	9.08E-02	4.86E-19	20.93%	8.66%
120	2.94E-02	1.18E-18	47.66%	-16.31%	1.00E-01	5.35E-19	16.99%	19.76%

Table 35. Energy deposited, absorbed dose and relative variation evaluated in breast from CBCT Thorax protocol.

BREAST	Phantom 10F				Phantom 15F			
Tube Voltage [kV]	**En. Deposition [eV/hist]**	**Absorbed Dose [Gy/hist]**	**Dose % SD**	**Relvative variation [%]**	**En. Deposition [eV/hist]**	**Absorbed Dose [Gy/hist]**	**Dose % SD**	**Relvative variation [%]**
40	4.21E+01	8.64E-16	1.09%	57.53%	8.30E+02	5.31E-16	0.19%	30.06%
50	3.59E+01	7.38E-16	1.25%	34.44%	7.53E+02	4.82E-16	0.21%	18.05%
60	3.21E+01	6.59E-16	1.37%	20.15%	7.05E+02	4.51E-16	0.24%	10.47%
70	2.96E+01	6.08E-16	1.59%	10.76%	6.73E+02	4.30E-16	0.24%	5.49%
80	2.79E+01	5.72E-16	1.51%	4.28%	6.53E+02	4.18E-16	0.18%	2.41%
90	2.69E+01	5.53E-16	1.60%	0.82%	6.42E+02	4.11E-16	0.28%	0.71%
100	2.67E+01	5.49E-16	1.42%	REF	6.38E+02	4.08E-16	0.22%	REF
110	2.62E+01	5.39E-16	1.45%	-1.77%	6.35E+02	4.06E-16	0.24%	-0.39%
120	2.65E+01	5.45E-16	1.51%	-0.68%	6.36E+02	4.07E-16	0.20%	-0.27%

Table 36. Energy deposited, absorbed dose and relative variation evaluated in lung from CBCT Thorax protocol.

LUNG	Phantom 10F				Phantom 15F			
Tube Voltage [kV]	**En. Deposition [eV/hist]**	**Absorbed Dose [Gy/hist]**	**Dose % SD**	**Relvative variation [%]**	**En. Deposition [eV/hist]**	**Absorbed Dose [Gy/hist]**	**Dose % SD**	**Relvative variation [%]**
40	2.01E+03	6.44E-16	0.16%	-31.39%	2.83E+03	6.05E-16	0.11%	-26.96%
50	2.43E+03	7.79E-16	0.16%	-17.00%	3.32E+03	7.09E-16	0.11%	-14.40%
60	2.64E+03	8.47E-16	0.16%	-9.73%	3.55E+03	7.59E-16	0.11%	-8.45%
70	2.75E+03	8.83E-16	0.18%	-5.94%	3.67E+03	7.84E-16	0.11%	-5.34%
80	2.84E+03	9.08E-16	0.16%	-3.19%	3.76E+03	8.03E-16	0.08%	-3.12%
90	2.89E+03	9.25E-16	0.17%	-1.40%	3.82E+03	8.17E-16	0.12%	-1.41%
100	2.93E+03	9.38E-16	0.15%	REF	3.88E+03	8.29E-16	0.10%	REF
110	2.97E+03	9.51E-16	0.15%	1.34%	3.93E+03	8.38E-16	0.10%	1.19%
120	3.00E+03	9.63E-16	0.16%	2.61%	3.98E+03	8.50E-16	0.09%	2.56%

Table 37. Energy deposited, absorbed dose and relative variation evaluated in stomach contents from CBCT Thorax protocol.

STOMACH COUNT	Phantom 10F				Phantom 15F			
Tube Voltage [kV]	**En. Deposition [eV/hist]**	**Absorbed Dose [Gy/hist]**	**Dose % SD**	**Relvative variation [%]**	**En. Deposition [eV/hist]**	**Absorbed Dose [Gy/hist]**	**Dose % SD**	**Relvative variation [%]**
40	2.11E+01	2.89E-17	1.61%	-76.63%	1.28E+01	1.02E-17	1.64%	-83.30%
50	3.90E+01	5.35E-17	1.28%	-56.72%	2.71E+01	2.17E-17	1.22%	-64.65%
60	5.44E+01	7.45E-17	1.12%	-39.65%	4.06E+01	3.25E-17	1.11%	-47.04%
70	6.69E+01	9.16E-17	1.15%	-25.87%	5.17E+01	4.14E-17	0.93%	-32.47%
80	7.67E+01	1.05E-16	1.02%	-14.96%	6.24E+01	5.00E-17	0.66%	-18.51%
90	8.39E+01	1.15E-16	1.00%	-6.97%	7.03E+01	5.63E-17	0.92%	-8.24%
100	9.02E+01	1.24E-16	0.88%	REF	7.66E+01	6.14E-17	0.72%	REF
110	9.59E+01	1.31E-16	0.84%	6.26%	8.18E+01	6.55E-17	0.72%	6.79%
120	9.90E+01	1.36E-16	0.88%	9.73%	8.67E+01	6.95E-17	0.61%	13.20%

Head & Neck protocol Results

Specifications:

As scan points of the thorax protocols, we used:

- Phantom 10F: the center of the Cranium located at 131.31 cm in height and at 20.69 cm laterally.
- Phantom 15F: the center of the Cranium located at 152.85 cm in height and at 23.94 cm laterally.

  The cone beam has an angle of 4.77°.

  As reference for the relative percentage is considered 100 kV.

Table 38. Energy deposited, absorbed dose and relative variation evaluated in brain from CBCT Head & Neck protocol.

BRAIN	**Phantom 10F**				**Phantom 15F**			
Tube Voltage [kV]	**En. Deposition [eV/hist]**	**Absorbed Dose [Gy/hist]**	**Dose % SD**	**Relvative variation [%]**	**En. Deposition [eV/hist]**	**Absorbed Dose [Gy/hist]**	**Dose % SD**	**Relvative variation [%]**
40	1.33E+03	1.62E-16	0.22%	-70.45%	1.16E+03	1.44E-16	0.15%	-71.27%
50	2.21E+03	2.70E-16	0.19%	-50.91%	1.95E+03	2.42E-16	0.16%	-51.77%
60	2.90E+03	3.55E-16	0.13%	-35.50%	2.58E+03	3.19E-16	0.12%	-36.25%
70	3.43E+03	4.19E-16	0.15%	-23.77%	3.07E+03	3.79E-16	0.14%	-24.30%
80	3.87E+03	4.74E-16	0.16%	-13.84%	3.47E+03	4.29E-16	0.13%	-14.30%
90	4.21E+03	5.15E-16	0.16%	-6.29%	3.79E+03	4.69E-16	0.08%	-6.44%
100	4.49E+03	5.50E-16	0.14%	REF	4.05E+03	5.01E-16	0.07%	REF
110	4.74E+03	5.79E-16	0.13%	5.38%	4.27E+03	5.28E-16	0.13%	5.41%
120	4.95E+03	6.05E-16	0.12%	10.07%	4.47E+03	5.53E-16	0.12%	10.33%

Table 39. Energy deposited, absorbed dose and relative variation evaluated in heart wall from Head & Neck CBCT protocol.

HEART WALL	Phantom 10F				Phantom 15F			
Tube Voltage [kV]	**En. Deposition [eV/hist]**	**Absorbed Dose [Gy/hist]**	**Dose % SD**	**Relvative variation [%]**	**En. Deposition [eV/hist]**	**Absorbed Dose [Gy/hist]**	**Dose % SD**	**Relvative variation [%]**
40	4.48E-01	5.13E-19	11.39%	-85.97%	4.21E-01	3.06E-19	7.84%	-86.99%
50	8.18E-01	9.37E-19	9.29%	-74.36%	7.50E-01	5.46E-19	7.86%	-76.81%
60	1.29E+00	1.47E-18	6.21%	-59.64%	1.29E+00	9.40E-19	4.95%	-60.08%
70	1.70E+00	1.94E-18	6.48%	-46.77%	1.83E+00	1.33E-18	4.75%	-43.39%
80	2.33E+00	2.67E-18	6.43%	-26.90%	2.28E+00	1.66E-18	4.83%	-29.63%
90	2.87E+00	3.28E-18	5.93%	-10.22%	2.84E+00	2.07E-18	5.64%	-12.28%
100	3.19E+00	3.65E-18	5.01%	REF	3.24E+00	2.35E-18	2.38%	REF
110	3.58E+00	4.10E-18	4.47%	12.19%	3.53E+00	2.57E-18	4.24%	9.24%
120	3.98E+00	4.55E-18	4.02%	24.66%	3.81E+00	2.77E-18	3.67%	17.84%

Table 40. Energy deposited, absorbed dose and relative variation evaluated in eyes from Head & Neck CBCT protocol.

EYES	Phantom 10F				Phantom 15F			
Tube Voltage [kV]	**En. Deposition [eV/hist]**	**Absorbed Dose [Gy/hist]**	**Dose % SD**	**Relvative variation [%]**	**En. Deposition [eV/hist]**	**Absorbed Dose [Gy/hist]**	**Dose % SD**	**Relvative variation [%]**
40	2.42E+02	3.22E-15	0.50%	49.07%	2.44E+02	2.86E-15	0.32%	50.85%
50	2.10E+02	2.81E-15	0.57%	29.72%	2.12E+02	2.49E-15	0.45%	31.24%
60	1.92E+02	2.57E-15	0.49%	18.65%	1.92E+02	2.25E-15	0.39%	18.64%
70	1.79E+02	2.39E-15	0.62%	10.28%	1.80E+02	2.11E-15	0.54%	11.56%
80	1.71E+02	2.29E-15	0.70%	5.83%	1.70E+02	2.00E-15	0.52%	5.44%
90	1.66E+02	2.22E-15	0.78%	2.44%	1.66E+02	1.94E-15	0.66%	2.54%
100	1.62E+02	2.16E-15	0.68%	REF	1.62E+02	1.89E-15	0.32%	REF
110	1.60E+02	2.14E-15	0.62%	-1.11%	1.59E+02	1.87E-15	0.60%	-1.28%
120	1.59E+02	2.13E-15	0.61%	-1.63%	1.58E+02	1.85E-15	0.55%	-2.27%

Table 41. Energy deposited, absorbed dose and relative variation evaluated in thyroid from Head & Neck CBCT protocol.

THYROID	**Phantom 10F**				**Phantom 15F**			
Tube Voltage [kV]	**En. Deposition [eV/hist]**	**Absorbed Dose [Gy/hist]**	**Dose % SD**	**Relvative variation [%]**	**En. Deposition [eV/hist]**	**Absorbed Dose [Gy/hist]**	**Dose % SD**	**Relvative variation [%]**
40	3.51E-01	7.12E-18	12.82%	-89.01%	3.04E-01	4.07E-18	9.21%	-88.40%
50	7.47E-01	1.52E-17	9.50%	-76.60%	6.18E-01	8.27E-18	8.58%	-76.43%
60	1.29E+00	2.62E-17	6.05%	-59.61%	9.77E-01	1.31E-17	5.63%	-62.71%
70	1.93E+00	3.91E-17	6.22%	-39.56%	1.49E+00	2.00E-17	6.10%	-43.06%
80	2.41E+00	4.90E-17	6.21%	-24.43%	1.90E+00	2.54E-17	5.17%	-27.70%
90	2.95E+00	5.99E-17	6.09%	-7.54%	2.17E+00	2.91E-17	6.44%	-17.11%
100	3.19E+00	6.48E-17	5.01%	REF	2.62E+00	3.51E-17	2.67%	REF
110	3.48E+00	7.06E-17	4.60%	8.93%	2.93E+00	3.92E-17	1.84%	11.81%
120	3.78E+00	7.67E-17	4.23%	18.34%	3.18E+00	4.26E-17	4.08%	21.42%

Table 42. Energy deposited, absorbed dose and relative variation evaluated in ovaries from Head & Neck CBCT protocol.

OVARIES	Phantom 10F				Phantom 15F			
Tube Voltage [kV]	**En. Deposition [eV/hist]**	**Absorbed Dose [Gy/hist]**	**Dose % SD**	**Relvative variation [%]**	**En. Deposition [eV/hist]**	**Absorbed Dose [Gy/hist]**	**Dose % SD**	**Relvative variation [%]**
40	Not found	Not found	Not found	Not found	6.57E-04	1.75E-20	182.66%	-79.51%
50	3.58E-05	1.64E-21	200.91%	-86.51%	Not found	Not found	Not found	Not found
60	1.03E-05	4.72E-22	203.88%	-96.12%	1.02E-03	2.71E-20	196.70%	-68.29%
70	6.13E-05	2.81E-21	195.62%	-76.90%	2.64E-04	7.03E-21	144.11%	-91.78%
80	Not found	Not found	Not found	Not found	1.08E-03	2.88E-20	194.72%	-66.36%
90	5.33E-05	2.44E-21	142.56%	-79.93%	1.59E-04	4.24E-21	201.43%	-95.04%
100	2.66E-04	1.22E-20	199.55%	REF	3.21E-03	8.55E-20	71.74%	REF
110	1.39E-03	6.36E-20	158.46%	422.72%	5.33E-03	1.42E-19	97.65%	66.10%
120	9.39E-04	4.30E-20	170.44%	253.44%	3.98E-04	1.06E-20	108.07%	-87.59%

Table 43. Energy deposited, absorbed dose and relative variation evaluated in oesophagous from Head & Neck CBCT protocol.

OESOPHAGOUS	Phantom 10F				Phantom 15F			
Tube Voltage [kV]	**En. Deposition [eV/hist]**	**Absorbed Dose [Gy/hist]**	**Dose % SD**	**Relvative variation [%]**	**En. Deposition [eV/hist]**	**Absorbed Dose [Gy/hist]**	**Dose % SD**	**Relvative variation [%]**
40	9.90E-02	8.81E-19	24.25%	-91.27%	9.55E-02	5.14E-19	16.76%	-89.73%
50	2.50E-01	2.23E-18	16.80%	-77.94%	1.94E-01	1.04E-18	15.49%	-79.19%
60	4.50E-01	4.00E-18	10.45%	-60.31%	3.35E-01	1.80E-18	9.86%	-64.02%
70	6.35E-01	5.66E-18	10.70%	-43.93%	4.65E-01	2.50E-18	10.96%	-49.96%
80	7.37E-01	6.56E-18	10.99%	-34.98%	6.75E-01	3.63E-18	8.60%	-27.47%
90	1.00E+00	8.94E-18	9.96%	-11.36%	8.05E-01	4.33E-18	10.19%	-13.50%
100	1.13E+00	1.01E-17	8.03%	REF	9.30E-01	5.00E-18	4.41%	REF
110	1.33E+00	1.18E-17	7.00%	17.27%	9.90E-01	5.32E-18	7.68%	6.39%
120	1.39E+00	1.24E-17	6.69%	22.60%	1.14E+00	6.15E-18	6.64%	22.96%

Table 44. Energy deposited, absorbed dose and relative variation evaluated in breast from Head & Neck CBCT protocol.

BREAST	Phantom 10F				Phantom 15F			
Tube Voltage [kV]	**En. Deposition [eV/hist]**	**Absorbed Dose [Gy/hist]**	**Dose % SD**	**Relvative variation [%]**	**En. Deposition [eV/hist]**	**Absorbed Dose [Gy/hist]**	**Dose % SD**	**Relvative variation [%]**
40	4.90E-02	1.01E-18	32.67%	-39.30%	1.55E+00	9.90E-19	3.94%	-41.75%
50	4.74E-02	9.74E-19	35.85%	-41.23%	1.69E+00	1.08E-18	5.04%	-36.57%
60	6.07E-02	1.25E-18	26.34%	-24.72%	1.89E+00	1.21E-18	3.91%	-28.77%
70	7.35E-02	1.51E-18	29.93%	-8.90%	2.11E+00	1.35E-18	4.73%	-20.48%
80	7.76E-02	1.59E-18	32.20%	-3.77%	2.34E+00	1.49E-18	4.28%	-12.16%
90	7.34E-02	1.51E-18	34.05%	-9.02%	2.48E+00	1.58E-18	5.65%	-6.86%
100	8.07E-02	1.66E-18	28.51%	REF	2.66E+00	1.70E-18	2.44%	REF
110	7.49E-02	1.54E-18	26.70%	-7.18%	2.79E+00	1.78E-18	4.31%	4.79%
120	9.98E-02	2.05E-18	24.05%	23.68%	2.92E+00	1.87E-18	4.11%	9.81%

Table 45. Energy deposited, absorbed dose and relative variation evaluated in lung from Head & Neck CBCT protocol.

LUNG	Phantom 10F				Phantom 15F			
Tube Voltage [kV]	**En. Deposition [eV/hist]**	**Absorbed Dose [Gy/hist]**	**Dose % SD**	**Relvative variation [%]**	**En. Deposition [eV/hist]**	**Absorbed Dose [Gy/hist]**	**Dose % SD**	**Relvative variation [%]**
40	3.29E+00	1.06E-18	4.25%	-84.86%	4.12E+00	8.80E-19	2.43%	-82.01%
50	5.87E+00	1.88E-18	3.58%	-73.03%	7.11E+00	1.52E-18	2.53%	-68.96%
60	9.34E+00	2.99E-18	2.36%	-57.08%	1.03E+01	2.19E-18	1.75%	-55.23%
70	1.25E+01	4.02E-18	2.47%	-42.38%	1.38E+01	2.94E-18	2.11%	-39.98%
80	1.61E+01	5.17E-18	2.48%	-25.80%	1.72E+01	3.67E-18	1.74%	-24.93%
90	1.89E+01	6.04E-18	2.44%	-13.34%	2.03E+01	4.34E-18	2.12%	-11.42%
100	2.18E+01	6.97E-18	1.93%	REF	2.29E+01	4.89E-18	0.92%	REF
110	2.37E+01	7.59E-18	1.77%	8.84%	2.55E+01	5.46E-18	1.64%	11.51%
120	2.63E+01	8.43E-18	1.63%	20.92%	2.77E+01	5.91E-18	1.45%	20.80%

Pelvic protocol Results

Specifications:

As scan points of the thorax protocols, we used:

- Phantom 10F: the center of the Pelvis located at 73.60 cm in height and at 20.89 cm laterally.
- Phantom 15F: the center of the Pelvis located at 88.09 cm in height and at 24.00 cm laterally.

  The cone beam has an angle of 4.77°.

  As reference for the relative percentage is considered 120 kV.

Table 46. Energy deposited, absorbed dose and relative variation evaluated in liver from Pelvic CBCT protocol.

LIVER	**Phantom 10F**				**Phantom 15F**			
Tube Voltage [kV]	**En. Deposition [eV/hist]**	**Absorbed Dose [Gy/hist]**	**Dose % SD**	**Relvative variation [%]**	**En. Deposition [eV/hist]**	**Absorbed Dose [Gy/hist]**	**Dose % SD**	**Relvative variation [%]**
40	4.70E+00	9.07E-19	2.11%	-91.75%	8.56E+00	1.05E-18	2.10%	-91.08%
50	1.17E+01	2.27E-18	1.96%	-79.39%	2.03E+01	2.51E-18	0.93%	-78.79%
60	2.00E+01	3.86E-18	1.90%	-64.84%	3.41E+01	4.21E-18	1.20%	-64.39%
70	2.79E+01	5.39E-18	1.68%	-50.93%	4.81E+01	5.93E-18	1.12%	-49.84%
80	3.61E+01	6.96E-18	1.53%	-36.68%	6.05E+01	7.46E-18	0.86%	-36.92%
90	4.26E+01	8.22E-18	1.50%	-25.23%	7.14E+01	8.81E-18	1.06%	-25.50%
100	4.79E+01	9.24E-18	1.34%	-15.97%	8.05E+01	9.92E-18	0.78%	-16.10%
110	5.27E+01	1.02E-17	1.23%	-7.39%	8.90E+01	1.10E-17	0.82%	-7.18%
120	5.69E+01	1.10E-17	1.25%	REF	9.59E+01	1.18E-17	0.74%	REF

Table 47. Energy deposited, absorbed dose and relative variation evaluated in pancreas from Pelvic CBCT protocol.

PANCREAS	Phantom 10F				Phantom 15F			
Tube Voltage [kV]	**En. Deposition [eV/hist]**	**Absorbed Dose [Gy/hist]**	**Dose % SD**	**Relvative variation [%]**	**En. Deposition [eV/hist]**	**Absorbed Dose [Gy/hist]**	**Dose % SD**	**Relvative variation [%]**
40	1.33E+00	3.56E-18	3.90%	-88.33%	1.84E+00	2.95E-18	4.41%	-89.49%
50	3.05E+00	8.14E-18	3.61%	-73.35%	4.28E+00	6.86E-18	2.03%	-75.50%
60	4.86E+00	1.30E-17	3.70%	-57.52%	6.96E+00	1.12E-17	2.59%	-60.14%
70	6.34E+00	1.69E-17	3.31%	-44.61%	9.49E+00	1.52E-17	2.42%	-45.63%
80	7.87E+00	2.10E-17	3.18%	-31.22%	1.15E+01	1.85E-17	1.91%	-33.98%
90	9.21E+00	2.46E-17	3.15%	-19.50%	1.34E+01	2.15E-17	2.39%	-23.25%
100	1.03E+01	2.75E-17	2.72%	-10.06%	1.52E+01	2.44E-17	1.71%	-13.01%
110	1.08E+01	2.87E-17	2.60%	-5.97%	1.62E+01	2.60E-17	1.79%	-7.17%
120	1.14E+01	3.06E-17	2.62%	REF	1.75E+01	2.80E-17	1.66%	REF

Table 48. Energy deposited, absorbed dose and relative variation evaluated in brain from Pelvic CBCT protocol.

BRAIN	Phantom 10F				Phantom 15F			
Tube Voltage [kV]	**En. Deposition [eV/hist]**	**Absorbed Dose [Gy/hist]**	**Dose % SD**	**Relvative variation [%]**	**En. Deposition [eV/hist]**	**Absorbed Dose [Gy/hist]**	**Dose % SD**	**Relvative variation [%]**
40	4.14E-02	5.07E-21	22.69%	-88.43%	2.78E-02	3.44E-21	35.94%	-88.29%
50	9.24E-02	1.13E-20	22.73%	-74.19%	6.32E-02	7.81E-21	17.42%	-73.42%
60	1.45E-01	1.77E-20	23.51%	-59.60%	9.00E-02	1.11E-20	24.44%	-62.12%
70	1.67E-01	2.04E-20	22.20%	-53.46%	9.80E-02	1.21E-20	25.52%	-58.76%
80	2.10E-01	2.57E-20	20.50%	-41.41%	1.82E-01	2.24E-20	16.52%	-23.58%
90	3.05E-01	3.74E-20	13.42%	-14.68%	1.71E-01	2.11E-20	22.84%	-28.12%
100	2.95E-01	3.61E-20	17.30%	-17.65%	2.01E-01	2.48E-20	16.42%	-15.42%
110	3.32E-01	4.06E-20	16.26%	-7.27%	2.62E-01	3.24E-20	16.04%	10.19%
120	3.58E-01	4.38E-20	16.48%	REF	2.38E-01	2.94E-20	1015.45%	REF

Table 49. Energy deposited, absorbed dose and relative variation evaluated in heart wall from Pelvic CBCT protocol.

HEART WALL	Phantom 10F				Phantom 15F			
Tube Voltage [kV]	**En. Deposition [eV/hist]**	**Absorbed Dose [Gy/hist]**	**Dose % SD**	**Relvative variation [%]**	**En. Deposition [eV/hist]**	**Absorbed Dose [Gy/hist]**	**Dose % SD**	**Relvative variation [%]**
40	1.25E-01	1.43E-19	12.82%	-94.65%	1.10E-01	8.02E-20	18.14%	-95.43%
50	3.19E-01	3.65E-19	11.61%	-86.35%	3.16E-01	2.30E-19	7.59%	-86.89%
60	6.28E-01	7.18E-19	10.67%	-73.12%	6.02E-01	4.38E-19	8.81%	-75.06%
70	9.21E-01	1.05E-18	8.90%	-60.54%	9.09E-01	6.61E-19	7.92%	-62.34%
80	1.27E+00	1.45E-18	7.89%	-45.71%	1.33E+00	9.67E-19	5.64%	-44.91%
90	1.53E+00	1.75E-18	7.85%	-34.55%	1.61E+00	1.17E-18	6.85%	-33.43%
100	1.76E+00	2.02E-18	6.81%	-24.58%	1.94E+00	1.41E-18	4.80%	-19.66%
110	2.03E+00	2.32E-18	5.93%	-13.26%	2.25E+00	1.64E-18	4.88%	-6.54%
120	2.33E+00	2.67E-18	6.00%	REF	2.41E+00	1.76E-18	4.56%	REF

Table 50. Energy deposited, absorbed dose and relative variation evaluated in kidney from Pelvic CBCT protocol.

KIDNEY	Phantom 10F				Phantom 15F			
Tube Voltage [kV]	**En. Deposition [eV/hist]**	**Absorbed Dose [Gy/hist]**	**Dose % SD**	**Relvative variation [%]**	**En. Deposition [eV/hist]**	**Absorbed Dose [Gy/hist]**	**Dose % SD**	**Relvative variation [%]**
40	3.88E+00	3.45E-18	2.32%	-88.43%	3.72E+00	2.36E-18	3.23%	-90.70%
50	8.74E+00	7.78E-18	2.29%	-73.94%	9.00E+00	5.73E-18	1.44%	-77.46%
60	1.38E+01	1.23E-17	2.24%	-58.71%	1.48E+01	9.40E-18	1.83%	-62.98%
70	1.86E+01	1.66E-17	2.04%	-44.41%	2.03E+01	1.29E-17	1.72%	-49.06%
80	2.31E+01	2.05E-17	1.86%	-31.14%	2.57E+01	1.63E-17	1.28%	-35.63%
90	2.61E+01	2.32E-17	1.88%	-22.11%	3.04E+01	1.93E-17	1.61%	-23.95%
100	2.95E+01	2.63E-17	1.66%	-11.90%	3.41E+01	2.17E-17	1.17%	-14.53%
110	3.22E+01	2.87E-17	1.52%	-3.86%	3.73E+01	2.37E-17	1.23%	-6.64%
120	3.35E+01	2.98E-17	1.58%	REF	3.99E+01	2.54E-17	1.10%	REF

Table 51. Energy deposited, absorbed dose and relative variation evaluated in stomach wall from Pelvic CBCT protocol.

STOMACH WALL	Phantom 10F				Phantom 15F			
Tube Voltage [kV]	**En. Deposition [eV/hist]**	**Absorbed Dose [Gy/hist]**	**Dose % SD**	**Relvative variation [%]**	**En. Deposition [eV/hist]**	**Absorbed Dose [Gy/hist]**	**Dose % SD**	**Relvative variation [%]**
40	9.83E-01	1.85E-18	4.48%	-88.86%	1.29E+00	1.72E-18	5.14%	-89.19%
50	2.20E+00	4.15E-18	4.32%	-75.07%	2.97E+00	3.98E-18	2.39%	-75.02%
60	3.50E+00	6.60E-18	4.29%	-60.34%	4.89E+00	6.55E-18	3.07%	-58.89%
70	4.85E+00	9.14E-18	3.92%	-45.05%	6.41E+00	8.59E-18	2.96%	-46.11%
80	5.87E+00	1.11E-17	3.58%	-33.51%	7.91E+00	1.06E-17	2.28%	-33.48%
90	7.03E+00	1.33E-17	3.56%	-20.33%	9.39E+00	1.26E-17	2.77%	-21.07%
100	7.80E+00	1.47E-17	3.08%	-11.62%	1.05E+01	1.40E-17	2.01%	-12.10%
110	8.38E+00	1.58E-17	2.87%	-5.08%	1.13E+01	1.51E-17	2.13%	-5.12%
120	8.82E+00	1.66E-17	2.95%	REF	1.19E+01	1.59E-17	1.93%	REF

Table 52. Energy deposited, absorbed dose and relative variation evaluated in small intestine wall from Pelvic CBCT protocol.

WALL SMALL INTESTINE	Phantom 10F				Phantom 15F			
Tube Voltage [kV]	**En. Deposition [eV/hist]**	**Absorbed Dose [Gy/hist]**	**Dose % SD**	**Relvative variation [%]**	**En. Deposition [eV/hist]**	**Absorbed Dose [Gy/hist]**	**Dose % SD**	**Relvative variation [%]**
40	7.94E+02	3.44E-16	0.15%	-29.87%	1.08E+03	3.42E-16	0.18%	-32.44%
50	9.33E+02	4.04E-16	0.21%	-17.60%	1.28E+03	4.05E-16	0.12%	-19.89%
60	1.00E+03	4.33E-16	0.26%	-11.58%	1.38E+03	4.38E-16	0.18%	-13.48%
70	1.04E+03	4.50E-16	0.26%	-8.24%	1.44E+03	4.57E-16	0.19%	-9.72%
80	1.07E+03	4.61E-16	0.26%	-5.90%	1.49E+03	4.70E-16	0.16%	-7.02%
90	1.09E+03	4.70E-16	0.29%	-4.10%	1.52E+03	4.82E-16	0.22%	-4.79%
100	1.10E+03	4.78E-16	0.26%	-2.59%	1.55E+03	4.90E-16	0.17%	-3.11%
110	1.12E+03	4.84E-16	0.25%	-1.22%	1.57E+03	4.97E-16	0.18%	-1.72%
120	1.13E+03	4.90E-16	0.26%	REF	1.60E+03	5.06E-16	0.17%	REF

Table 53. Energy deposited, absorbed dose and relative variation evaluated in spleen from Pelvic CBCT protocol.

SPLEEN	Phantom 10F				Phantom 15F			
Tube Voltage [kV]	**En. Deposition [eV/hist]**	**Absorbed Dose [Gy/hist]**	**Dose % SD**	**Relvative variation [%]**	**En. Deposition [eV/hist]**	**Absorbed Dose [Gy/hist]**	**Dose % SD**	**Relvative variation [%]**
40	2.92E-01	5.84E-19	8.57%	-92.97%	3.54E-01	4.39E-19	10.17%	-94.48%
50	7.62E-01	1.53E-18	7.61%	-81.64%	1.05E+00	1.30E-18	4.10%	-83.63%
60	1.41E+00	2.82E-18	7.11%	-66.14%	1.98E+00	2.45E-18	4.91%	-69.18%
70	1.95E+00	3.91E-18	6.15%	-53.02%	2.84E+00	3.52E-18	4.58%	-55.74%
80	2.64E+00	5.28E-18	5.69%	-36.45%	3.86E+00	4.79E-18	3.37%	-39.80%
90	2.91E+00	5.82E-18	5.51%	-29.99%	4.43E+00	5.50E-18	4.06%	-30.87%
100	3.46E+00	6.93E-18	4.91%	-16.66%	5.16E+00	6.40E-18	2.91%	-19.50%
110	3.77E+00	7.55E-18	4.51%	-9.19%	5.73E+00	7.11E-18	3.14%	-10.64%
120	4.15E+00	8.31E-18	4.58%	REF	6.41E+00	7.95E-18	2.81%	REF

Table 54. Energy deposited, absorbed dose and relative variation evaluated in bladder from Pelvic CBCT protocol.

BLADDER	Phantom 10F				Phantom 15F			
Tube Voltage [kV]	**En. Deposition [eV/hist]**	**Absorbed Dose [Gy/hist]**	**Dose % SD**	**Relvative variation [%]**	**En. Deposition [eV/hist]**	**Absorbed Dose [Gy/hist]**	**Dose % SD**	**Relvative variation [%]**
40	1.87E+02	9.86E-16	0.33%	-23.02%	1.52E+02	4.93E-16	0.48%	-40.54%
50	2.16E+02	1.14E-15	0.44%	-11.14%	1.91E+02	6.21E-16	0.30%	-25.19%
60	2.27E+02	1.20E-15	0.53%	-6.50%	2.13E+02	6.91E-16	0.46%	-16.71%
70	2.33E+02	1.23E-15	0.56%	-4.32%	2.24E+02	7.29E-16	0.49%	-12.17%
80	2.36E+02	1.24E-15	0.55%	-2.91%	2.35E+02	7.63E-16	0.42%	-8.07%
90	2.37E+02	1.25E-15	0.59%	-2.36%	2.42E+02	7.85E-16	0.54%	-5.31%
100	2.38E+02	1.25E-15	0.55%	-2.14%	2.47E+02	8.02E-16	0.41%	-3.27%
110	2.41E+02	1.27E-15	0.54%	-0.89%	2.52E+02	8.19E-16	0.44%	-1.28%
120	2.43E+02	1.28E-15	0.58%	REF	2.55E+02	8.29E-16	0.43%	REF

Table 55. Energy deposited, absorbed dose and relative variation evaluated in ovaries from Pelvic CBCT protocol.

OVARIES	Phantom 10F				Phantom 15F			
Tube Voltage [kV]	**En. Deposition [eV/hist]**	**Absorbed Dose [Gy/hist]**	**Dose % SD**	**Relvative variation [%]**	**En. Deposition [eV/hist]**	**Absorbed Dose [Gy/hist]**	**Dose % SD**	**Relvative variation [%]**
40	1.29E+01	5.92E-16	1.24%	-43.10%	1.92E+01	5.11E-16	1.36%	-46.06%
50	1.69E+01	7.72E-16	1.60%	-25.81%	2.49E+01	6.62E-16	0.85%	-30.02%
60	1.88E+01	8.59E-16	1.92%	-17.51%	2.81E+01	7.49E-16	1.28%	-20.91%
70	1.98E+01	9.08E-16	1.91%	-12.72%	3.03E+01	8.08E-16	1.35%	-14.61%
80	2.07E+01	9.47E-16	1.93%	-9.02%	3.15E+01	8.39E-16	1.14%	-11.35%
90	2.18E+01	9.99E-16	2.02%	-4.05%	3.29E+01	8.78E-16	1.49%	-7.23%
100	2.21E+01	1.01E-15	1.86%	-2.87%	3.40E+01	9.06E-16	1.12%	-4.32%
110	2.25E+01	1.03E-15	1.73%	-1.07%	3.45E+01	9.19E-16	1.22%	-2.93%
120	2.27E+01	1.04E-15	1.85%	REF	3.55E+01	9.47E-16	1.13%	REF

Table 56. Energy deposited, absorbed dose and relative variation evaluated in uterus from Pelvic CBCT protocol.

UTERUS	Phantom 10F				Phantom 15F			
Tube Voltage [kV]	**En. Deposition [eV/hist]**	**Absorbed Dose [Gy/hist]**	**Dose % SD**	**Relvative variation [%]**	**En. Deposition [eV/hist]**	**Absorbed Dose [Gy/hist]**	**Dose % SD**	**Relvative variation [%]**
40	9.78E+00	3.92E-16	1.43%	-55.97%	4.46E+01	2.39E-16	0.90%	-64.37%
50	1.38E+01	5.53E-16	1.74%	-37.76%	6.82E+01	3.65E-16	0.51%	-45.56%
60	1.66E+01	6.64E-16	2.05%	-25.38%	8.38E+01	4.48E-16	0.74%	-33.09%
70	1.83E+01	7.34E-16	1.97%	-17.49%	9.47E+01	5.07E-16	0.77%	-24.34%
80	1.95E+01	7.82E-16	2.00%	-12.12%	1.04E+02	5.58E-16	0.63%	-16.76%
90	2.00E+01	8.00E-16	2.05%	-10.06%	1.11E+02	5.93E-16	0.81%	-11.53%
100	2.08E+01	8.33E-16	1.92%	-6.31%	1.17E+02	6.24E-16	0.61%	-6.90%
110	2.16E+01	8.63E-16	1.81%	-2.91%	1.21E+02	6.49E-16	0.65%	-3.19%
120	2.22E+01	8.89E-16	1.85%	REF	1.25E+02	6.70E-16	0.61%	REF

Table 57. Energy deposited, absorbed dose and relative variation evaluated in breast from Pelvic CBCT protocol.

BREAST	Phantom 10F				Phantom 15F			
Tube Voltage [kV]	**En. Deposition [eV/hist]**	**Absorbed Dose [Gy/hist]**	**Dose % SD**	**Relvative variation [%]**	**En. Deposition [eV/hist]**	**Absorbed Dose [Gy/hist]**	**Dose % SD**	**Relvative variation [%]**
40	1.10E-02	2.25E-19	40.17%	-36.22%	4.73E-01	3.03E-19	8.24%	-65.44%
50	1.14E-02	2.35E-19	54.19%	-33.39%	5.63E-01	3.60E-19	5.33%	-58.89%
60	5.29E-03	1.09E-19	90.74%	-69.20%	6.93E-01	4.43E-19	7.79%	-49.36%
70	8.41E-03	1.73E-19	91.59%	-51.05%	7.93E-01	5.07E-19	8.07%	-42.05%
80	1.83E-02	3.77E-19	60.01%	6.73%	8.86E-01	5.66E-19	6.43%	-35.29%
90	1.67E-02	3.44E-19	71.73%	-2.60%	1.04E+00	6.63E-19	8.10%	-24.27%
100	2.35E-02	4.83E-19	55.32%	36.82%	1.19E+00	7.64E-19	5.78%	-12.74%
110	1.62E-02	3.33E-19	56.81%	-5.72%	1.32E+00	8.46E-19	5.97%	-3.35%
120	1.72E-02	3.53E-19	64.04%	REF	1.37E+00	8.75E-19	5.55%	REF

Table 58. Energy deposited, absorbed dose and relative variation evaluated in lung from Pelvic CBCT protocol.

LUNG	Phantom 10F				Phantom 15F			
Tube Voltage [kV]	**En. Deposition [eV/hist]**	**Absorbed Dose [Gy/hist]**	**Dose % SD**	**Relvative variation [%]**	**En. Deposition [eV/hist]**	**Absorbed Dose [Gy/hist]**	**Dose % SD**	**Relvative variation [%]**
40	3.06E-01	9.80E-20	8.18%	-94.74%	3.25E-01	6.94E-20	10.47%	-95.79%
50	7.76E-01	2.49E-19	7.60%	-86.63%	9.14E-01	1.95E-19	4.49%	-88.15%
60	1.51E+00	4.84E-19	6.62%	-73.97%	1.77E+00	3.78E-19	5.20%	-77.06%
70	2.35E+00	7.52E-19	5.97%	-59.60%	2.86E+00	6.10E-19	4.55%	-62.96%
80	3.14E+00	1.01E-18	5.10%	-45.98%	4.05E+00	8.66E-19	3.21%	-47.44%
90	3.89E+00	1.25E-18	4.88%	-32.99%	4.98E+00	1.06E-18	4.01%	-35.37%
100	4.62E+00	1.48E-18	4.33%	-20.46%	5.96E+00	1.27E-18	2.85%	-22.66%
110	5.24E+00	1.68E-18	3.81%	-9.70%	6.71E+00	1.43E-18	2.83%	-12.93%
120	5.81E+00	1.86E-18	3.79%	REF	7.71E+00	1.65E-18	2.59%	REF

Table 59. Energy deposited, absorbed dose and relative variation evaluated in stomach contents from Pelvic CBCT protocol.

STOMACH CONT	Phantom 10F				Phantom 15F			
Tube Voltage [kV]	**En. Deposition [eV/hist]**	**Absorbed Dose [Gy/hist]**	**Dose % SD**	**Relvative variation [%]**	**En. Deposition [eV/hist]**	**Absorbed Dose [Gy/hist]**	**Dose % SD**	**Relvative variation [%]**
40	1.58E+00	2.16E-18	3.61%	-89.77%	2.96E+00	2.37E-18	3.38%	-89.86%
50	3.74E+00	5.12E-18	3.48%	-75.78%	6.96E+00	5.58E-18	1.58%	-76.13%
60	6.21E+00	8.50E-18	3.38%	-59.76%	1.14E+01	9.11E-18	2.02%	-61.01%
70	8.23E+00	1.13E-17	3.04%	-46.64%	1.54E+01	1.23E-17	1.95%	-47.29%
80	1.01E+01	1.38E-17	2.77%	-34.47%	1.93E+01	1.54E-17	1.51%	-33.95%
90	1.22E+01	1.67E-17	2.78%	-20.79%	2.22E+01	1.78E-17	1.89%	-23.70%
100	1.32E+01	1.81E-17	2.50%	-14.45%	2.51E+01	2.01E-17	1.36%	-13.94%
110	1.43E+01	1.95E-17	2.31%	-7.49%	2.72E+01	2.18E-17	1.43%	-6.56%
120	1.54E+01	2.11E-17	2.33%	REF	2.92E+01	2.34E-17	1.30%	REF

Table 60. Energy deposited, absorbed dose and relative variation evaluated in liver from small intestine contents CBCT protocol.

CONT SMALL INTESTINE	Phantom 10F				Phantom 15F			
Tube Voltage [kV]	**En. Deposition [eV/hist]**	**Absorbed Dose [Gy/hist]**	**Dose % SD**	**Relvative variation [%]**	**En. Deposition [eV/hist]**	**Absorbed Dose [Gy/hist]**	**Dose % SD**	**Relvative variation [%]**
40	3.95E+02	3.88E-16	0.23%	-29.48%	6.69E+02	1.74E-16	0.22%	-31.13%
50	4.68E+02	4.60E-16	0.30%	-16.45%	7.97E+02	2.08E-16	0.15%	-17.93%
60	5.04E+02	4.95E-16	0.36%	-10.12%	8.62E+02	2.25E-16	0.23%	-11.34%
70	5.22E+02	5.13E-16	0.36%	-6.91%	8.95E+02	2.33E-16	0.25%	-7.89%
80	5.33E+02	5.23E-16	0.38%	-4.96%	9.18E+02	2.39E-16	0.21%	-5.58%
90	5.41E+02	5.32E-16	0.41%	-3.40%	9.34E+02	2.43E-16	0.28%	-3.91%
100	5.49E+02	5.39E-16	0.36%	-2.09%	9.49E+02	2.47E-16	0.21%	-2.36%
110	5.54E+02	5.45E-16	0.36%	-1.06%	9.60E+02	2.50E-16	0.23%	-1.23%
120	5.60E+02	5.51E-16	0.37%	REF	9.72E+02	2.53E-16	0.22%	REF

Table 61. Energy deposited, absorbed dose and relative variation evaluated in right colon contents from Pelvic CBCT protocol.

RIGHT COLON CONT	Phantom 10F				Phantom 15F			
Tube Voltage [kV]	**En. Deposition [eV/hist]**	**Absorbed Dose [Gy/hist]**	**Dose % SD**	**Relvative variation [%]**	**En. Deposition [eV/hist]**	**Absorbed Dose [Gy/hist]**	**Dose % SD**	**Relvative variation [%]**
40	3.38E+01	1.93E-16	0.77%	-34.80%	1.41E+02	5.27E-16	0.50%	-6.52%
50	4.09E+01	2.34E-16	1.00%	-21.13%	1.49E+02	5.57E-16	0.34%	-1.26%
60	4.54E+01	2.60E-16	1.23%	-12.51%	1.51E+02	5.63E-16	0.54%	-0.17%
70	4.73E+01	2.71E-16	1.23%	-8.82%	1.51E+02	5.63E-16	0.60%	-0.17%
80	4.89E+01	2.80E-16	1.25%	-5.67%	1.51E+02	5.63E-16	0.52%	-0.16%
90	5.05E+01	2.89E-16	1.33%	-2.66%	1.51E+02	5.65E-16	0.66%	0.05%
100	5.15E+01	2.94E-16	1.22%	-0.78%	1.51E+02	5.63E-16	0.54%	-0.28%
110	5.17E+01	2.96E-16	1.18%	-0.33%	1.51E+02	5.62E-16	0.59%	-0.32%
120	5.19E+01	2.97E-16	1.23%	REF	1.51E+02	5.64E-16	0.55%	REF

Table 62. Energy deposite, absorbed dose and relative variation evaluated in left colon contents from Pelvic CBCT protocol.

LEFT COLON CONT	Phantom 10F				Phantom 15F			
Tube Voltage [kV]	**En. Deposition [eV/hist]**	**Absorbed Dose [Gy/hist]**	**Dose % SD**	**Relvative variation [%]**	**En. Deposition [eV/hist]**	**Absorbed Dose [Gy/hist]**	**Dose % SD**	**Relvative variation [%]**
40	6.54E+00	6.35E-17	1.68%	-52.28%	1.62E+02	4.27E-16	0.46%	1.57%
50	8.82E+00	8.56E-17	2.15%	-35.69%	1.65E+02	4.35E-16	0.32%	3.41%
60	1.05E+01	1.02E-16	2.49%	-23.76%	1.65E+02	4.34E-16	0.52%	3.10%
70	1.15E+01	1.11E-16	2.44%	-16.37%	1.62E+02	4.27E-16	0.58%	1.57%
80	1.22E+01	1.18E-16	2.46%	-11.16%	1.61E+02	4.23E-16	0.50%	0.57%
90	1.28E+01	1.24E-16	2.59%	-6.99%	1.59E+02	4.20E-16	0.69%	-0.09%
100	1.33E+01	1.29E-16	2.41%	-3.18%	1.59E+02	4.19E-16	0.52%	-0.49%
110	1.36E+01	1.32E-16	2.28%	-0.95%	1.58E+02	4.16E-16	0.58%	-1.08%
120	1.37E+01	1.33E-16	2.33%	REF	1.60E+02	4.21E-16	0.54%	REF

Annex

Annex I

In this section details about two phantoms and organs used for the work are reported [116].

- *Phantom 10F*

  Age: 10 years old;

  Height: 138 cm;

  Weight: 32 kg;

  Voxel No.: 54037156;

  Voxel size: 2.377 cm².

Table 20. Phantom 10F organ mass and volume [116].

Phantom 10F	Mass [g]	Volume [cm²]
Bladder	30.4	29.4
Brain	1310	1258.9
Breast	7.8	7.9
Eyes	12	12
Heart Wall	140	133.8
Kidney	180	181.5
Left Colon	16.5	33.7
Liver	830	788.9
Lung	500	1166.4
Oesophagus	18	17.5
Ovaries	3.5	3.3
Pancreas	60	58
Right Colon	28	27.2
Small intestine Content	163	287.1
Small intestine Wall	370	358.7
Spleen	80	75.1
Stomach Content	85	82.4
Stomach Wall	117	113.5
Thyroid	7.9	7.5
Uterus	4	3.8

- *Phantom 15F*

Age: 15 years old;
Height: 161 cm;
Weight: 53 kg;
Voxel No: 54037156;
Vozel Size: 4.072 cm².

Table 21. Phantom 15F organ mass and volume [116].

Phantom 15F	Mass [g]	Volume [cm²]
Bladder	29.4	29.9
Brain	1296.02	1246.2
Breast	7.9	7.8
Eyes	13.66	13.4
Heart Wall	220.18	211.7
Kidney	181.5	188.7
Left Colon	60.8	59.6
Liver	788.9	828.4
Lung	750	2949.7
Oesophagus	29.79	28.9
Ovaries	6.01	5.7
Pancreas	99.86	97.9
Right Colon	42.9	43.7
Small intestine Content	614.7	280
Small intestine Wall	506.4	521.6
Spleen	129.2	121.9
Stomach Content	199.94	196
Stomach Wall	119.53	116
Thyroid	11.97	11.4
Uterus	3.8	4